



TUM School of Natural Sciences

Technische Universität München

Nuclear Structure Investigations of Light Nuclei  
with the R<sup>3</sup>B Experiment

Tobias Jenegger

Vollständiger Abdruck der von der TUM School of Natural Sciences der Technischen  
Universität München zur Erlangung des akademischen Grades eines  
Doktors der Naturwissenschaften (Dr. rer. nat.)  
genehmigten Dissertation.

Vorsitz: TBA  
Prüfer\*innen der Dissertation:  
1. TBA  
2. TBA

Die Dissertation wurde am DATUM-HIER bei der Technischen Universität München  
eingereicht und durch die TUM School of Natural Sciences am DATUM-HIER  
angenommen.





TUM School of Natural Sciences

---

Nuclear Structure Investigations of Light Nuclei  
with the R<sup>3</sup>B Experiment

---

Tobias Jenegger



Techinsche Universität München  
Fachbereich: Dense and Strange Hadronic Matter (E62)

2025



# Abstract

The nucleosynthesis of heavy elements ( $A > 56$ ) beyond iron, primarily via the rapid neutron-capture process (r-process), represents one of the most fascinating and complex phenomena in nuclear astrophysics. This process, which is responsible for the majority of heavy element production in the universe, provides a critical interface between astrophysics and nuclear physics, offering a unique "laboratory" to study nuclear reactions and properties far from stability. Moreover, neutron star mergers (NSMs), which are stellar collisions involving NSs, are recognized as major astrophysical sites for the r-process. Neutron stars (NS), with their extreme densities and exotic compositions, are of exceptional interest in this context. These astrophysical objects serve as a natural laboratory to explore nuclear structure under extreme conditions, such as those described by the equation of state (EoS). Understanding the EoS, which governs the macroscopic properties of neutron stars, remains a formidable challenge. While astrophysical observations provide macroscopic constraints on NS models, nuclear experiments in terrestrial laboratories play a vital role in constraining the microscopic nuclear physics parameters embedded within these models. A comprehensive understanding of the r-process requires detailed knowledge of nuclear structure and reaction dynamics in regimes far from nuclear stability.

This doctoral thesis, titled "Nuclear Structure Investigations of Light Nuclei with the R<sup>3</sup>B Experiment", addresses detailed investigations on the state of the art experimental techniques to study key properties of the most exotic nuclei with highest precision. These investigations were conducted with the R<sup>3</sup>B (Reactions with Relativistic Radioactive Beams) setup during the commissioning experiment S444 as part of the FAIR Phase-0 campaign at GSI. Specifically, this work focuses on:

1. Charge-changing and total interaction cross sections: The study of  $^{12}\text{C} + ^{12}\text{C}$  collisions via the transmission method. These measurements provide critical insights into the nuclear matter radius and its distribution, which serve as essential benchmarks for understanding the EoS of nuclear matter in astrophysical environments.
2. Quasi-Free Scattering (QFS) reactions: The investigation of the  $^{12}\text{C}(\text{p},2\text{p})^{11}\text{B}$  reaction as a tool to probe the single particle structure of nuclei. This approach demonstrates in addition its potential for studying the recycling branch of the r-process through fission in QFS experiments and with it probing the evolution of fission barriers so far only known for few nuclei close to stability.

By advancing our knowledge of fundamental nuclear properties and reaction dynamics, this work bridges the gap between laboratory-based nuclear physics and astrophysical processes, shedding light on the origin of heavy elements in the universe.





# Contents

<b>1</b>	<b>Introduction</b>	<b>1</b>
1.1	R <sup>3</sup> B Experiment - "The Universe in the Lab"	2
1.1.1	Scientific Objectives and Research Program of the R3B Experiment at FAIR	2
1.1.2	Study of the EoS at R3B	3
<b>2</b>	<b>Nuclear Scattering Reactions in the Glauber Framework</b>	<b>5</b>
2.1	Elastic scattering at low energies	5
2.2	Nuclear Density distribution studies via elastic scattering	5
2.3	Glauber Model for nuclear scattering at high energies	6
2.3.1	Extensions to the Glauber model	6
2.4	Cross sections for <sup>12</sup> C + <sup>12</sup> C	6
2.5	Quasi-Free Scattering (QFS) Reactions	7
2.5.1	Kinematics of QFS Reactions	8
2.5.2	Cross Sections for QFS Reactions - Qualitative Considerations	13
2.5.3	Application Fields of QFS Reactions	13
<b>3</b>	<b>Experiment</b>	<b>20</b>
3.1	GSI facility	21
3.1.1	FAIR Project	22
3.2	R <sup>3</sup> B Setup	22
3.3	Detector Setup in S444 Commissioning Experiment 2020	23
3.3.1	Multi Wire Proportional Chambers (MWPC)	24
3.3.2	Ionization Chambers - R <sup>3</sup> B Music/TWIN Music	26
3.3.3	Sofia Start Detector	29
3.3.4	GLAD Magnet	29
3.3.5	CALIFA Calorimeter	29
3.3.6	Sofia Time of Flight Wall	38
3.3.7	NeuLAND Detector	38
<b>4</b>	<b>Analysis - Total Interaction Cross Section of <sup>12</sup>C + <sup>12</sup>C</b>	<b>41</b>
4.1	Cross Section Measurement via Transmission Method	41
4.2	Event Selection	43
4.3	Charge Changing Cross Section Measurement	48

4.3.1	TWIN MUSIC Calibration . . . . .	50
4.3.2	TWIN MUSIC Event Selection . . . . .	51
4.3.3	Carbon Identification . . . . .	53
4.4	Geometric Corrections . . . . .	58
4.5	Isotope Correction - Total Interaction Cross Section . . . . .	61
4.5.1	Results for Isotope Correction Methods . . . . .	66
4.6	Statistical and Systematic Error Analysis . . . . .	67
4.6.1	Statistical Uncertainties . . . . .	69
4.6.2	Systematic Uncertainties . . . . .	70
4.7	(Preliminary) Results Total Interaction Cross Section . . . . .	70
<b>5</b>	<b>Qualitative Analysis -</b>	
	<b>Quasi-Free Scattering <math>^{12}\text{C}(\text{p},2\text{p})^{11}\text{B}</math></b>	<b>72</b>
5.1	Setup-Calibration . . . . .	72
5.1.1	Flight-Path Reconstruction . . . . .	72
5.1.2	Time of Flight Calibration . . . . .	75
5.2	Event Selection . . . . .	76
5.3	Fragment Identification . . . . .	77
5.4	QFS-Protons . . . . .	79
5.4.1	Missing Momentum $\mathbf{p}_{\text{miss}}$ Reconstruction . . . . .	84
5.4.2	Correlations between $^{11}\text{B}$ Fragment and the reconstructed inner Proton . . . . .	86
5.4.3	Proton Separation Energy $S_p$ . . . . .	87
5.5	Reconstruction of excited $^{11}\text{B}$ states . . . . .	90
5.6	Fission via Quasi-Free Scattering reaction . . . . .	94
<b>6</b>	<b>Machine Learning for the Cluster Reconstruction in the CALIFA Calorimeter at R<sup>3</sup>B</b>	<b>101</b>
6.1	Gamma Spectroscopy with the Standard R3B Clustering Algorithm . .	102
6.1.1	Challenges in Relativistic Gamma Spectroscopy . . . . .	102
6.1.2	The Standard R3B Clustering Algorithm . . . . .	104
6.2	Data Simulation and Selection . . . . .	104
6.2.1	Simulation Setup . . . . .	104
6.2.2	Performance Metrics . . . . .	106
6.3	Agglomerative Clustering Model . . . . .	106
6.4	Edge Detection Neural Network . . . . .	107
6.5	Results . . . . .	109
6.6	Discussion and Outlook . . . . .	112

<b>Appendices</b>	<b>113</b>
<b>A Pileup rejection with R3B MUSIC charge cut</b>	<b>113</b>
<b>B MWPCs - <i>cal-to-hit</i> data processing</b>	<b>113</b>
B.1 Coherent clustering . . . . .	115
<b>C MWPC0 selection cuts</b>	<b>116</b>
<b>D Alternative methods for TWIN MUSIC hit selection and charge as- signment</b>	<b>118</b>
<b>E TWIN MUSIC Geometric Acceptance Correction via Efficiency Mea- surement</b>	<b>123</b>
<b>F Overview of isotope correction methods - selection cuts on the MWPC1/2/3</b>	<b>124</b>
<b>G Flight-Path Reconstruction</b>	<b>124</b>
<b>References</b>	<b>128</b>

# 1 Introduction

The elemental abundances observed throughout the universe are a fingerprint of the formation and evolution of astrophysical objects. Understanding the origin and distribution of these elements requires a robust theoretical framework based on nuclear structure models. The synthesis of elements – from the lightest nuclei formed during Big Bang nucleosynthesis to the heaviest transuranic elements produced in explosive astrophysical environments – depends critically on the properties of atomic nuclei.

The foundation for modern nuclear structure theory was laid by the atomic shell model, first introduced by Niels Bohr in 1913. This model, while initially developed for electrons in atoms, inspired the formulation of the nuclear shell model by Maria Goeppert Mayer and J. Hans D. Jensen in 1949. Their key innovation was the inclusion of a significant spin-orbit interaction term in the nuclear mean-field potential. Unlike the atomic case – where spin-orbit coupling appears as a relatively small fine-structure correction – in the nuclear shell model, the spin-orbit interaction is of comparable magnitude to the primary energy level gaps and carries an inverted sign. This results in the  $j = l + 1/2$  states lying energetically below the  $j = l - 1/2$  states.

This critical adjustment enabled the nuclear shell model to accurately reproduce the so-called "magic numbers" (2, 8, 20, 28, 50, 82, and 126), which correspond to closed shells of protons or neutrons associated with exceptional nuclear stability. Notable examples include isotopes such as those of tin ( $Z = 50$ ) and lead ( $Z = 82$ ), where large energy gaps between filled and unfilled shells lead to enhanced binding energies and structural rigidity.

While the shell model has proven highly successful in describing nuclei close to stability, recent experiments have shown, that the magic shells can be substantially modified in case of exotic species, like  $^{32}\text{Mg}$  [1] or  $^{28}\text{O}$  [2]. In case of more heavy regions, experimental data remain scarce, and the shell model must be extended or augmented to account for collective phenomena and configuration mixing. These nuclei play a central role in rapid neutron-capture processes (r-process), which are responsible for the formation of approximately half of the heavy elements beyond iron. In particular, the fate of the r-process path – its termination via fission and the possible emergence of a predicted "island of stability" in the superheavy region – depends critically on the structural properties of such exotic nuclei.

This chapter introduces the scientific objectives and research program of the R<sup>3</sup>B experiment. In particular, we highlight the role of nuclear structure studies in constraining the nuclear equation of state (EOS), especially for highly asymmetric nuclear matter. Nuclear scattering reactions at R<sup>3</sup>B offer an effective probe of these systems, and their

theoretical treatment – along with a general overview of reaction mechanisms – will be presented in chapter 2.

## 1.1 R<sup>3</sup>B Experiment - "The Universe in the Lab"

### 1.1.1 Scientific Objectives and Research Program of the R3B Experiment at FAIR

The R3B experiment (Reactions with Relativistic Radioactive Beams) is a key component of the nuclear astrophysics program at the Facility for Antiproton and Ion Research (FAIR) in Darmstadt and major experiment of the NUSTAR (Nuclear STructure, Astrophysics and Reactions) collaboration [3].

As part of the broader research initiative "*The Universe in the Lab*", R3B aims to provide a comprehensive understanding of the fundamental nuclear processes that govern the formation of elements in the universe. It seeks to replicate, under controlled laboratory conditions, the extreme environments found in stellar explosions and neutron-star mergers – astrophysical sites in which rapid nuclear reactions are responsible for the synthesis of the heavy elements [4].

The central scientific objective of R3B is the investigation of the structure and reaction dynamics of exotic, short-lived nuclei far from the valley of stability, particularly those involved in the rapid neutron-capture process (r-process) and other astrophysical nucleosynthesis pathways [5]. This includes the determination of key nuclear properties such as masses, lifetimes, decay modes, and reaction cross sections, as well as branching ratios and transition probabilities under conditions similar to those of astrophysical environments.

To address these goals, R3B employs high-intensity, relativistic radioactive ion beams in conjunction with a versatile and high-resolution detectors capable of performing kinematically complete measurements of both incoming and outgoing reaction products. The experimental program covers a wide variety of reaction mechanisms, including fragmentation, Coulomb excitation, knockout, and charge-exchange reactions, as well as inverse kinematics reactions such as (p,n) and (n,p) on liquid hydrogen targets besides on carbon, plastic and lead targets - depending on the experimental focus.

The R3B setup is specifically optimized for operation at beam energies of several hundred MeV per nucleon. It provides precise tracking and unambiguous particle identification, with excellent resolution in time, energy, and position [6]. These capabilities are essential for disentangling complex reaction channels and for extracting high-precision nuclear data that serve as critical input to astrophysical models of nucleosynthesis.

Directly related to the scientific objectives at R3B is the exploration of the equation of

state (EoS) of asymmetric nuclear matter under extreme conditions. The EoS describes how nuclear matter behaves as a function of parameters such as density, temperature, and isospin asymmetry, and it plays a pivotal role in understanding a wide range of astrophysical phenomena, including the structure and evolution of neutron stars, core-collapse supernovae, and neutron star mergers.

### 1.1.2 Study of the EoS at R3B

While various models agree at saturation density  $n_0 \approx 0.16 \text{ fm}^{-3}$  (natural packing density of nucleons inside a nucleus) at high baryon number density, as it is the case in neutron stars there are significant differences between the models. Fig X shows the EoS description for different models and their divergences by plotting the binding energy and the symmetry energy – which will be introduced in the next paragraph – versus the baryon number density. Huge efforts are made to constrain the EoS for highly asymmetric or pure neutron matter.

In modeling the nuclear equation of state, it is common to perform a Taylor expansion of the energy per nucleon with respect to the isospin asymmetry parameter  $\delta = \frac{n_n - n_p}{n_n + n_p}$  where  $n_n$  and  $n_p$  denote the neutron and proton number densities, respectively, at a fixed baryon density  $n_B = n_n + n_p$ . In this approach, the energy per nucleon is written as:

$$E(n_B, \delta) = E(n_B, 0) + S(n_B)\delta^2 + \mathcal{O}(\delta^4) \quad (1)$$

The second term on the left side of equation 1 is called the asymmetry term. With:

$$S(n) = \frac{1}{2} \left. \frac{\partial^2 E(n, \delta)}{\partial \delta^2} \right|_{\delta=0} \quad (2)$$

This approach allows one to isolate the contribution of the symmetry energy  $S(n_B)$  which governs the leading-order dependence on isospin asymmetry.

To further understand how the symmetry energy evolves with density – particularly in environments such as neutron stars –  $S(n_B)$  is itself often expanded around the nuclear saturation density  $n_0$  in a separate Taylor series involving the slope  $L$  and curvature  $K_{\text{sym}}$  parameters:

$$S(n_B) = S_0 + L \left( \frac{n_B - n_0}{3n_0} \right) + \frac{1}{2} K_{\text{sym}} \left( \frac{n_B - n_0}{3n_0} \right)^2 + \dots \quad (3)$$

$S_0$  is constrained around 30-40 MeV which is compatible to the theoretical predictions. Both  $L$  and  $K$  are poorly constrained and according experimental data is limited. While the term with the curvature parameter  $K$  enters quadratically, its contribution is small near to saturation density.

Whereas the slope parameter L is the dominating factor. Constraining L, which quantifies the "stiffness" of the symmetry energy – how much the energy cost of isospin asymmetry increases as nuclear matter becomes denser – is of high interest and would lead to a better understanding of nuclear matter and its interaction, especially when considering extreme astrophysical object such as NS.

Central formula is the equation of states (EOS). We want to study it within a wide range.

- in astrophysics NS are herefore of special interest. Measuring their mass and radius -> this relation depends on the EOS.
- since NS are highly asymmetric matter (neutrons only) they are a good playground to test the different models. Since they are all consistent at rho0 (real world) they diverge for higher matter asymmetry.
- plot of some models
- formula of tailor expansion of Equation of state
- at FAIR we want to study nuclear matter under extreme conditions, highly asymmetric matter.
- constraining the symmetry energy
- this can be done via neutron removal cross section, cite T. Aumann, Bertulani etc.
- show picture of sensitiveness of this method, shortly mention that L was previously constrained in PREX experiments (give some literature for further readings)
- the predicted models rely on the input from reaction mechanisms ->  $^{12}\text{C}+^{12}\text{C}$  good to probe the underlying reaction mechanisms -> one part of the thesis

Moreover to study the single particle states of nucleons inside nucleus, especially when going toward exotic nuclei -> quasi free scattering experiments. -> refer to the theory of those scattering experiments. This was the first time we had our CALIFA CALORIMETER in its final frame. Refer to the application section.

To point out is the pilot experiment we had in 2021 to study fission via qfs. This could have a large impact in the understanding of the dynamics of fission far off the line of stability.

Explain the fission via qfs a little bit more in detail here.

This could explain maybe better the element abundances we have and if there is any island of stability at  $Z > 126$ .

## 2 Nuclear Scattering Reactions in the Glauber Framework

Explain path to go:

- short intro why we use scattering reactions: to study structure of nuclei (mostly via e. scattering as they only interact via electromagn. force) and refer to chapter. Introduce problems qe account body problem etc
- starting from elastic scattering at low energies going to medium to high energies
- explain glauber: eikonal wave approximations, optical limit which leads to optical potential model, description via nucleon nucleon interaction

### 2.1 Elastic scattering at low energies

- Rutherford scattering,poiniering works (alpha particle on gold atoms),description in classical mechanics
- Rutherford scattering only valid if coulomb potential
- at low energies below pion production only elastic cross section
- introduce here the Scattering problem in quantum mechanics (see Schindler, p. 23)
- from classical physics we go to quantum mechanics and use partial wave decomposition with theta being the scattering angle
- include in this picture coulomb and nuclear interaction (as done in Kuk, page 120)

### 2.2 Nuclear Density distribution studies via elastic scattering

- Rutherford, Mott and Rosenbluth
- show something about form Factors
- are charge radii and nuclear radii measured?
- note approximation for  $^{12}C$  that neutron radius same as proton radius

## 2.3 Glauber Model for nuclear scattering at high energies

- explain model assumption
- eikonal wave approximation: high incoming momentum, low scattering angle
- Show picture of scattering
- optical limit: - Nucleons at high energy are undeflected due to large momentum (linear trajectory) -Nucleus large compared to nucleon-nucleon force -Motion of nucleons independent of nucleus -overall cross-section described in terms of nucleon-nucleon cross section
- Description in the Probability Approach (also here I use all the eiconal and optical limit approximation)
- Description in the Eikonal optical-limit approximation
- Comparison of both descriptions methods for total interaction cross section, should end up with same. Advantage of PA is that you can calculate the cross section for a defined number of removed projectile nucleons (Schindler, p. 49)

### 2.3.1 Extensions to the Glauber model

- things which cannot be neglected and influence the cross section
- in medium modifications (see Lukas thesis)
- Coulomb interaction
- Pauli blocking

## 2.4 Cross sections for $^{12}C + ^{12}C$

- Total reaction cross section
- charge changing cross section; maybe I have to include lise++ calculations
- isotope corrections- neutron removal; maybe I have to include lise++ calculations

## 2.5 Quasi-Free Scattering (QFS) Reactions

Quasi-free scattering (QFS) reactions, as a subset of direct reactions, are processes where a projectile nucleon interacts with a target nucleon via the strong nuclear force in a single and fast localized event at large momentum transfer which allows for a highly localized vertex. The relative kinetic energies of the participants, typically in the order of  $E_{kin} \gtrsim 100$  AMeV, are high<sup>1</sup>.

In QFS experiments conducted in direct kinematics, a proton serves as the projectile, colliding with a nucleon or a cluster within the target nucleus. Conversely, in inverse kinematics, the nucleus of interest becomes the projectile, while a proton or proton-like particle is used as the target. Despite these differing setups, both approaches are fundamentally equivalent, differing only due to a Lorentz transformation of the reference frame.

As the name implies, QFS reactions are conceptually similar to free nucleon-nucleon scattering, with the primary approximation being that the influence of the residual nucleus is neglected to first order. This approximation simplifies the theoretical description of the process, allowing to treat the interaction as a two-body problem within a (only weakly interfering) nuclear environment.

The first experiments confirming the existence of quasi-free scattering processes were conducted at the University of California, Berkeley, in 1952 by O. Chamberlain and Emilio Segrè[7]. In their study, lithium nuclei were bombarded with 350 MeV protons, and coincident proton pairs were observed with an opening angle of approximately 90°. That same year, J.B. Cladis, W.N. Hess, and B.J. Moyer published results on the scattering of 340 MeV protons on deuterium and carbon targets[8], further substantiating the phenomenon.

In 1957, Tyrén, Maris, and Hillman designed an experiment aimed at fully characterizing proton-proton collisions within the quasi-free scattering framework[9]. Their results validated the assumption of a direct and clean interaction between the projectile and the target nucleon, free from significant distortions caused by the surrounding nucleus. Furthermore, these experiments demonstrated that QFS reactions could serve as a powerful tool for probing nuclear structure and testing predictions of the shell model. Specifically, they enabled the study of key nuclear parameters such as spin-orbit splitting and energy differences between nuclear shells probing the shell evolution.

In QFS reactions, these parameters can be extracted by analyzing the reaction products, which include the two correlated outgoing protons, the residual nucleus, and any gamma rays emitted during de-excitation of the residual nucleus. The detailed measure-

---

<sup>1</sup>Which is needed for the single nucleon-nucleon interaction. The *de Broglie wavelength* of a 100 MeV proton corresponds to  $\lambda \approx 2.79\text{ fm}$  which is in the order of the proton diameter ( $\approx 1.6\text{ fm}$ )

ments of these observables provide critical insights into the underlying nuclear structure and dynamics.

The experimental discoveries and theoretical insights from these early studies strongly pushed the advancements in the theoretical modeling of QFS reactions. These models have since become essential tools for understanding nucleon-nucleon interactions within the nuclear medium and for further investigations of nuclear structure and reaction mechanisms.

### 2.5.1 Kinematics of QFS Reactions

A simplified picture, which however explains the essential kinematics of the QFS reaction, can be found in figure 1: we have an incoming proton knocking out a nuclear constituent (proton/neutron) in a quasi-free nucleon-nucleon collision ending with a final state having the scattered proton, the scattered off nuclear constituent and the rest nucleus ( $A-1$ ), which could be either in the ground-state or an excited state. In this picture index  $0$  is assigned to the incoming proton,  $1$  to the knocked out nucleon,  $2$  to the outgoing projectile proton,  $A$  to the initial nucleus and  $A-1$  to the final nucleus accordingly. As from standard textbooks (see [10, Chapter 6.2]) the energy-momentum

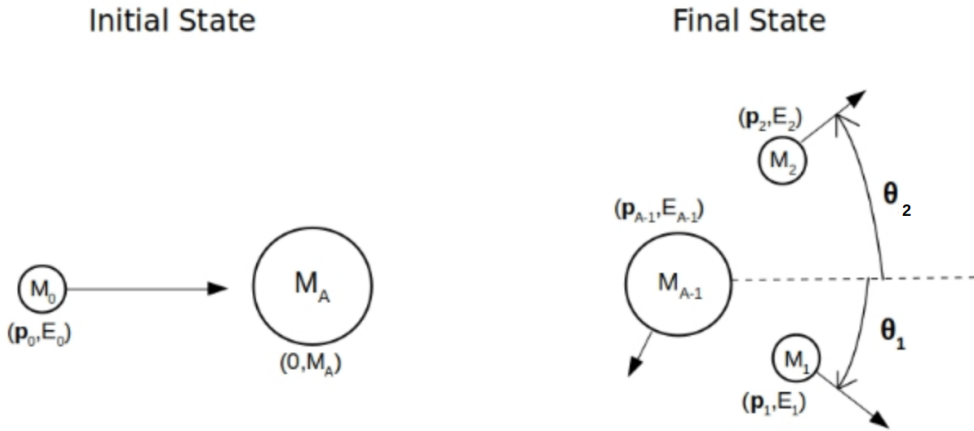


Figure 1: Simplified picture of the QFS reaction process in direct kinematics.

conservation of the reaction can be expressed as:

$$P_A + P_0 = P_1 + P_2 + P_{A-1} \quad (4)$$

with  $P_i$  the four momentum ( $E_i, \mathbf{p}_i$ ).

In direct kinematics as presented in figure 1 the separation energy of the ejected nucleon for a certain final state of the nucleus  $A-1$  is given by<sup>2</sup>:

$$S = T_0 - (T_1 + T_2 + T_{A-1}); \text{ with } T_i \text{ the kinetic energy of particle } i \quad (5)$$

In the idealized shell model the separation energy equals to the (negative) energy of the nucleus' single-particle state. In the case where the final nucleus  $A-1$  (corresponding to a one-proton knockout) remains in its ground state, its total energy in the center-of-mass frame of the initial nucleus is given by

$$E_{A-1} = M_{A-1}c^2 + T_{A-1}, \quad (6)$$

where  $M_{A-1}$  denotes the rest mass of the final nucleus and  $T_{A-1}$  its kinetic energy after the quasi-free nucleon-nucleon collision.

If a nucleon has been ejected from an inner shell resulting in a hole state, the final nucleus will be in an excited state:

$$E_{A-1}^* = M_{A-1}c^2 + T_{A-1} + E_{exe} \quad (7)$$

From the experimental point of view  $E_{exe}$  is directly accessible via gamma detection from the transition of the final nucleus from the excited to the ground state or via the detection of evaporated neutrons from higher excited states.

From momentum conservation follows that in the center-of-mass frame of the initial nucleus ( $\mathbf{p}_A = 0$ ), the recoil momentum of the nucleus in final state  $\mathbf{p}_{A-1}$  equals to  $-\mathbf{p}_i$ , the momentum of the initial nucleon inside the nucleus A pointing in opposite direction.

In addition the four-momentum of the inner nucleon can be deduced from momentum measurement of the initial and final state free nucleons:

$$P_i \approx P_{miss} \equiv P_1 + P_2 - P_0 \quad (8)$$

where  $P_{miss}$  is the so called "measured missing four-momentum of the reaction"<sup>[11]</sup><sup>3</sup>. Thereupon, the separation energy measurement and the recoil momentum distribution fully describe the single particle state in the various shell levels. In addition and as complementary method  $\gamma$  rays can be measured in coincidence with the reaction and consequently exclusive cross section and momentum distribution measurements of the single particle states are accessible.

---

<sup>2</sup>In inverse kinematics the four-momentum vectors need to be boosted to the center of mass frame of the initial nucleus via Lorentz transformation.

<sup>3</sup> $P_{miss}$  is only equal to  $P_i$  for the unperturbed QFS (no ISI/FSI) case.

Considering the removal of a single nucleon from an initial nucleus state  $\Psi_i^A$  with A nucleons and initial spin  $I$  and final nucleus state  $\Psi_f^{A-1}$  with final spin  $I_f$  an overlap function between initial and final state many-body wave function can be written as:

$$\langle \vec{r}, \Psi_f^{A-1} | \Psi_i^A \rangle = \sum_j C_j^{if} \psi_j(\vec{r}), \quad \text{with } |I - I_f| < j < |I + I_f| \quad (9)$$

where  $S_j^{if} = |C_j^{if}|^2$  is the commonly named spectroscopic factor, see ref [12] sec.2.1.  $S_j^{if}$  is summed over all final single particle states m (from  $-j$  to  $j$ ). It is unity for nucleon removal from a pure single particle state and in this picture equals  $(2j+1)$  when the nucleon was removed from a filled  $j$ -subshell. In a more realistic model the spectroscopic factor is linked to the exclusive experimental cross section measurement of a single particle state  $\sigma_{sp}(nlj)$  and the theoretical predicted one, as in ref [12]:

$$\sigma_{th}^{if} = \sum_j S_j^{if} \sigma_{sp}(nlj) \quad (10)$$

where  $\sigma_{sp}$  are the theoretical cross sections for the normalized wave functions  $\Psi_j$  of the final state nucleus A-1 with the appropriate quantum numbers.

From this considerations the spectroscopic factor can be used to probe the theoretical shell predictions. In past this was already done with direct QFS-reactions ( $e, e'p$ ). Results for the spectroscopic factor with data obtained at the NIKHEF facility are shown in figure 2. The substantial reduction of the spectroscopic factor with respect to the independent particle model (IPM) or mean field of  $\approx 35\%$  indicates a substantial depletion of the single-particle states and inferring from this a refined model prediction has to be applied<sup>4</sup>.

While QFS-reaction with electrons ( $e, e'p$ ) in direct kinematics is a valuable method to make precise measurements for stable (target) nuclei it is not suitable for the experimental analysis with exotic (neutron or proton rich) nuclei. Due to their short lifetime (e.g.  $^{52}Ca$  with  $\tau = 4.6s$ ) they can hardly serve as a target. Inducing the reaction in inverse kinematics - having electrons as targets and the exotic nuclei of interest as projectiles - is also not feasible since no free electrons can be captured as target and even more important the required center of mass energies in such an asymmetric system would require extremely high beam energies. The alternative approach is to use proton induced quasi-free scattering in inverse kinematics where the exotic beam impinges on an extended proton target such as liquid hydrogen  $H_2$  or a fixed proton rich target such as  $CH_2$ <sup>5</sup>.

---

<sup>4</sup>The mean field potential does not consider spin-spin interaction  $V_{ss}$ , non central tensor-potential  $V_T$  or spin-orbit interaction  $V_{LS}$ .

<sup>5</sup>Herefore a carbon target reference run is used to extract the QFS-reaction events from the  $CH_2$  target run.

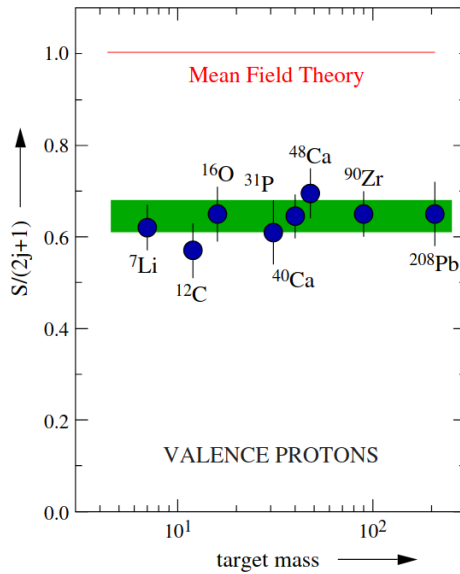


Figure 2: Normalized spectroscopic factors from the  $(e, e'p)$  reaction as a function of target mass taken from [13]. As input for the theoretical cross sections the prediction from mean field models were used.

Summarizing, the QFS-reaction technique in inverse kinematics with exotic nuclei as in-flight projectiles and a proton-like target opens new possibilities to probe theoretical model predictions of exotic nuclei far off stability which haven't been accessible before. For precise cross section measurements of the single particle states  $\sigma_{sp}$  the kinematical characteristics of the QFS-reaction products have to be considered for correct identification of QFS-events and clear background subtraction. The following descriptions are already implicitly embedded within the equation 4.

As starting point one compares the QFS-reaction of the two nucleons with the two dimensional non-central collision of free point-like particles in non-relativistic kinematics. Since both kinetic energy and momenta are conserved a clear signature is expected: the opening angle of the scattered particles is exactly  $90^\circ$ .

However, at kinetic energies of 400 AMeV and more, relativistic effects affect the opening angle of the scattered particles<sup>6</sup>. TODO: Formula to calculate directly from beam energy the opening angle...

For the final description of the process it has to be considered that the projectile nucleon inside the nucleus has a non negligible momentum (see  $P_i$  in equation 8) and in addition the separation energy  $S_{p/n}$  has to be expended to remove the scattered nucleon of the nuclear potential of the projectile nucleus.

To account for the nucleon momentum the picture of the Fermi gas model where protons

<sup>6</sup>Relativistic considerations become relevant at velocities  $\beta \gtrsim 0.1c$ . This corresponds to  $\approx 4.5$  MeV.

and neutrons freely move inside the nucleus' potential is applied. In the ground state of the nucleus the nucleons can reach a momentum up to the Fermi momentum  $p_F$ . Except for the light nuclei, the Fermi momentum is almost independent of A and amounts to  $p_F \approx 250 \text{ MeV/c}$ <sup>7</sup>. The mean quadratic momenta of the nucleons is related to the Fermi momentum by:

$$\langle \mathbf{p}^2 \rangle = \frac{3}{5} p_F^2$$
 (11)

The width of the momentum distribution of the nucleons is given in the Goldhaber model by:

$$\sigma^2 = \sigma_0^2 K(A - K)/(A - 1), \text{ with } \sigma_0 \approx 90 \text{ MeV/c}$$
 (12)

where A is the mass number of the projectile nucleus and K the mass number of the fragment after scattering. For a detailed derivation and further readings see ref. [15] and [16]. In the impulse approximation, where we assume that the interaction between the projectile and target nucleons has approximately the same form as the interaction between two nucleons in free space, the inner momenta of the scattered nucleons smear out the angular correlations of the outgoing fragment - which has the same momentum as the knocked out nucleon in the cms system of the nucleus but points in opposite direction - as well as of the two nucleons involved in the scattering. As consequence the opening angle distribution of the two scattered nucleons gets broadened as well as the azimuthal angular correlation which for the assumption of zero nucleon momentum sharply peaked at  $\Delta\varphi = 180^\circ$ .

In view of the added nucleon momentum the kinematics get expanded from a two dimensional scattering reaction to a three dimensional process where the reaction plane is determined by the plane spanned by the momentum vector of the projectile nucleus  $\mathbf{p}_A$  and the scattered nucleon after the reaction<sup>9</sup>. With the momentum measurement of the two correlated outgoing nucleons and the momentum of the incoming projectile nucleus it is possible to retrieve the internal momentum of the knocked out nucleon perpendicular to the reaction plane  $Q_{\perp i}$  via the formula derived in reference[17]:

$$Q_{\perp i} = \sin(\theta_{1/2}) \cdot \sin(\varphi_{1/2} - \varphi_{2/1}) \cdot \mathbf{p}_{2/1}$$
 (13)

In case of (p,2p) reactions it is impossible to track back the origin of each nucleon - from the projectile nucleus or the proton-like target. Inferring from this there are two possible solutions for  $Q_\perp$ . The ambiguity can be resolved by incorporating the momentum of the fragment nucleus perpendicular to the reaction plane  $Q_{\perp A-1}$ . The fragment momentum

<sup>7</sup>For light nuclei like  $^{12}\text{C}$ ,  $p_F \approx 230 \text{ MeV/c}$  can be assumed [14]

<sup>8</sup>From the derivation of the mean kinetic energy of the nucleons  $\langle E_{\text{kin}} \rangle = \frac{\int_0^{p_F} E_{\text{kin}} p^2 dp}{\int_0^{p_F} p^2 dp} = \frac{3}{5} \cdot \frac{p_F^2}{2M}$

<sup>9</sup>For (p,2p) reactions there is an ambiguity which of the scattered protons  $\mathbf{p}_1$  or  $\mathbf{p}_2$  origin from the projectile nucleus or the proton like target.

vector should be of the same amount but point in opposite direction to  $Q_{\perp i}$ . TODO: maybe insert here the plot of  $Q_{\perp}$  if possible...

Up to this point, the scattering process has been described analogously to free elastic scattering in relativistic kinematics, with the knocked-out nucleon assumed to possess a non-negligible initial momentum inside the nucleus. However, it must be noted that the ejected nucleon is an off-shell particle, bound within the nuclear potential. Its virtual mass  $\mu_i$  in the c.m.s. of the nucleus is given by:

$$\mu_i = \sqrt{m_A^2 + m_{A-1}^2 - 2m_A \sqrt{m_{A-1}^2 + |\mathbf{p}_i|^2}} \quad (14)$$

where  $m_A$  and  $m_{A-1}$  are the rest masses of the initial nucleus and the residual fragment after the quasi-free scattering, respectively, and  $\vec{p}_i$  denotes the momentum of the inner nucleon in the c.m.s. of the nucleus, see also equation 8. From equation 14 follows:

$$0 < \mu_i < m_n \quad (15)$$

where  $m_n$  is the mass of the appropriate free nucleon. To knock the bound nucleon out of the nucleus the separation energy has to be overcome which can be observed in the reduced opening angle of the two outgoing correlated nucleons.

### 2.5.2 Cross Sections for QFS Reactions - Qualitative Considerations

TO DO: see more in the standard work [8], [9].

### 2.5.3 Application Fields of QFS Reactions

Over several decades of experimental and theoretical research, Quasi-Free Scattering (QFS) reactions have been firmly established as a powerful and direct tool for probing the microscopic structure of atomic nuclei. These reactions provide critical insights into nuclear correlations, single-particle properties, and the momentum distributions of nucleons within the nucleus.

The versatility of QFS extends across various applications, including the study of short-range nucleon-nucleon interactions, exotic nuclear states, and the modification of nucleon properties in nuclear matter. Advances in experimental facilities and state-of-the-art detector systems, have significantly improved the precision and scope of QFS measurements. These developments have enabled in-depth investigations of nuclear dynamics, the structure of unstable isotopes, and fundamental aspects of quantum many-body systems, contributing to a deeper understanding of nuclear and sub-nuclear phenomena.

This subsection will point out the most exciting and promising application fields of QFS

reactions with focus on the applicability in the R<sup>3</sup>B experimental setup. A detailed review can be found in ref [18].

**Single-Particle Spectroscopic Strength** As already mentioned in section 2.5.1 in many experiments a reduction in the spectroscopic strength of about 35% with respect to the independent particle model (IPM) and shell model predictions was observed. In one-nucleon removal reactions - experiments with isotope beams impinging on a composite nuclear target - the extraction of the missing spectroscopic strength is challenging as the kinematical pattern is highly complex. In contrast, the QFS reactions mechanism in inverse kinematics retains a clear kinematical signature which makes it a valuable tool to study the quenching of the spectroscopic strength which originates from residual correlations between bound nucleons inside the nucleus.

Several experiments were carried out at the GSI Facility to study the reduction factor of the spectroscopic strength and its evolution over a broad range in isotopic chains, in light nuclei such as for oxygen shown in figure 3. With the commissioning of the SIS100 and SuperFRS at GSI it will be achievable to study (p,2p) reactions with very short lived nuclei also in heavier systems at reasonable intensities which will presumably draw even more attention to QFS reaction approach.

**Gamma Spectroscopy** Alongside to the study of the single-particle spectroscopic strengths QFS reactions provide valuable information of the shell structure and deformation of the fragment (A-1) via gamma spectroscopy. QFS reactions with nucleons in inner shells result in bound (or unbound) excited states of the (A-1) fragment. The excited fragment promptly decays to its ground state either through the emission of a Doppler-shifted  $\gamma$ -ray, or – if the excitation energy exceeds the particle separation threshold – via the emission of a proton or neutron. A big advantage of the (p,2p) reaction experiments is the ability to make precise vertex reconstruction by accurate measurement of the two outgoing correlated protons. This is of particular importance for extended targets and determines the emission point within the target, enabling an accurate calculation of the fragment's velocity and therefore a precise Doppler correction.

From gamma spectroscopy the excitation energy E(2+), often the first excited state in even-even nuclei, can be observed which is a fundamental observable of nuclear structure, providing key insights into the shell configuration and deformation of the nucleus[18]. Especially when going towards exotic neutron rich isotopes the study of the gamma emission lines can strongly contribute to the understanding of nuclear shell evolution.

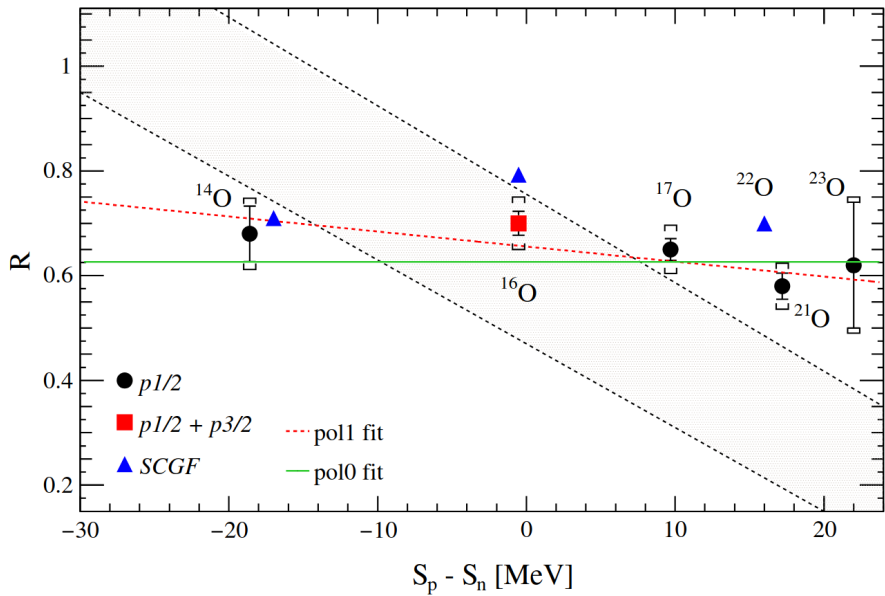


Figure 3: Extracted reduction factors of the spectroscopic strength from (p,2p) measurements (circles and square) as a function of the difference between proton and neutron separation energy  $S_p/S_n$ . The blue triangles correspond to the predictions from self-consistent green functions (SCGF). The shaded area indicates a trend from an analysis of one-nucleon removal cross sections in other reactions and which lead to an intense discussion in the field. From Ref. [19].

**QFS to probe inner clustering and halo formation** Clusterization inside nuclei is a phenomenon widely observed in experiments with large implications on astrophysics processes such as the synthesis of carbon inside stars via triple  $\alpha$  clusterization [20],  $\alpha$  - radioactivity, or the evolution of core collapse supernovae[21], just to mention some. Its presence has also to be implemented in the state of the art equation of state calculations.

Single-particle cluster states can be directly accessed via QFS ( $p,p\alpha$ ) reactions. In the low energy regime of 100 AMeV the  $^{12}\text{C}(p,p\alpha)^8\text{Be}$  reaction, see ref [22], as benchmark study approved the reaction mechanism and up to a scaling factor the measured cross sections aligned exceptionally well to the free  $p-\alpha$  scattering measurements.

Moreover the QFS mechanism allows to access light nuclei going towards the neutron drip line via ( $p,pn$ ) reaction. These light nuclei are mostly weakly bound with an extended low density neutron-matter distribution forming a so-called *nuclear-halo*.

The most prominent candidate for such is  $^{11}\text{Li}$ , often called *Borromean three-body system*, consisting of two neutrons interacting with a core ( $^9\text{Li}$ ) via weak, short-range interactions [23]. First evidence for the correlation between the two neutron was strongly pushed by experimental studies at GSI, see [24], and theoretical work by Bertulani et. al.[25].

The latest experiment with the focus on the study of multi-neutron correlations in drip-line nuclei was carried out at R<sup>3</sup>B in 2022 (experiment S509) probing broad isotopic chains of Li, Be, B, C and N via the QFS mechanism, and first results are expected to be published in the near future.

**Short Range Correlations(SRC)** Short range correlations refer to elementary nucleon-nucleon interactions within a nucleus and occur over very short distances, typically on the order of 1-2 femtometers. These correlations are characterized by pairs of nucleons with high relative momentum ( $> k_F$ , Fermi momentum) and low total momentum. These NN-interactions are treated as good explanatory candidate for observed deviations from mean field approximation. Many phenomena, such as the above discussed reduction in the spectroscopic strength and the EMC effect[26], the observation that the cross section for deep inelastic scattering from an atomic nucleus is different from that of the same number of free protons and neutrons, are associated to the short range correlations inside the nucleus.

From isotopic chain studies[27] it has been shown that there is an indication of SRC dependency on isospin, see figure 4, where SRC are predominately preferred by p-n pairs than by nn or pp pairs. This again can have significant impact for

asymmetric nuclei and imply a stronger quenching of the spectroscopic strength for proton single particle states below the Fermi momentum for neutron rich matter.

Since pioneering experiments were made at JLab and Brookhaven via  $(e, e'p)$  and  $(e, e'n)$  reactions several experimental campaigns were carried out at GSI with the R<sup>3</sup>B setup probing the QFS reactions via the strong nuclear force instead of the Coulomb interaction. Also in 2022 the S522 experiment was performed to exploit for the first time the use of short-lived nuclei scattering off a proton probe in inverse kinematics at R<sup>3</sup>B, followed by the S091 experiment in 2024 with the focus on probing NN-correlations in atomic nuclei via  $(p, pd)$  QFS reactions[28].

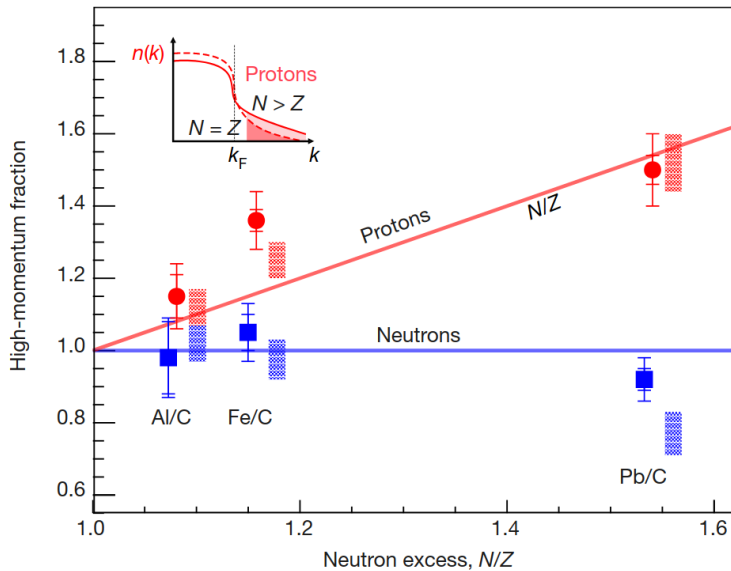


Figure 4: Fraction of high-momentum neutrons and protons with respect to the N/Z ratio for several carbon isotopes. A clear trend towards high momentum proton distribution for neutron rich carbon isotopes (red line) is shown, while the high momentum neutron distribution stays constant with respect to the N/Z ratio (blue line). From reference [27].

**Fission via QFS** Fission induced via quasifree scattering (QFS) provides a powerful method to extract fission barriers on an event-by-event basis. The fundamental concept involves the knockout of a proton or neutron from an incoming exotic ion beam. By measuring the energy and the angular distribution of the correlated emitted nucleons, it becomes possible to probe the excitation energy transferred to the fissioning system. In cases where deeply bound nucleons are knocked out, the resulting daughter nucleus either evaporates one or multiple neutrons or populates

an excited state, which can be experimentally observed. The R<sup>3</sup>B setup is particularly well-suited for such investigations, as it enables full kinematic reconstruction of the reaction products and hence to pin down the complete reaction mechanism. This approach allows for the detailed exploration of the potential-energy surface and the fission dynamics across a broad range of fissility and excitation energies, taking advantage of relativistic radioactive beams.

The pilot experiment S455 was conducted in 2021 at R<sup>3</sup>B using a stable <sup>238</sup>U beam incident on a liquid hydrogen target. The data collected from this experiment provide simultaneous information on several key fission observables, which can be used to constrain theoretical calculations. These calculations aim to describe both the static and dynamic properties of the fission process and enable comparisons with predictions from various theoretical frameworks, including phenomenological approaches, macroscopic-microscopic models, and fully microscopic statistical or time-dependent Hartree-Fock calculations.



### 3 Experiment

The here experiment mainly being investigated in the framework of this thesis was performed in 2020 in the FAIR Phase-0 campaign at GSI (Gesellschaft für Schwerionenforschung) in Darmstadt (Germany). The GSI operates a unique accelerator facility for heavy ions and focuses on several cutting-edge research fields. These include:

1. **Nuclear Physics:** Studying the properties of atomic nuclei, exploring the forces that bind protons and neutrons, and investigating exotic nuclei far from stability. This effort involves major international collaborations, including HISPEC/DESPEC, which investigates the structure of atomic nuclei through high-resolution spectroscopy [29], and the R<sup>3</sup>B Collaboration, which focuses on kinematically complete measurements of nuclear reactions. An important aspect of this field also includes the discovery of new elements. Notably, experiments at the GSI accelerator facility have led to the identification of superheavy elements with atomic numbers 107 to 112 [30].
2. **Hadron and Quark Matter:** Investigating the behavior of hadrons (particles made of quarks) and the state of matter under extreme conditions, such as those found in neutron stars or during the early universe, see e.g. HADES experiment [31].
3. **Atomic Physics:** Examining the structure and dynamics of atoms, including highly charged ions, to understand fundamental atomic interactions and refine quantum electrodynamics, see e.g. [32]. This includes also the field of superheavy element chemistry which make nuclear studies of the heaviest man-made elements.
4. **Plasma Physics:** Creating and analyzing high-energy-density plasmas to simulate conditions found in stellar interiors and other astrophysical phenomena, see e.g. PHELIX laser facility [33].
5. **Biophysics and Medical Research:** Exploring the effects of ion beams on biological systems for applications in cancer therapy, particularly using heavy ion therapy, and studying radiation protection for space missions.
6. **Materials Research:** Investigating the response of materials to high radiation doses to develop more resilient materials for use in various technologies, including nuclear reactors and space exploration.

### 3.1 GSI facility

The GSI Helmholtzzentrum für Schwerionenforschung GmbH was founded in 1969 (as "Gesellschaft für Schwerionenforschung mbH) looks back on a successful research history. In the time between 1981 and 2010 six new superheavy elements were discovered<sup>10</sup>. In the medical research field GSI has developed advanced cancer therapy techniques using heavy ion beams which target tumors with high precision, minimizing damage to surrounding healthy tissues.

Along with those groundbreaking discoveries in research the facility at GSI has always been an inspiring source of drive for new technologies.

The key devices and apparatus enabling heavy-ion experiments at GSI makes it to one of the most advanced accelerator facilities in the world.

The starting point for the production of relativistic heavy ions at GSI is a set of different ion sources where ions are generated by stripping electrons off the shell of the atoms. Depending on the experimental needs the ion sources at GSI are able to produce ions of all different stable elements (up to Uranium)[35]. The only limitations arise from safety regulations, which currently prohibit the use of toxic primary beams, such as thallium (Tl).

On the first acceleration stage the stable primary ions are injected from the ion source into the UNIversal Linear Accelerator (UNILAC). On a length of 120 meters ions are accelerated up to maximum energy of 11.4 AMeV. The low energy beam can be either directly used or being injected into the ring accelerator SIS18 (Schwerionensynchotron 18). Here the ion beam is further accelerated up to 4.7 GeV/u (for protons) / 1 GeV/u (for Uranium). The magnets and the ultra-high vacuum ( $\sim 10^{-9}$  Pa) keep the ions well on their circular path (SIS18 has a circumference of 216 meters)[36]. For the production of rare heavy isotopes the primary ion beam from SIS18 can be impinged on a light nuclear target, e.g beryllium, the so called production target. The secondary beams of radioactive isotopes are typically purified in the FRagment Separator (FRS). The FRS as a high-resolution magnetic spectrometer is capable to precisely select specific isotopes and to forward the desired beam of exotic relativistic nuclei to the various experiments or direct it to the ESR for later use.

---

<sup>10</sup>A comprehensive overview work of five decades of GSI superheavy element discoveries can be found here [34]

### 3.1.1 FAIR Project

The Facility for Antiproton and Ion Research (FAIR) will extend these capabilities significantly and will be one of the most advanced and extensive accelerator complexes in the world. The construction of the superconducting ring accelerator SIS100, with a circumference of 1.1 km, along with associated storage rings and experimental sites, began in the summer of 2017. The commissioning of parts of the facility is planned for 2027, followed immediately by the Early Science Program.

The so-called First Science Phase, which will mark the full operation of SIS100 and the complete commissioning of FAIR equipment, will be the next step. Prior to the commissioning of SIS100, several high-priority experiments with significant scientific impact will take place as part of the Early Science Program in the newly established experimental halls. These include experiments utilizing the R<sup>3</sup>B setup in the High-Energy Cave (HEC), focusing on key aspects of nuclear structure and reactions under extreme conditions.

## 3.2 R<sup>3</sup>B Setup

The R<sup>3</sup>B (Reactions with Relativistic Radioactive Beams) experiment currently still operated in Cave C at the GSI is a cutting-edge research experiment focused on the study of nuclear reactions and structure using high-energy radioactive ion beams. The experiment aims to investigate exotic nuclei far from stability, offering insights into the fundamental properties of nuclear matter, nucleosynthesis processes, and the forces governing nuclear interactions. A schematic overview of the R<sup>3</sup>B setup can be seen in Figure 5.

Short living isotopes are injected to the Cave C from the FRS, which preselects the isotopes of interest, and impinge on a fixed target. The R<sup>3</sup>B setup is designed for kinematically complete reaction studies. To fulfill this requirement the incoming ions are tracked and identified on an event-by-event basis by dedicated detectors in the FRS via time-of-flight and  $\Delta E$  measurement techniques [37]. Depending on the settings and composition of the incoming ion beam different type of reactions take place in the target area with a large variety of reaction products: heavy ions (as products from fission/spallation reactions), neutrons, light charged particles and gamma rays. For the detection of gammas and light charged ions from reactions with the target the dedicated CALIFA calorimeter (see more in section 3.3.5) and various tracking detectors are installed in the target region. The GLAD (GSI Large Acceptance Dipole) magnet, located at the center of the Cave C, allows fragment identification for the forward boosted charged reaction residues. The magnetic rigidity of the charged reaction

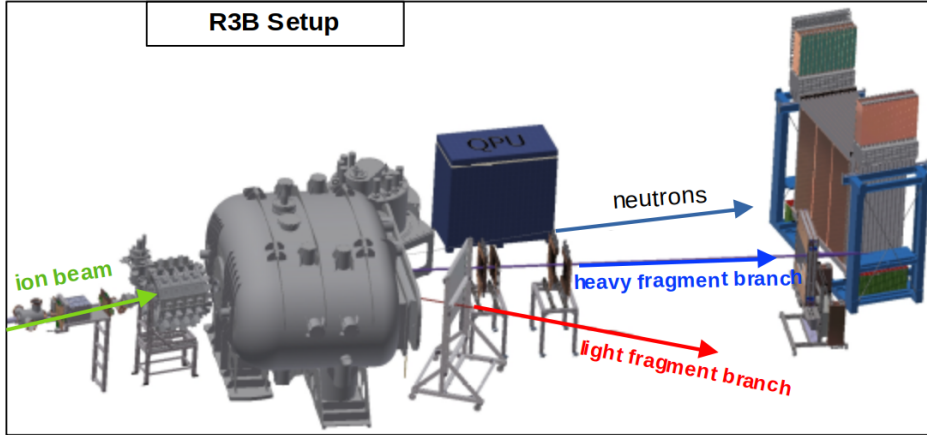


Figure 5: Overview of the  $R^3B$  setup in Cave C with detectors for the specific fragment branch identification.

residues is measured by a combination tracking detectors and a time of flight wall after the GLAD magnet. This allows to identify the charged reaction residues and their momenta. For the detection of the neutrons, not deflected by the magnetic field of GLAD, the new Large-Area Neutron Detector (NeuLAND) is positioned after GLAD on the zero degree line with the incoming ion beam.

The  $R^3B$  setup offers high flexibility, allowing operation both in vacuum and in atmospheric conditions. Over the past few years, during the so-called *Phase-0*, numerous experiments have been conducted, each utilizing different configurations and newly developed or upgraded detector systems.

The combination of a broad spectrum of incoming ion beams across a wide energy range, provided by the FRS facility, and the versatility of the  $R^3B$  setup – equipped with state-of-the-art detectors tailored for specific physics studies – makes it an exceptional platform for experimental nuclear and astrophysics.

### 3.3 Detector Setup in S444 Commissioning Experiment 2020

The S444 Experiment (successor experiment of the FAIR Phase-0 program in 2019, see ref. [38]) for the commissioning of the CALIFA Calorimeter in its final mechanical design took place in February 2020. The choice to operate with stable  $^{12}C$  primary beam with four beam energy settings - 400/550/650/800 AMeV gave the opportunity to use it as preparation for the following up S467 experimental run with neutron-rich  $Ca$  isotopes as medium-heavy incoming beam. The detectors for ion tracking, charge identification and time of flight measurement were provided by the SOFIA(Study on Fission with ALADiN<sup>11</sup>) collaboration. These detectors are optimized for fission ex-

<sup>11</sup>ALADiN magnet was the predecessor of GLAD.

periments with medium to heavy reaction fragments. As for the S444 experiment with primary  $^{12}\text{C}$  incoming beam no fission reaction with multiple heavy charged fragments is expected the Sofia detectors were adapted accordingly (e.g. only one of the four sections of the Twin-Music Ionization chamber was operated, see more in section 3.3.2). For this experiment, most detectors and components of the setup were operated in air. The target chamber, as well as the GLAD magnet, was filled with gaseous helium at room temperature to reduce scattering of the ions.

However, the presence of gas, detectors and window material in the setup leads to ion interactions, causing angular straggling in the flight path reconstruction. This effect can limit the resolution of the reconstructed momenta from reactions occurring at the target.

In the following sections the different detector components and their properties are discussed.

### 3.3.1 Multi Wire Proportional Chambers (MWPC)

The positional tracking of the incoming ions as well as the charged reaction products were performed by using Multi Wire Proportional Chambers (MWPCs). A MWPC operates on the principle of proportional counters that are arranged side by side in a plane, thereby providing spatial resolution for particle radiation. The multi wire proportional chambers were developed in late 1960s by George Charpak<sup>12</sup> at CERN[39]. The MWPC operates in the same way as aligned proportional counters with the difference of not having additional walls between the anode wires. This reduces the material budget, hence improving the spatial resolution and reducing reactions with the detected particle.

In the general design the MWCP is made up of a plane of anode wires enclosed between two cathode planes which are aligned parallel to the anode wire plane. Depending on the beam conditions the anode wires are set to high voltage ( $\sim 1100$  V) while the cathode planes are grounded.

The volume between the two cathode planes is filled by a gas mixture of 84% Argon and 16%  $\text{CO}_2$ . The decision of the gas mixture is driven by a balanced ratio between amplification and quenching proprieties of the gas.

When a charged particle passes through the detector it ionizes the gas. Primary electrons are created followed by a secondary ionization. The electron cloud drifts towards the wires (anodes) while the positive ions drift towards the grounded cathode planes.

---

<sup>12</sup>George Charpak received the Nobel Prize in Physics in 1992 for his invention and development of particle detectors, in particular, the multi-wire proportional chambers.

Close to the anode wire the electric field is high enough that the primary electrons scattered off gas molecules can create an avalanche of secondary electrons to amplify the signal. As the MWPCs are operated in the proportional region, the number of created electrons/ions is proportional to the initial ionization. Instead of reading out the signal from the wires it is read out from the strips of the cathode plane, see figure 6. This improves the position resolution in case multiple (neighboring) strips give signal. The signal distribution over the strips is analyzed and fitted to provide the position information.

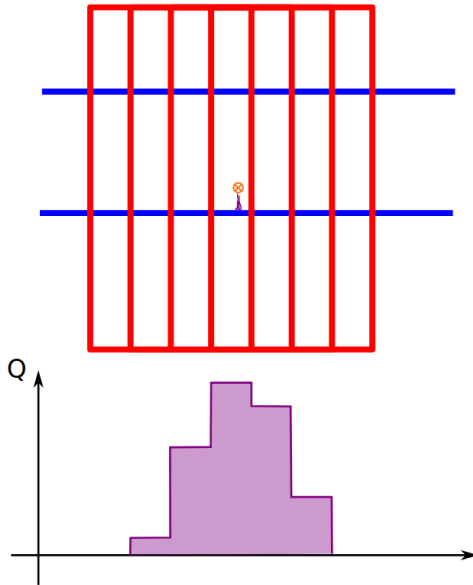


Figure 6: Schematic representation of the charge distribution when reading out the signal from the cathode pads (red) instead of the anode wires (blue). The red cross symbolizes the incident ion.

In the R<sup>3</sup>B setup for the S444 experiment four MWPCs were installed:

1. MWPC0: right at the beginning of the beam entrance in Cave C, 184 cm upstream to the target position to detect x- and y positions of the incoming ions.
2. MWPC1: 88 cm downstream to the target for positional tracking in x and y of the outgoing ions and reaction products.
3. MWPC2: 154 cm downstream also for positional tracking in x and y of the fragment.
4. MWPC3: after the GLAD magnet. The x position of this detector gives the information about the magnetic rigidity of the reaction fragment.

Despite having the same mode of operation, they slightly differ in their construction design and positional resolution. The primary distinction lies in the active detection area: while MWPC0, MWPC1, and MWPC2 each feature an active area of  $400 \text{ cm}^2$ , MWPC3 covers a significantly larger area of  $5400 \text{ cm}^2$ . This extended coverage is required to track ions and reaction products that are deflected within the GLAD magnet according to their momentum-to-charge ratio. For the technical specifications of the individual MWPCs, see table 1.

Common MWPC Settings	
Gas	84% Ar, 16% CO <sub>2</sub>
Windows	Mylar®, 12μm
Anode wires voltage	1100 V
Cathode planes voltage	Ground
Wire pitch	2.5 mm
Wire diameter	5 μm
Width of X pads	3.125 mm

MWPC0	
X pads	64 pads, vertically segmented into two equal parts
Y pads	64 pads, horizontally segmented (3.125 mm width)
Active surface	$200 \times 200 \text{ mm}^2$

MWPC1 & MWPC2	
X pads	64 pads, vertically segmented into two equal parts
Y pads	40 pads (5 mm width), horizontally segmented
Active surface	$200 \times 200 \text{ mm}^2$

MWPC3	
X pads	288 pads
Y pads	120 pads (5 mm width)
Active surface	$900 \times 600 \text{ mm}^2$

Table 1: SOFIA MWPCs - Technical specifications

### 3.3.2 Ionization Chambers - R<sup>3</sup>B Music/TWIN Music

For the S444 experiment at R<sup>3</sup>B two types of Multi Sampling Ionisation Chambers (MUSICs) were installed: the R<sup>3</sup>B MUSIC, centered 153 cm upstream to the target,

and the TWIN MUSIC, 132 cm downstream to the target. Like the MWPCs (see 3.3.1) the ionization chambers are gas-filled detectors for tracking charged particles. While MWPCs consist only of a few mm of active gaseous volume, the initiation chambers have an expanded gaseous volume which allows to make precise energy loss measurements from the ionization process in the gas. The multi sampling initiation chambers consist of a cathode plane, a Frisch grid and an anode plane, with a series of anode strips. When a charged particle crosses the chamber the gas gets ionized along the trajectory and the created electrons and ions are separated by the strong electric field. While the ions drift towards the cathode plane the electrons move to the anodes where each anode is read out separately. Since the energy loss of the passing through fully stripped ions is proportional to the square of its nuclear charge ( $\Delta E \sim Z^2$ ) the signal from the anodes allow to precisely measure the charge of the particle. Moreover multi-sampling ionization chambers measure the drift time of the electrons created by the ionization process on each anode (compared to one or more reference anodes). Assuming a constant electron drift velocity ( $v_{drift} \sim 40\text{mm}/\mu\text{s}$ ) over the gaseous volume the time information of each anode signal can be used to reconstruct the position along the electric field of the passing through particle.

### R<sup>3</sup>B MUSIC

The R<sup>3</sup>B MUSIC, installed 153 cm upstream to the target, is used to measure both the charge of of the incoming ion before impinging on the target and the angle of the particle's trajectory. The detector has an active gaseous dimension of 20 x 20 x 40 cm<sup>3</sup>, confined on one side by a cathode plane and on the other side by an anode plane segmented in 10 anodes ( 8 readout anodes and 2 screen anodes). For the technical specifications, see table 2.

---

<b>Dimensions</b>	
Detector dimension:	51 x 54 x 53 cm <sup>3</sup>
Active dimension:	20 x 20 x 40 cm <sup>3</sup>
Dimension of one anode:	20 x 20 x 5 cm <sup>3</sup>
Dimension of one screen anode:	20 x 20 x 2 cm <sup>3</sup>
<b>Gas</b>	
P75 (Ar 25%, CH <sub>4</sub> 75%)	
<b>Voltage</b>	
Cathode (left to beam direction):	-(2 - 6)kV
Anode (right to beam direction):	+300V

---

Table 2: R<sup>3</sup>B MUSIC - Technical specifications

## TWIN MUSIC

The TWIN MUSIC is a double ionization chamber with one central cathode plane and two independent horizontal drift volumes and anode planes on each side. Each of the anode planes consists of 16 anodes for readout plus two screen anodes. Furthermore each anode is again segmented into up/down which splits the detector into four dedicated sections. As the TWIN MUSIC is placed 132 cm downstream to the target it is employed to measure charge and angular direction of the outgoing medium-to-heavy fragments. The detector was designed for the requirements in fission experiments where two or more fission fragments are created. If each fragment is flying through one of the four sections (which is mostly the case due to momentum conservation rules) charge and angle of each fragment can be measured independently.

To fulfill the required permanence of the field in both extended gaseous volumes (of dimension 11x22x40 cm<sup>3</sup>) a Frisch grid is located 3 mm from the anode planes. The Frisch grid is metal mesh grid that shields the anode from the movement of ions produced during ionization process in the chamber ensuring that only the electrons that reach the anode contribute to the signal. Additionally, the shielding of the anodes by the Frisch grid account for the fast rise time of the signal at the anodes which diminishes pile-up effects and makes the detector high beam-rate capable (up to 100kHz). Further technical specifications you can find in table 3.

---

### Dimensions

Detector dimension:	43 x48 x55 cm <sup>3</sup>
Active dimension:	two halves, each 11x22x40 cm <sup>3</sup>
Distance central cathode - Frisch grid:	11 cm
Distance Frisch grid from anode planes:	3mm

### Gas

CH4 [79%], Ar [20%] and CO2 [1%]

### Voltage

Central cathode:	-(2 – 6)kV
Anode planes:	+600V
Frisch Grid:	+250V

### Resolutions

$\Delta E/E$	< 5% FWHM, total < 2% FWHM
$\Delta X$	< 40 $\mu$ m

---

Table 3: TWIN MUSIC - Technical specifications, see also [40]

### 3.3.3 Sofia Start Detector

The SOFIA Start detector is positioned right after the R<sup>3</sup>B MUSIC ionization chamber and gives a time reference for the incoming ion. It is a 1 mm thin scintillating plastic blade attached with a photo multiplier tube on each side. The scintillator light from excitation of the incoming ions produce a clear CFD signal on both photomultiplier tubes used for the time measurement:

$$t_{start} = 0.5 \cdot (t_{left} + t_{right})$$

To shield the plastic detector from daylight it is wrapped in Mylar foil (300 $\mu\text{m}$  thickness).

### 3.3.4 GLAD Magnet

The **GSI Large Acceptance zero degree superconducting Dipole magnet GLAD** sits in the center of the R<sup>3</sup>B setup in the Cave C, see figure 7. Its adjustable field integral up to 5 Tm and a high acceptance range are crucial for the identification of highly asymmetric reaction fragments. The homogeneous magnetic field in GLAD allows to achieve momentum resolutions  $\Delta p/p$  of 10<sup>-3</sup> in combination with the dedicated tracking system.

The large opening angle of  $\pm 80$  mrad makes the GLAD magnet highly transmissive for evaporated or scattered neutrons in the reaction process which will be subsequently detected in the NeuLAND detector.

The default bending angle of the beam with respect to the beam line was set to 18°. Herefore the currents where adjusted according to the different beam energies:

1. 400 AMeV beam: 1444 Ampere
2. 550 AMeV beam: 1778 Ampere
3. 650 AMeV beam: 1957 Ampere
4. 800 AMeV beam: 2223 Ampere

### 3.3.5 CALIFA Calorimeter

The **CALOrimeter for In Flight detection of  $\gamma$ -rays and high energy charged pArticles**, CALIFA, is one of the main detector components of the R<sup>3</sup>B setup. It surrounds the target area and covers the full azimuthal range and a polar angular acceptance from 7° up to 140° in the target region in its final configuration. The calorimeter serves for the detection of gamma rays in the energy region 100 keV  $\lesssim E_\gamma \lesssim$  30 MeV and light charged



Figure 7: Upstream view of GLAD magnet in the center of Cave C after installation in February 2016. Picture from [41]

particles, mostly protons, up to  $E_p \lesssim 700$  MeV. To fulfill the demands requested by the different experimental campaigns an energy resolution of  $\frac{\Delta E}{E} \sim 6\%/\sqrt{E[(MeV)]}$  (FWHM) in the gamma-ray energy regime is achieved. For proton energies in the range  $100 \leq E_p \leq 300$  AMeV, the corresponding energy resolution is approximately  $\frac{\Delta E}{E} \sim 1\%/\sqrt{E[(MeV)]}$ .

## Geometry

The CALIFA detector is a highly segmented detector with 2544 CsI(Tl) crystals installed in the final design. Since experiments in the R<sup>3</sup>B setup operate in relativistic kinematics both the incoming ions as well as the measured particles originating from reactions experience relativistic effects, more precisely the relativistic Doppler effect. The emitted gamma rays and protons are not isotropically distributed around the source region but are instead boosted in the forward direction. Furthermore, the energy measured in the laboratory frame differs from the kinetic energy in the rest frame of the incoming ion due to relativistic effects.

The relativistic Doppler effect has a huge impact on the geometric design and requirements of CALIFA. Therefore the detector was subdivided into two polar angle ranges 8:

### 1. BARREL

- $43^\circ \leq \theta \leq 140^\circ$  - Barrel: This segment covers the region where the lowest rates and energies are expected. The Barrel region contains 1952 CsI(Tl) crystals. The most forward crystals have a length of 22 cm (which allow to

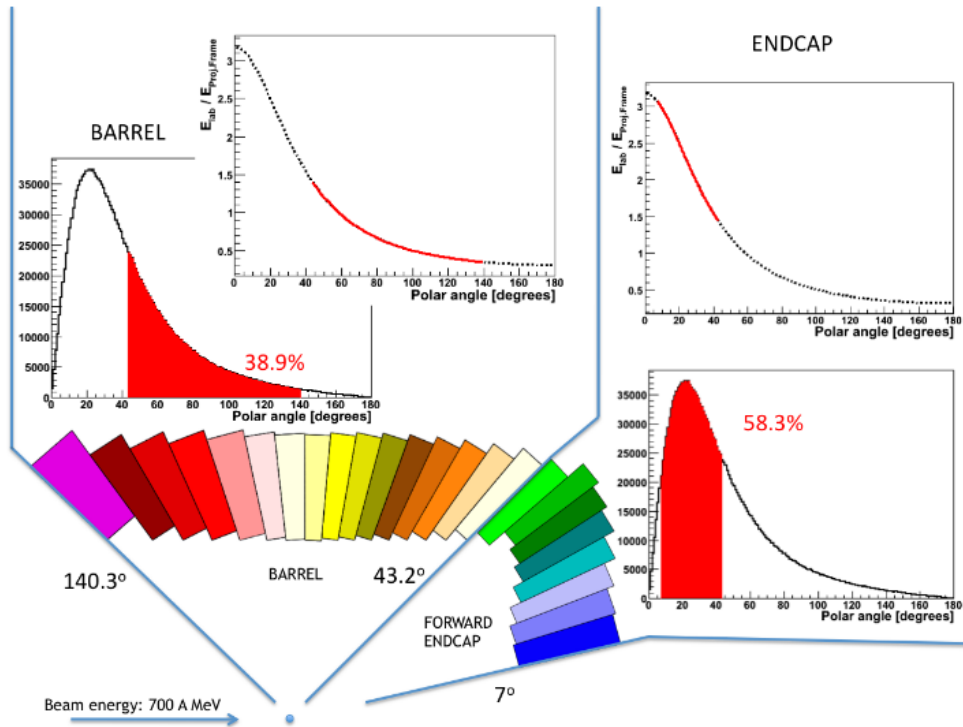


Figure 8: Schematic view of the Barrel and Endcap(iPhos and CEPA) segments of CALIFA and the according angular and energy distribution of emitted  $\gamma$  rays (isotropic and mono-energetic in the projectile frame at beam energy of 700 AMeV). From [42]

stop protons with  $E_{kin,p} \leq 315\text{MeV}$ ). This length is reduced down to 12 cm for the most backward crystals (For more information see Barrel TDR:[42]).

## 2. ENDCAP

- $19^\circ \leq \theta \leq 43^\circ$  - Intrinsic Phoswich (iPhos): In conjunction with the CEPA, the iPhos region forms the CALIFA Endcap. The iPhos region is, same as for the CEPA, affected by high rates. Protons reaching this region have high kinetic energies and therefore a significant fraction of "punch-throughs" is expected. In the iPhos region 480 CsI(Tl) crystals with a length of 22 cm<sup>13</sup> are installed and cover each an average polar angle of  $\theta \approx 3^\circ$ .(For more information see Endcap TDR:[43]).
- $7^\circ \leq \theta \leq 19^\circ$  - CEPA (CALIFA Endcap Phoswich Array): The most forward segment consists of 112 CsI(Tl) crystals. Due to the aforementioned relativistic Doppler effect this area will have the highest intensities and energies. For high beam energies most of the particles will not be stopped inside the crystal and will escape as "punch-throughs". Despite the "punch-through" where ions deposit only a fraction of their kinetic energy ( $\Delta E$ ) in CALIFA, it is possible to reconstruct the initial energy of the particle <sup>14</sup>. In CEPA crystals with a length of 22 cm are used, each covering specific polar angle ranges to ensure optimal geometrical coverage. The finer segmentation in the polar angular range provides the advantage of compensating for high event rates while enabling high-resolution Doppler correction.

The crystals are arranged in groups of four in one carbon fibre alveolus with a nominal wall thickness of  $230\text{\mu m}$ [42] that provide a support structure for the crystals and keep the material bunched as low as possible. The alveoli in turn are held and covered by individual aluminum tiles. From the backside the volume enclosed by the alveoli and the aluminum tiles is flooded with nitrogen to keep humidity low on the surface of the crystals. For a sufficient suspension of the aluminum cover a robust external holding structure was designed, see figure 9.

In 2019 CALIFA was for the first time integrated into the R<sup>3</sup>B setup in form of the CALIFA demonstrator, a prototype consisting of seven mechanically separate petals,

---

<sup>13</sup>To fully stop protons with  $E_{kin,p} \approx 600\text{AMeV}$  crystals with a length of 60 cm would be needed. Such long crystals would have multiple drawbacks: reduced energy resolution due to worse scintillator light transport, enhanced nuclear reactions inside the crystals and challenging demands on stability of the detector holding structure

<sup>14</sup>This is done by exploiting the distinct scintillation components of CsI, see more in chapter 5 of [44]



Figure 9: Simulated view of the R<sup>3</sup>B setup installed in the High-Energy Cave (HEC) at FAIR. The support structures for the CALIFA detector are shown in yellow and green in the lower left part of the image. © GSI/FAIR, Zeitrausch.

each of it containing a set of 64 crystals.

At the end of 2019 the CALIFA frame in its final design was installed and the forward barrel part ( $43^\circ \leq \theta \leq 90^\circ$  and full azimuthal coverage) was equipped with 1024 crystals.

For the S444 and the S467 experiment in 2020 CALIFA was equipped with 180 more crystals in the iPhos region ( $19^\circ \leq \theta \leq 43^\circ$ ) which corresponds to a coverage of 37.5 % in azimuthal angle for that region. Right before the S455 fission experiment [45] the full installation of the iPhos region was completed.

In February 2024 the full CEPA region ( $7^\circ \leq \theta \leq 19^\circ$ ) with 112 crystals was commissioned for the first time together with a new equipped part of the backward barrel ( $90^\circ \leq \theta \leq 102.5^\circ$ , 128 crystals).

#### **Energy and particle reconstruction with CsI(Tl) scintillator crystals**

Scintillator material, as caesium iodide doped with thallium CsI(Tl), is widely used in experimental physics to detect ionizing radiation from  $\gamma$ - rays or charged particles. A comprehensive overview of scintillation mechanisms and the corresponding models can be found in Ref. [46] and more detailed literature in Refs. [47, 48].

Thallium-doped Cesium Iodide produces light with a peak emission around 550 nm (green light) and has a high light output<sup>15</sup>. The high density of CsI with 4.51 g/cm<sup>3</sup>

---

<sup>15</sup>The light output per MeV deposited energy in CsI(Tl), measured in [49], resulted in  $5.2 \cdot 10^4$

makes it to an optimal scintillator material to efficiently absorb  $\gamma$ - rays and high-energy particles. Moreover the CsI(Tl) crystal is well transparent to its own scintillation light, which is essential for the transport and consequent detection of the scintillator light. CsI(Tl) crystals are in addition relatively robust compared to other crystals and only slightly hygroscopic making them suitable for long-term use in experimental setups. In a first approximation, the total amount of emitted light is proportional to the energy deposited in the scintillator. For  $\gamma$ -rays this is valid for  $E_\gamma \gtrsim 400\text{keV}$ [50]. However, for charged particles significant deviations from linearity are observed, a so-called *quenching*[47].

Although the the energy calibration of CsI(Tl) crystals for charged particles is challenging, CsI(Tl) as such has the beneficial property of having a complex time dependent light emission consisting of multiple distinct exponential components. The dominant time dependent light emission response of CsI(Tl)  $L(t)$  can be approximated as:

$$L(t) = \frac{N_f}{\tau_s} \exp(-\frac{t}{\tau_f}) + \frac{N_s}{\tau_s} \exp(-\frac{t}{\tau_s}) \quad (16)$$

Where  $N_f$  is the amplitude of the fast component and  $N_s$  the amplitude of the slow component. Accordingly  $\tau_f$  the life time of the fast component ( $\tau_f \approx 650 - 770\text{ns}$ ) and  $\tau_s$  the lifetime of the slow component ( $\tau_s \approx 3.2 - 3.5\mu\text{s}$ ). It has been found that the proportion between the two components is energy and particle dependent. This property can be used to identify isotopes by extracting the  $N_f$  and  $N_s$  values from pulse shape analysis (PSA) on the according light emission response<sup>16</sup>, as shown in figure 10.

### From scintillator light to electrical signal

The scintillator light produced at different points inside the crystal has first to be transported to the back-end of the crystal. The optimum design has been determined to be frustum-shaped crystals, wrapped into enhanced specular reflector (ESR) foil which provides excellent reflectivity.<sup>17</sup>. Finally, a large-area avalanche photodiode (LAAPD), specifically the Hamamatsu S12102 model [54], is attached at the rear end of each crystal to enable the detection of scintillation light. Avalanche photodiodes (APDs) operate on the same fundamental principle as conventional photodiodes, converting scintillation light into electrical signals. Both offer the advantage of being insensitive to magnetic fields, making them particularly suitable for applications in environments with strong magnetic interference. As a result of an additional highly doted p-layer a

---

(scintillation) photons/MeV.

<sup>16</sup>The method has been implemented in the CALIFA Firmware as *QuickParticleIdentification – QPID*. For more information see [51] and [52]

<sup>17</sup>Detailed information about the crystal wrapping and LAAPD gluing can be found in this work:[53]

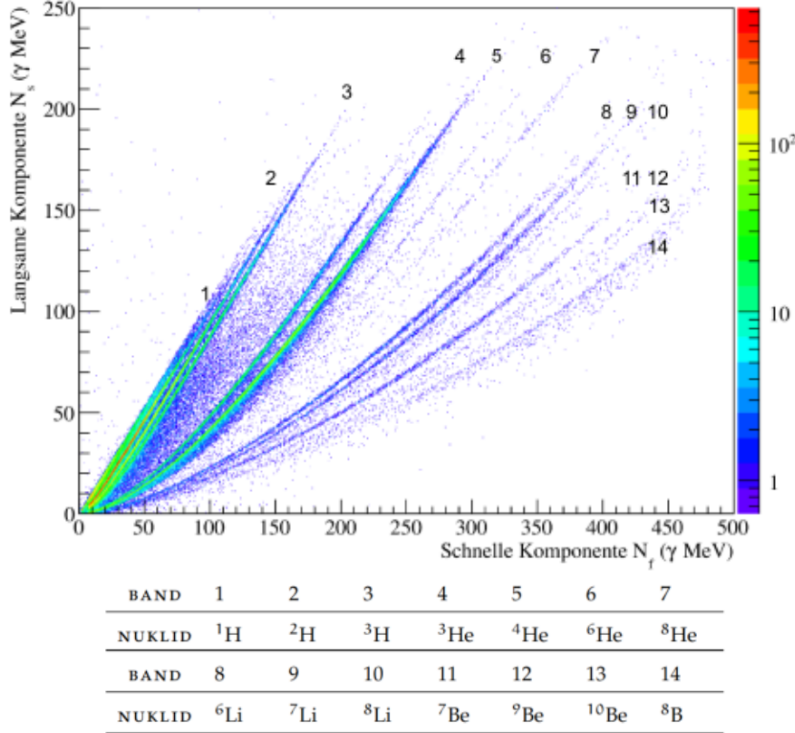


Figure 10: Quick Particle Identification(QPID) via fast and slow component  $N_f/N_f$ . Each correlation band corresponds to a nuclide, from Ref.[52].

region with very high field is formed which accounts for amplification factors up to  $\approx 100$ .

For the next amplification step the electric signal is forwarded via thin coaxial cables to the front-end of the preamplifiers from Mesytec[55] which can serve up to 32 input channels. For CALIFA two general types of peramplifiers are in use:

1. Dual Range (DR) Preamplifiers: They are used in the iPhos and CEPA region where both high energetic protons as well as gammas are expected. They cover two output signals in parallel: a *gamma* signal high amplification and a *proton* signal with 11x lower amplification. Following from this they have 64 channel differential signal output.
2. Single Range (SR) Preamplifiers: In the Barrel region, where only one amplification range is implemented. Depending on the experimental demands these preamplifiers can be switched to *gamma* or *proton range*. These peamplifiers have a 32 channel differential signal output.

The fall time for the preamplifiers has been chosen to  $\tau_{RC} \approx 35 \mu\text{s}$ . This is a trade-off between the ballistic deficit on one side (reduction of the signal amplitude due to low  $\tau_{RC}$ , see also [51], chapter 3.4.5) and rate capability (restricted by large  $\tau_{RC}$  value) on

the other side.

The differential signal output of the preamplifiers is then transmitted over shielded and twisted line pairs to the input of the FEBEX Addon Boards (FAB) for further processing.

### Signal Processing and readout system

The central hardware module for the signal processing in CALIFA is the FEBEX 3B Module (Front End Board with optical link EXtension<sup>18</sup>). Attached on it is a so-called AddOn board developed by TUM. The signal from the preamplifier gets here first filtered by a low pass two pole bessel filter (with cutoff frequency  $f_{3dB} = 16MHz$ ). Furthermore, since the input of the FEBEX ADCs cover a range of  $\pm 0.9$  V while the signal output from the preamplifier only has one polarity, an offset to the signal is applied to use the full range of the 14 bit flash ADCs. The signal from the ADCs is read out continuously to ring buffers implemented in a FPGA TODO "dip" on the FEBEX card and split up into two branches:

1. Fast/trigger branch: After being fed to a digital trapezoidal filter the signal is examined by three leading edge discriminators with configurable thresholds. Depending on the experimental requirements a coincident matrix between one or more discriminators and optionally external triggers validates the signal as event ready for data recording.
2. Slow branch: Validated signals then undergo a digital analysis. A pulse shape analysis is performed via various steps - signal decimation, moving average unit -technique, baseline subtraction and moving window deconvolution (MWD) - to recall the major steps<sup>19</sup>. From the resulting pulse shape pulse height measurement the energy deposited in the scintillator is determined. In addition the algorithm for the quick particle identification (QPID) is applied on the incoming signal which provides the fast( $N_f$ ) and slow( $N_s$ ) component of the signal for isotope identification and differentiation of stopped and punch-through particles. The CALIFA Firmware also allows to make time over threshold (TOT) measurements which is convenient for energy reconstruction when the incoming signals exceed the ADC range (which might happen when the preamplifier is set to *gamma range*)<sup>20</sup>.

---

<sup>18</sup>See the FEBEX3b datasheet provided by GSI: <https://www.gsi.de/fileadmin/EE/Module/FEBEX/fbex3b.pdf> (accessed April 30, 2025).

<sup>19</sup>A really detailed description of the pulse shape analysis in CALIFA can be found in Philipp Klenze's[56] and Max Winkel's thesis[52].

<sup>20</sup>The TOT energy-reconstruction method has the drawback of being really sensitive to pile-up events overestimating the energy deposition. Hence more suitable for regions with low event rates, such as Barrel region.

## Trigger Distribution and Validation

The central hub for internal and external trigger forwarding is formed by the Exploder modules<sup>21</sup>. The FEBEX crates are connected to the Exploder via an eight-fold flat cable known as the trigger bus. This setup allows efficient distribution and handling of trigger signals within the system.

The Exploder module provides multiple input and output lines and includes an internal, switchable bypass matrix. This enables to operate the CALIFA calorimeter in different modes:

- **Free-running mode:**internal validation based solely on signal thresholds from the preamplifiers. This configuration is suitable for calibration tasks (e.g., with  $\gamma$ -ray sources like  $^{22}\text{Na}$  or  $^{60}\text{Co}$ ) or low event-rate experiments.
- **Externally validated mode:**additional validation signals, such as clean CFD outputs from sub-detectors (e.g., START), are used for triggering/event selection. This configuration is preferred for high-rate or coincidence experiments involving multiple detector subsystems.

## Readout Electronics and Data Transfer<sup>22</sup>

Trigger bus control between the data acquisition PCs and the FEBEX cards is managed by the TRIXOR card<sup>23</sup>, which is directly connected to the DAQ PCs. It interfaces with both the Exploder modules and the KNIPEX (PCIe Optical Link Interface<sup>24</sup>) card. Connections are established via:

- ECL lines (TRIXOR  $\leftrightarrow$  Exploders)
- 26-fold flat cable (TRIXOR  $\leftrightarrow$  KNIPEX)

The KNIPEX card handles high-speed data transfer between the FEBEX electronics and the acquisition computers. It connects to the FEBEX crates via optical fiber and buffers data locally in a 576 MB Reduced Latency Dynamic Random Access Memory (RLDRAM, see Ref. [57]). The buffered data is then transferred to the PCâŽs RAM via Direct Memory Access (DMA) with speeds up to 560 MB/s.

Each FEBEX channel is equipped with two memory banks and can store up to 254

---

<sup>21</sup>See the EXPLODER2a datasheet provided by GSI: [https://www.gsi.de/fileadmin/EE/Module/EXPLODER/exploder2a\\_v5.pdf](https://www.gsi.de/fileadmin/EE/Module/EXPLODER/exploder2a_v5.pdf)(accessed April 30, 2025).

<sup>22</sup>A more detailed explanation about the readout system and the critical FEBEX timing topic can be found in Philipp Klenze's thesis [56].

<sup>23</sup>See the TRIXOR datasheet provided by GSI: <https://www.gsi.de/fileadmin/EE/Module/TRIXOR/trixor.pdf>(accessed April 30, 2025).

<sup>24</sup>See the KNIPEX datasheet provided by GSI: [https://www.gsi.de/fileadmin/EE/Module/Dokumente/kinpex1\\_pcb15.pdf](https://www.gsi.de/fileadmin/EE/Module/Dokumente/kinpex1_pcb15.pdf) (accessed April 30, 2025).

events locally. To prevent dead time during readout, a memory bank switch is triggered automatically when one bank reaches its configured event limit. This design ensures continuous, dead-time-free event recording at the channel level. Once a FEBEX channel reaches its threshold, the entire crate is read out synchronously.

#### Data Acquisition System: MBS

The Multi Branch System (MBS) [58], developed at GSI Helmholtz Center for Heavy Ion Research, is employed on the data acquisition PCs. MBS is a modular software framework that controls detector readout, manages data storage, and provides networking capabilities for distributed acquisition systems.

Key features of MBS include:

- Integration of multiple detectors into a single, synchronized data stream
- Trigger signal and dead time exchange via a dedicated trigger bus
- Time-sorted event building through the *MBS event builder*, which brings together data across detector subsystems into coherent events

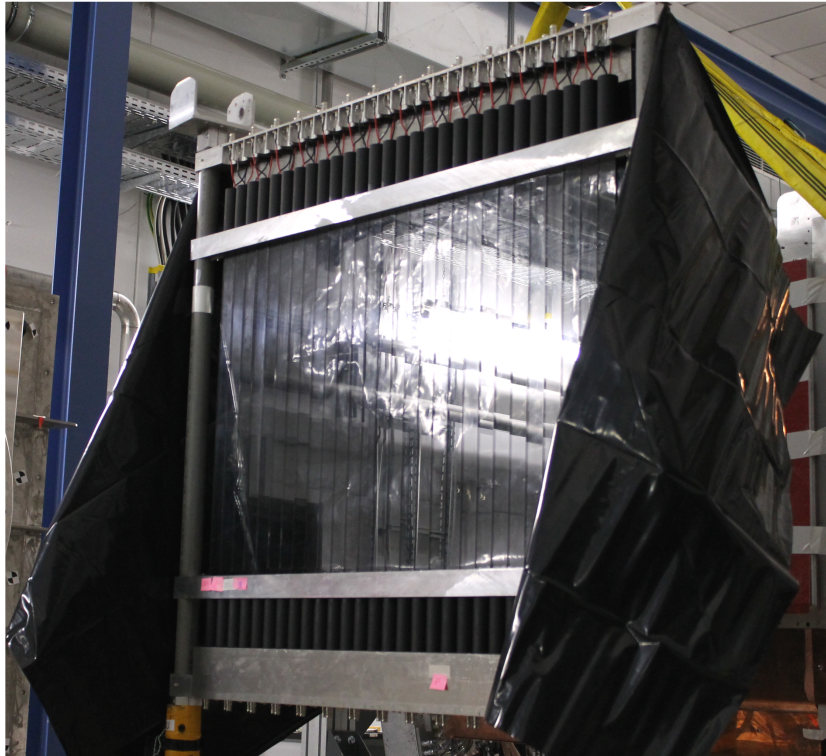
This system ensures robust, synchronized acquisition for complex multi-detector experiments.

#### 3.3.6 Sofia Time of Flight Wall

The Sofia Time of Flight Wall (or "Stop detector") is positioned at the very end of the heavy-ion flight-path downstream of the GLAD magnet, behind the MWPC 3 (see subsection 3.3.1), at approximately 6.6 m distance from the target position. It consists of a plane of 28 vertically aligned scintillator bars, each of dimension 32x600x5 mm. The scintillator plastics are numbered from 0 to 27 from left to right (when looking in beam direction). The time of flight of the ions between Start and ToFW can be measured by subtracting the time measurement of the Start detector from the ToFW. In optimal operating conditions, the combined time resolution of the Start and ToFW detectors can reach  $\sigma_{tot} < 40\text{ps}$ , enabling precise time-of-flight measurements, for an average time of flight of 30 ns[40]. For the technical specifications of the Sofia ToFW, see figure 11 and reference [59].

#### 3.3.7 NeuLAND Detector

For the detection of neutrons emitted from the forward going fragments the **New Large-Area Neutron Detector (NeuLAND)** is installed at zero degrees after GLAD. In its final design it will consist of 30 double planes with each 100 plastic scintillators of size 5x5x250 cm<sup>3</sup> providing an active detector surface of 2.5x2.5 m<sup>2</sup> and thickness of



---

Plastic	EJ-232, no quencher
Plastic dimensions	5x32x600 mm <sup>3</sup>
Detector dimension	5x900x600 mm <sup>3</sup> (28 plastics)
Photo-multiplier tubes	Hamamatsu 6533 and 10580
Total number of PMTs	56 (two per plastic - top and bottom)

---

Figure 11: Sofia ToFW in Cave C, from [40], and technical specifications.

3m. Its high detection efficiency, a time resolution of  $\sigma_t \leq 150\text{ps}$  and high multi-neutron efficiency are crucial detector features for complete kinematics experiments at R<sup>3</sup>B. A comprehensive analysis of the detector's resolution and efficiency is provided in Refs. [60, 61].

For the S444 commissioning experiment in 2020 13 double-planes of the NeuLAND detector have been used.

## 4 Analysis -

### Total Interaction Cross Section of $^{12}\text{C} + ^{12}\text{C}$

This chapter will go through the analysis step by step from the unpacking stage to the final results of the interaction cross sections. It will start by a short overview of the transmission method used for the cross section measurements. The next step is the selection of clean incoming  $^{12}\text{C}$  isotopes. Following the identification of the carbon isotopes after the target - for the measurement of the charge changing cross section - and as final step the interaction cross section measurement.

All relevant detector related geometrical and efficiency corrections will be addressed and their influence to the final result and its uncertainty will be discussed.

#### 4.1 Cross Section Measurement via Transmission Method

In its most generic form cross sections give a measure of the probability that a specific reaction will take place when two particles collide [62]. It is expressed in units of area, with one barn defined as  $1 \text{ b} = 10^{-24} \text{ cm}^2$ . Cross sections measured in scattering experiments, along with the corresponding energy and angular distributions of the reaction products, provide valuable insight into the underlying interaction dynamics between the projectile and target. Such measurements enable the extraction of fundamental quantities, including coupling constants, form factors, and structure functions.

In deep inelastic scattering processes involving multiple final-state channels, cross section measurements serve as a powerful tool to probe the parton distribution functions (PDFs), which describe the momentum distributions of quarks and gluons within nucleons. Furthermore, deviations from Standard Model predictions in the shape or magnitude of measured cross sections may indicate the presence of phenomena beyond the Standard Model, such as Supersymmetry or potential dark matter candidates.

The total cross section  $\sigma_{tot}$  can be derived by looking at the relation between the number of incoming particles ( $N_1$ ) and unreacted particles after the target ( $N_2$ ). For an experiment with fixed target with thickness  $z$  and volumetric number density  $n$  the number of reacted particles in the infinitesimal thin target layer  $dz$  can be expressed as:

$$\frac{dN_2}{dz} = -n\sigma_{tot}N_2 \quad (17)$$

Solving this differential equation for  $N_2$  (with the condition  $N_2 = N_1$  for  $z = 0$ ) discloses an exponential relation:

$$N_2 = N_1 e^{-n\sigma z} = N_1 e^{-N_t \sigma} \quad (18)$$

Where  $n \cdot z$  can be summarized as  $N_t$ , the total number of scattering centers per unit area. The relation  $(N_2/N_1)$ , number of unreacted particles after the target versus number of incoming particles, is often called survival probability  $P_{surv}$ . For an idealistic experimental setup with full detector efficiency and no interactions in the setup material the cross section could simply be deduced from equation 18. To account for reactions of the projectile that occur within the setup material and first order detector specific distortions of output signals the survival probability  $(N_2/N_1)$  has to be divided by the survival probability for an empty target run  $P_{surv}^E = (N_2^E/N_1^E)$ , where  $N_1^E$  is the number of incoming particles and  $N_2^E$  the number of unreacted particles after the target for an empty run respectively. Thereby the setup specific efficiency( $\epsilon_{setup}$ ) and transmission factor( $t_{setup}$ ) are canceled out to obtain the underlying number of unreacted particles after the target  $\tilde{N}_2$ :

$$N_2 = \tilde{N}_2 \cdot t_{setup} \cdot \epsilon_{setup}$$

$$N_2^E = \tilde{N}_2^E \cdot \epsilon_{setup} \text{ with } \frac{\tilde{N}_2^E}{N_1^E} \text{ the setup specific transmission factor } t_{setup}$$

The final formula for the cross section for a so called transmission measurement is:

$$\sigma = -\frac{1}{N_t} \ln\left(\frac{N_1^E}{N_2^E} \cdot \frac{N_2}{N_1}\right) = -\frac{1}{N_t} \ln\left(\frac{N_1^E}{\tilde{N}_2^E \cdot \epsilon_{setup}} \cdot \frac{\tilde{N}_2 \cdot t_{setup} \cdot \epsilon_{setup}}{N_1}\right)$$

$$\text{With } \frac{\tilde{N}_2^E}{N_1^E} = t_{setup} \quad (19)$$

$$\sigma = -\frac{1}{N_t} \ln\left(\frac{1}{t_{setup}} \cdot \frac{\tilde{N}_2 \cdot t_{setup}}{N_1}\right) = -\frac{1}{N_t} \ln\left(\frac{\tilde{N}_2}{N_1}\right)$$

It should be emphasized that this represents a first-order approximation, as in Equation 19 the setup-specific detection efficiency  $\epsilon_{setup}$  and transmission factor  $t_{setup}$  are assumed to be identical for both the empty and target runs. This assumption enables the cancellation of these factors in the ratio, thereby simplifying the analysis.

From the Equation 19 it is evident that for cross section measurements with the transmission method three types of observables have to be measured:

## ■ Number of scattering centers $N_t$

The number of scattering centers per unit area of the target is a target specific number. It depends from the target thickness and its density. The values herefore are taken from [63]<sup>25</sup>:

(a) Thin target:

$$\text{target thickness } d = 0.5451 \text{ cm; } N_t = 5.0588795 \cdot 10^{22}; \frac{\Delta N_t}{N_t} = 0.0648\%$$

---

<sup>25</sup>For the purpose of this work the target thicknesses were remeasured at GSI with a chromatic sensor giving 2D depth profiles of each target.

(b) Medium target:

target thickness  $d = 1.0793 \text{ cm}$ ;  $N_t = 1.0016600 \cdot 10^{23}$ ;  $\frac{\Delta N_t}{N_t} = 0.2620\%$

(c) Thick target:

target thickness  $d = 2.1928 \text{ cm}$ ;  $N_t = 2.0350598 \cdot 10^{23}$ ;  $\frac{\Delta N_t}{N_t} = 0.0322\%$

where  $N_t$  was calculated by:

$$N_t = \frac{\rho \cdot d \cdot N_A}{M} \quad (20)$$

with  $\rho$  the target density<sup>26</sup>,  $N_A$  the Avogadro constant ( $6.02214076 \cdot 10^{23} \text{ mol}^{-1}$ ) and  $M$  the molar mass of the target (for carbon  $M = 12.011 \text{ g} \cdot \text{mol}^{-1}$ ).

### ■ Number of incoming projectiles (<sup>12</sup>C) $N_1$

For the measurement only events with well identified incoming <sup>12</sup>C projectiles are chosen. Herefore strict cuts on the detectors upstream the target area are set. This strict event selection makes sure that we only consider events with single <sup>12</sup>C WITHIN TIME WINDOW:TODO. This will be discussed in more detail in section 4.2.

### ■ Number of unreacted projectiles (<sup>12</sup>C) $N_2$ after the target

Detectors downstream the target area are used to count the number of unreacted projectiles <sup>12</sup>C. To reduce detector specific influences which could distort the result it is advisable to use only as few as requirable detectors for the clear identification of unreacted projectiles. Moreover detector specific efficiencies are canceled out by including both empty and target runs (only in 1st order, as there may be a position dependence) in the cross section calculation(see equation19). For all downstream detectors used in this analysis it is critical to minimize any selection cuts and systematically check their effects on  $N_2$ .

## 4.2 Event Selection

For event selection, all three upstream detectors are utilized: the MWPC0, the R<sup>3</sup>B MUSIC Ionization Chamber, and the start detector. This selection of correlated signals in these detectors already ensure that individual dead times of the different DAQ systems and the central trigger system are excluded for the dataset and do not have to be considered in the following analysis. To ensure a clean incoming event selection, the following prerequisites must be met:

### 1. <sup>12</sup>C identification of incoming projectile by upstream detectors:

In the S444 experiment the incoming beam was directly delivered by the SIS18

---

<sup>26</sup> $\rho = 1.851 \text{ g/cm}^3$ , from [63]

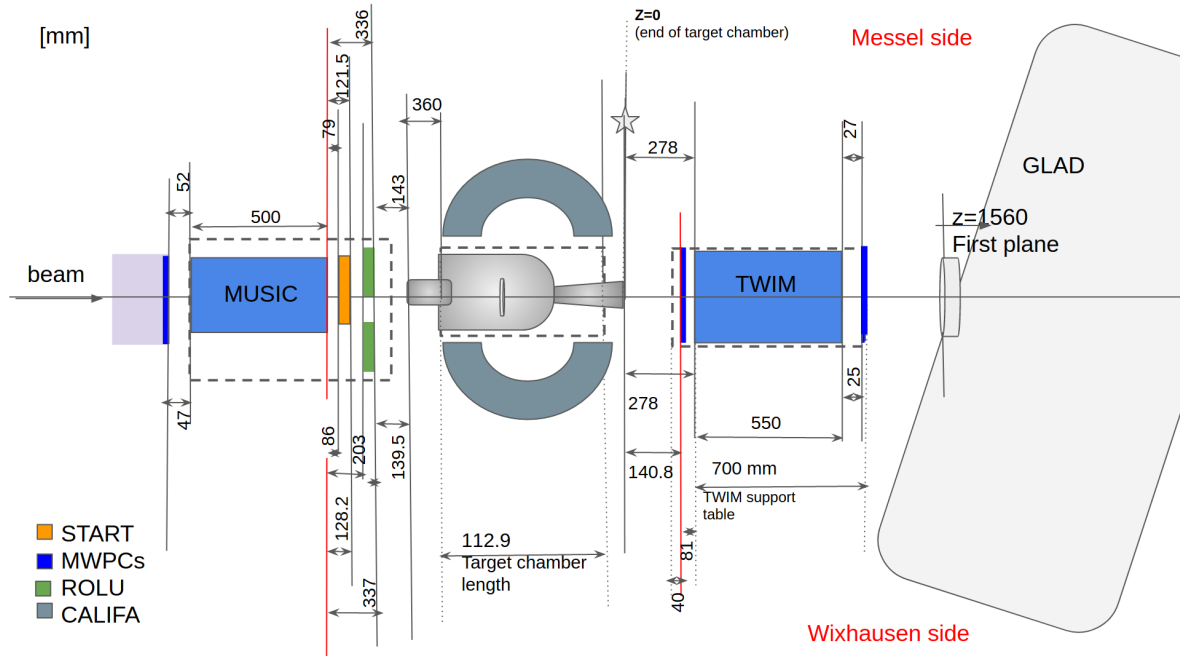


Figure 12: Schematic layout of the R<sup>3</sup>B experimental setup for the S444 experiment. The beam comes from the left, passing through MWPC0, R3B MUSIC (ionization chamber), START detector (orange), and ROLU (green) before interacting in the target chamber. The setup is spatially referenced with  $z=0$  at the end of the target chamber. Measurement directions "Messel side" and "Wixhausen side" are also indicated for (left-right) orientation. Dimensions are given in millimeters.

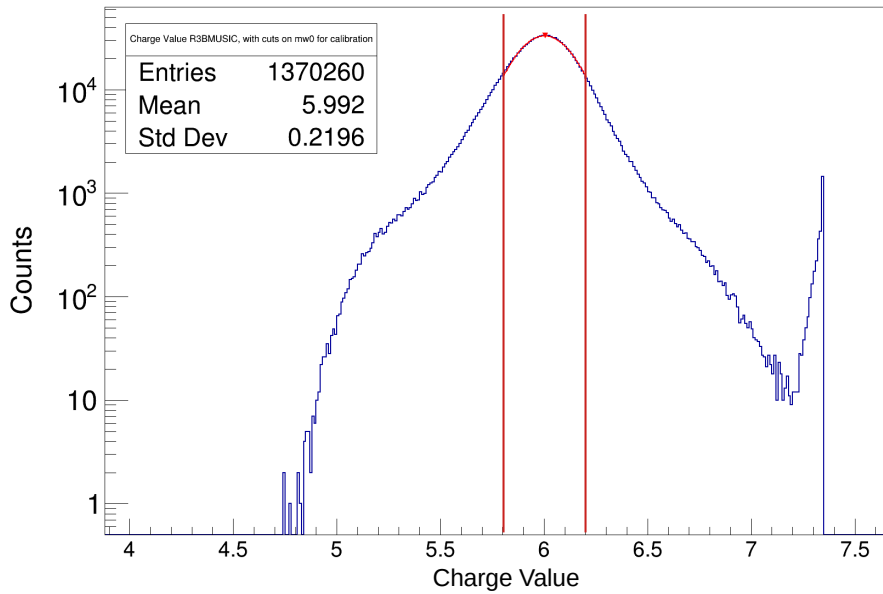


Figure 13: Charge distribution in R<sup>3</sup>B MUSIC with predefined calibration parameters with already applied positional cuts on MWPC0 - positioned upstream to the ionization chamber and required coincident signal in the start detector. The rise beyond Z  $\geq$  7.2 originates from pile-up events. The sharp cut on the right at Z  $\gtrsim$  7.35 is due to the limit of the electronics dynamic range. The fall off at Z  $\lesssim$  4.8 is due to applied threshold settings on the detector side.

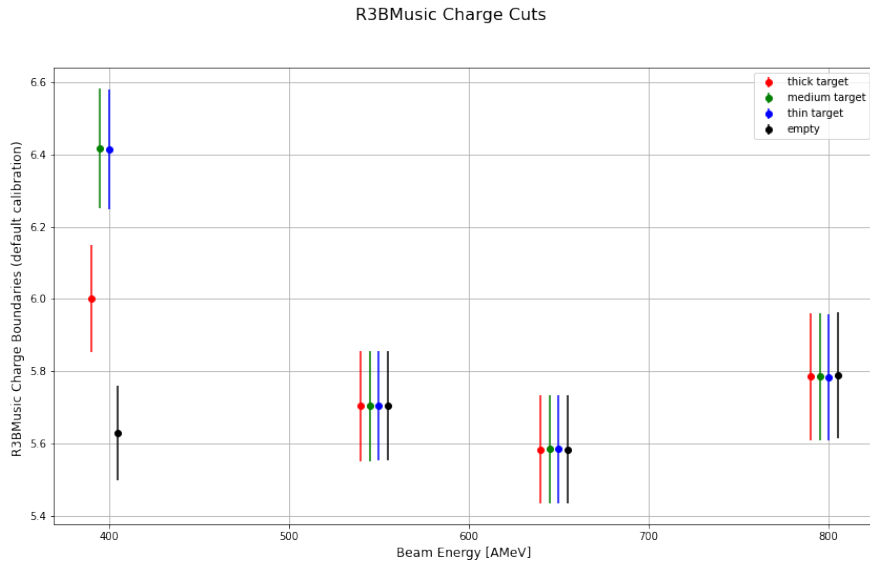


Figure 14: Strict  $\pm 1\sigma$  charge cuts with  $\text{R}^3\text{B}$  MUSIC for incoming particle selection. Fixed predefined calibration parameters were used which do not compensate different gain settings between runs. This is in particular the case for the 400 AMeV beam energy runs.

ring accelerator, which is operated in ultra-high vacuum. Due to the low material budget in this beam line and its narrow p/q acceptance the level of contamination is very low.

For the charge identification of the incoming ion the  $\text{R}^3\text{B}$  MUSIC ionization chamber is used which is positioned directly after the MWPC0 at the beam entrance in Cave C, see figure 12. The  $\text{R}^3\text{B}$  MUSIC detector measures anode-wise the energy loss of the passing-through ion which in the first order is proportional to the square of its charge ( $\Delta E \sim Z^2$ ). Herfore the calibration parameters from the online analysis are used<sup>27</sup>. Figure 13 shows the measured charge distribution in  $\text{R}^3\text{B}$  MUSIC. To select  $Z = 6$  incoming ions the distribution is fitted with a Gaussian fit function. Only ions with an energy loss within the  $\pm 1\sigma$  range are accepted. Figure 14 summarizes the  $\pm 1\sigma$  cuts on the  $\text{R}^3\text{B}$  MUSIC charge for empty/target runs for all beam energies.

## 2. Pileup rejection and TPat selection:

The overall recording and merging of the data from various sub-detectors is one of the tasks of the Data AcQuisition (DAQ) system. Whether an event is recorded or not depends on the pre-established trigger logic. Various detectors can send out triggers to the main DAQ when certain conditions are given (e.g. CALIFA can be

<sup>27</sup>These are generic parameter values used to the detector performance during the experiment phase.

configured to send out a trigger when a hit is recorded in the calorimeter). The different triggers are processed by the trigger logic and summarized as a defined trigger pattern, so called TPat, which is stored in a 16-bit mask for each event. Table 4 gives an overview of the trigger logic and the trigger patterns set in the S444 experiment. For this analysis the "*Min. Bias*" trigger is required<sup>28</sup>.

Since the TPat selection itself does not necessary set any pileup constraints it

Bit Position	TPat Name	Description
0	Min Bias	Hit in Start detector and $\overline{\text{ROLU}}$
1	Reaction	"CalifaOR" -high energy hit in CALIFA
2	Neutron	Hit in NeuLAND
3	p+n	Hit in CALIFA and Neuland
8	Califa	high energy hit in califa - off-spill
9	NeuLAND	Hit in NeuLAND - off-spill

Table 4: List of TPats set for S444 experiment. As for the selected runs low beam rates ( $< 10\text{kHz}$ ) were expected no dead time issues should arise for the in-beam detectors, therefore no downscaling of the *Min. Bias* TPat was deployed.

is important to analyze the signals of the detectors upstream carefully to insure yourself that only events with one incoming  $^{12}\text{C}$  ion at a time get selected. Therefore events with incoming ions with charge  $Z = 6 \pm 1\sigma$  are chosen, as discussed in the previous point. With this restrictive cut pileup events can be efficiently rejected (see also Appendix A).

Moreover it is required that both left and right preamplifiers of the start detector have seen a coincident signal within a time-window of 1.391 ns, see Fig. 15. The width of the time window was chosen based on the maximum signal rise time of the detector as well as the maximal propagation delay of the scintillation light to the oppositely positioned preamplifiers. The overall searching window of the start detector was set to 2  $\mu\text{s}$ , see figure 15.

For the MWPC0 which is mounted right at the beam entrance of Cave C no hit multiplicity cuts were applied considering its operating mode, which is designed for charge sharing between the readout pads.

### 3. Projectile's focus on the target region:

To assure that the incoming  $^{12}\text{C}$  ion hits the target it is necessary to select only events where the projectile is focused to the target region. Therefore strict cuts

---

<sup>28</sup>This includes also "*Reaction*" and "*Neutron*" TPat since these patterns contain also "*Min. Bias*" TPat as necessary condition.

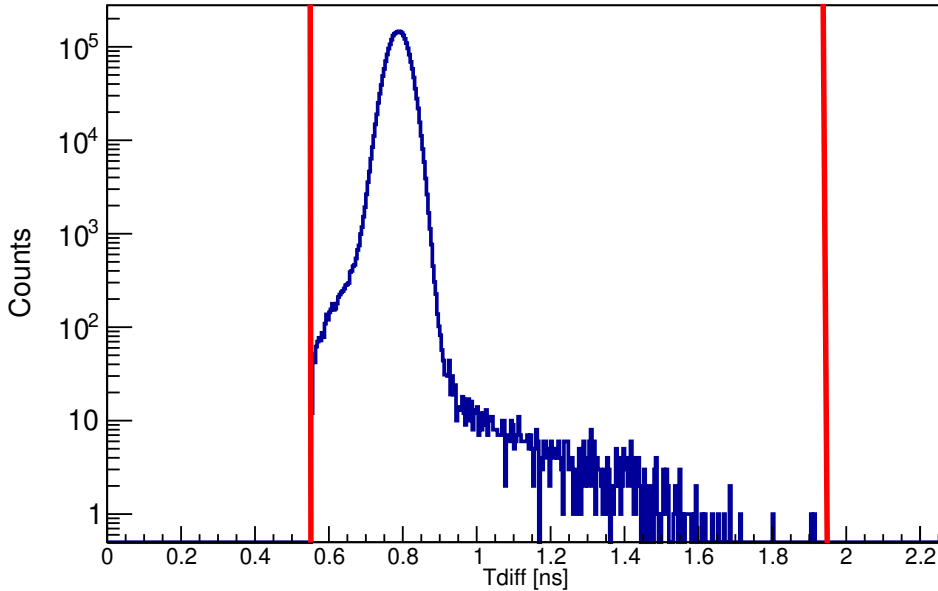


Figure 15:  $\Delta t_{right-left}$  between hits in the Start detector for events with exactly one hit on the left and right preamplifier and limiting the time difference in the range 0.555 ns to 1.946ns.

on the MWPC0 x and y position are applied. This was achieved by fitting the x and y distribution of the MWPC0 (without any restrictions on it) by a Gaussian function. The selection of "focused" incoming projectiles was then restricted to events with hits in MWPC0 within the  $\pm 1\sigma$  region in the x and y position around the beam spot center, see figure 16 and 17.

The MWPC0 x-position and the available projectile angle in the x-y plane from the R<sup>3</sup>B MUSIC is used to propagate the corresponding x-position on the target location to further check that the selected projectiles hit the target parallel to the z-position (= beam direction) and do only have a minimal incident angle, see figure 18.

### 4.3 Charge Changing Cross Section Measurement

The charge changing cross section refers to a measure of the probability that the incoming projectile will undergo a reaction inside the target that changes its charge. To measure the charge changing cross section it can be referred to formula 19 where in this case  $N_2$  is the number of survived carbon isotopes, i.e. projectiles which did not change their charge state. For this measurement only the data from the double ionization chamber TWIN MUSIC (see section 3.3.2) needs to be read out and analyzed.

While for the event selection before the target the cut conditions can be arbitrarily strict (it will only have an impact to the statistics and the derived statistical error),

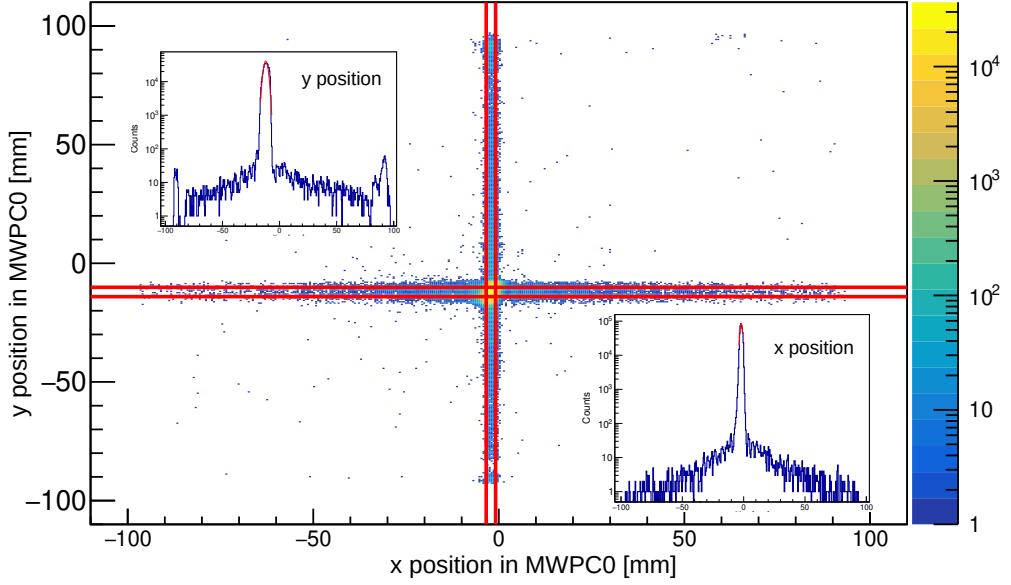


Figure 16: Reconstructed  $x$ - $y$  position of incoming ions on MWPC0 without applying a charge selection on the R3B MUSIC detector. The position reconstruction was performed without enforcing any multiplicity cut on the number of hits in MWPC0. However, a strict selection of  $\pm 1\sigma$  around the beam spot center was applied independently in  $x$  and  $y$ , as indicated by the red rectangular region. A detailed description of the MWPC0 hit selection procedure is provided in Appendix C.

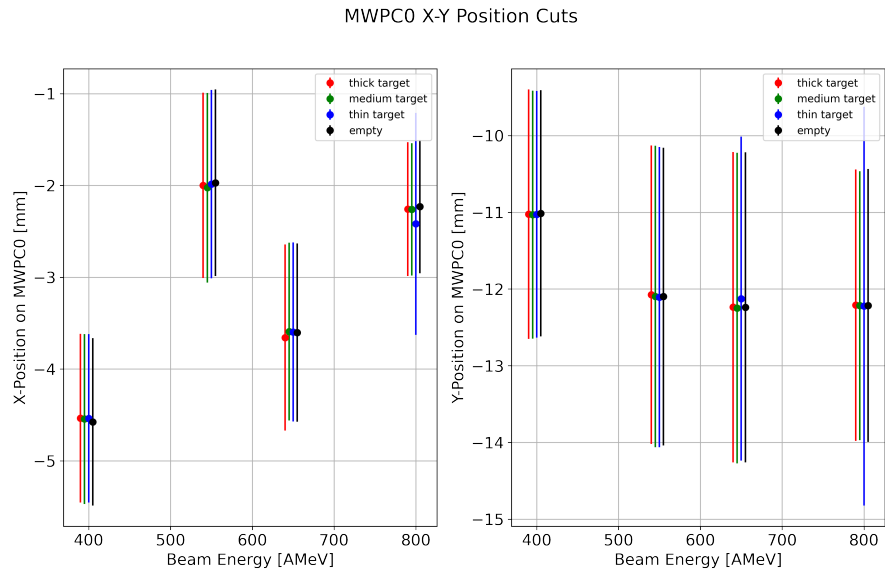


Figure 17: Overview of  $\pm 1\sigma$  cuts in  $x$  and  $y$  in MWPC0 for empty/target runs.

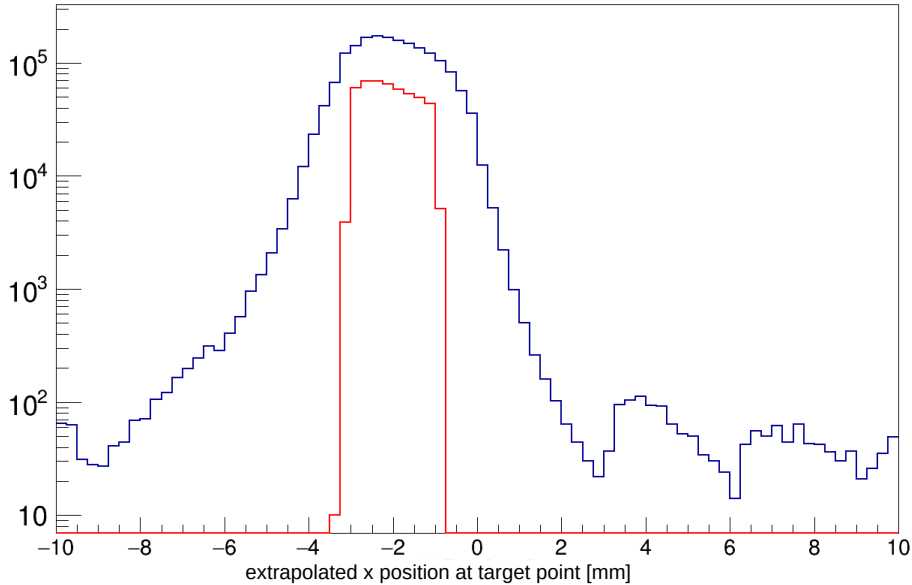


Figure 18: Propagated x-position on target location from measured x-value on MWPC0 and angle measurement from R<sup>3</sup>B MUSIC. The target area is 3 x 3 cm. In red the selected events with  $\pm 1\sigma$  cut in x and y position in MWPC0 and  $\pm 1\sigma$  charge cut on R3B MUSIC, in blue no cut on incoming events. Thin target run, 550 AMeV.

cuts on the downstream detectors need to be avoided if at all possible. Too selective cuts on the identification of  $N_2$  can alter the result of the measurement.

#### 4.3.1 TWIN MUSIC Calibration

For the analysis of data in TWIN MUSIC – different to the upstream detectors, where calibrated data with default calibration parameters is used – the so called *mapped* raw level data is processed. In the mapped level TWIN MUSIC provides following information:

- **SectionID:** The detector is a double ionization chamber and as such divided into four parts (in beam perspective): section 1 - right down; section 2 - right up; section 3 - left down; section 4 - left up. For the S444 experiment only section 1 was operated and accordingly geometrically centered on the beam spot.
- **AnodeID:** Each section has 16 anodes for energy-loss readout and one reference anode (anodeID = 17).
- **Time:** Each hit in each anode gets assigned to a time. The drift time (in ns) of the electrons from the ionization process of the gas by the in-flying projectile (or the fragments of it) to the anode is calculated by subtracting the individual anode time by the time of the reference channel. The reference anode receives its

clean signal from a constant fraction discriminator of the start detector.

- **Energy:** Each hit in each anode gets assigned to an energy. To reconstruct the charge of the passing charged particle anode-wise or detector-wise the parametrization formula:

$$Z = a + b \cdot \sqrt{(E)} + c \cdot E \quad (21)$$

is used with individual settings of the calibration parameters  $a$ ,  $b$  and  $c$ . For this analysis  $a$  and  $b$  are set to zero, so that the parametrization formula is reduced to  $Z = c \cdot E$ <sup>29</sup>.

The calibration of the TWIN MUSIC energy response was performed individually for each anode on a run-by-run basis. For the calibration step, only events in which all anodes – including the reference anode – registered exactly one hit were selected to ensure consistent signal conditions. The most prominent peak in the charge spectrum, corresponding to carbon fragments with charge  $Z = 6$ , was fitted using a Gaussian function. The calibration for each anode was then achieved by determining a scaling factor that aligns the mean of its Gaussian fit with the reference position at  $Z = 6$ ; see Fig. 19.

For the analysis of reaction fragments, the reconstructed charge  $\bar{Z}$  is finally determined from the calibrated energy signals according to:

$$\bar{Z} = \frac{1}{n} \sum_{i=1}^n c_i \cdot E_i, \quad (22)$$

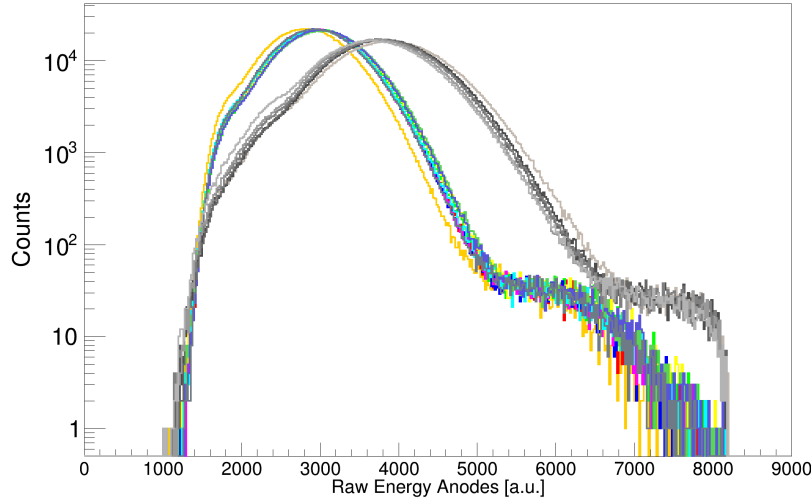
where  $E_i$  is the energy signal recorded by the  $i$ -th anode,  $c_i$  is its corresponding calibration factor, and  $n$  is the number of anodes with valid signals contributing to the event.

### 4.3.2 TWIN MUSIC Event Selection

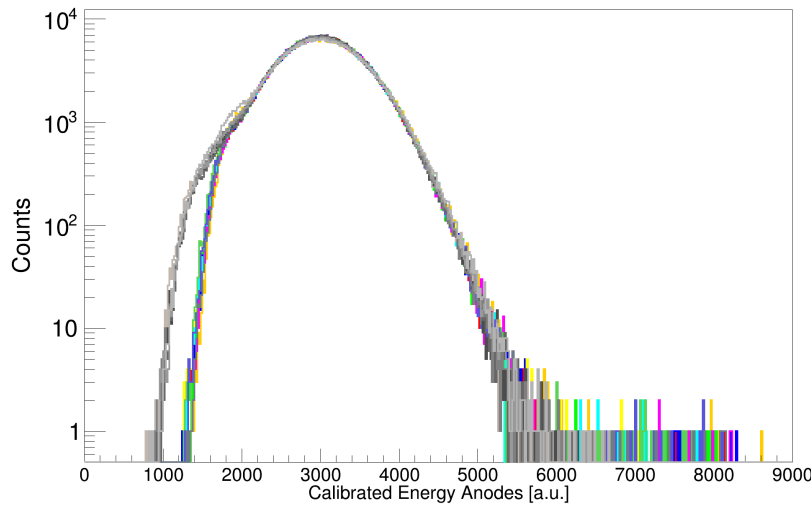
As previously stated cuts on the downstream detectors are avoided. However, events which have hits in one or several anodes in TWIN MUSIC but no signal in the reference anode are discarded as a whole neither contributing to  $N_1$  (incoming selected ions) nor to  $N_2$  (unreacted ions). If no reference time from start CFD signal is available it is not possible to measure the drift time in the individual anodes which makes it not possible to distinguish between signal and noise hits for multi-hit anode events in TWIN MUSIC.

---

<sup>29</sup>In this analysis, no  $\beta$ -correction is applied to the energy loss  $\Delta E$  measured in the TWIN MUSIC detector. Such a correction is only required in analyses involving heavy fragments, where the relative difference in charge between neighboring isotopes (e.g.,  $Z$  and  $Z \pm 1$ ) becomes small, and the velocity dependence of energy loss significantly affects charge resolution, e.g. fission experiments with heavy fragments and broad  $\beta$ -range.



(a) Uncalibrated raw energy-loss ( $\Delta E$ ) distributions for all 16 TWIN anodes recorded during the thick-target run at a beam energy of 550 AMeV. The eight upstream anodes are shown in color, while the eight downstream anodes are displayed in shades of gray. No charge selection based on the R3B MUSIC detector or position cut using MWPC0 was applied, which accounts for the extended high-energy tail caused by pileup events. The sharp cut-off at 8192 a.u. corresponds to the upper limit of the digitizer's dynamic range, while the steep drop around 1500 a.u. results from the applied electronic thresholds. The last six anodes exhibit a slightly different amplification factor.



(b) Calibrated energy-loss ( $\Delta E$ ) distributions for all 16 TWIN anodes after applying strict event selection criteria on R3B MUSIC and MWPC0 position distribution. A Gaussian fit was performed on the raw  $\Delta E$  spectra for each anode, and the resulting peaks were aligned by applying individual shifts, ensuring a consistent energy scale across all channels.

Figure 19: Fitting procedure in TWIN MUSIC.

The number of events affected by this cut is in the region of  $10/10^5$ . This is negligible to the number of incoming ions  $N_1$  and should not have any dependence whether the projectile reacted or not.

# incoming projectiles $N_1$	400 MeV/nucleon	550 MeV/nucleon	650 MeV/nucleon	800 MeV/nucleon
Empty	574279(*451*)	453729(*34*)	522451(*44*)	395451(*52*)
thin	569503(*422*)	476323(*33*)	538037(*43*)	481459(*36*)
medium	606578(*431*)	451137(*27*)	500688(*40*)	345654(*46*)
thick	655762(*497*)	436457(*30*)	530869(*29*)	479679(*61*)

(a) Number of clean selected incoming  $^{12}\text{C}$  ions. In brackets number of rejected events because of missing tref in TWIN MUSIC. TODO: change the bracket notation, looks like error number!!

# survived carbon isotopes $N_2$	400 MeV/nucleon	550 MeV/nucleon	650 MeV/nucleon	800 MeV/nucleon
Empty	563382(1.898%)	444618(2.008%)	511923(2.015%)	387513(2.007%)
thin	538245(5.489%)	449422(5.648%)	507557(5.665%)	454099(5.683%)
medium	552763(8.872%)	410376(9.035%)	455159(9.093%)	314119(9.123%)
thick	553935(15.528%)	368004(15.684%)	446115(15.965%)	402696(16.049%)

(b) Number of survived carbon isotopes after the target identified via 2D Gaussian fit with borders within  $3.5\sigma$  fit range. In brackets the percentage of projectiles with a charge state of  $Z < 6$  after the target. In brackets the percentage of projectiles outside the  $3.5\sigma$  fit range, relative to the total number  $N_1$  of incoming  $^{12}\text{C}$  ions.

Table 5: Numbers of incoming projectiles  $N_1$  and survived carbon isotopes  $N_2$  for all energy and target combinations after the event selection.

### 4.3.3 Carbon Identification

The identification of carbon isotopes in TWIN is done by reconstructing fragments with charge  $Z = 6$  from 2D plots where coincident mean reconstructed charge values for different anode combinations are plotted. Since the TWIN MUSIC is multi-hit capable various strategies were developed to deal with multi-hit events, i.e. when having anodes with multiple hits, decide which hit originates from the final state products from the reaction and which from background and noise. It is important to emphasize that these multi-hit events are not associated with pile-up phenomena, as such events are effectively identified due to the longer shaping time of the R3B MUSIC detector and

are already excluded by the stringent charge selection applied in the R3B MUSIC data preprocessing.

The default strategy is to use the time information for single hit selection in multi-hit anodes. It has to be remarked that for the S444 experiment the TWIN MUSIC was read out by two independent MDPP modules [64]. The signals from the first reference anode and the first eight upstream anodes were sent to module 1, the ones from the last eight downstream anodes and the second reference anode were forwarded to module 2. For the first eight upstream anodes the drift time is calculated by subtracting the hit time in each anode by the reference time from the first reference anode and for the last eight downstream anodes accordingly the second reference anode was used.

The time based selection algorithm for multi-hit anodes works as follows:

1. Get the mean drift time for the eight upstream anodes( $t_{mean\_up}$ ) and the eight downstream anodes( $t_{mean\_down}$ )<sup>30</sup>. Anodes with multiple hits do not contribute to this calculation.
2. If there are anodes with multiple hits compare the hit time with the according mean drift time ( $t_{mean\_up}$  for any of the eight upstream anodes,  $t_{mean\_down}$  for any of the eight downstream anodes). Calculate the absolute difference between mean drift time and each hit time:

$$\Delta t = |\bar{t} - t^i_{drift}|; i = \text{anodeID } (1-16) \text{ with } \bar{t} = \begin{cases} t_{mean\_up} & \text{for } i \leq 8 \\ t_{mean\_down} & \text{for } i \geq 9 \end{cases} \quad (23)$$

3. For each anodes with multiple hits select the hit with lowest drift time difference to the mean drift time.

After selecting the appropriate hit for both single- and multi-hit anodes, the mean reconstructed charge is calculated separately for the eight upstream anodes ( $\overline{Z_{up}}$ ) and the eight downstream anodes ( $\overline{Z_{down}}$ ). To identify the surviving carbon isotopes, a two-dimensional Gaussian fit is then applied to the  $\overline{Z_{up}}$  versus  $\overline{Z_{down}}$  distribution, centered on the peak at  $\overline{Z_{up}} \approx \overline{Z_{down}} \approx 6$  (see Fig. 20):

$$f(x) = Ae^{-\frac{1}{2}((\frac{x-\bar{x}}{\sigma_x})^2 + (\frac{y-\bar{y}}{\sigma_y})^2)} \quad (24)$$

where x is the mean re-scaled energy loss of the first upstream anodes and y the according eight downstream anodes. The number of survived carbon isotopes is given by the integral of events within the 2D Gaussian fit. Since the anodes were read out by

---

<sup>30</sup>For the case all eight downstream anodes have multiple hits, set  $t_{mean\_down} = t_{mean\_up}$  and vice versa

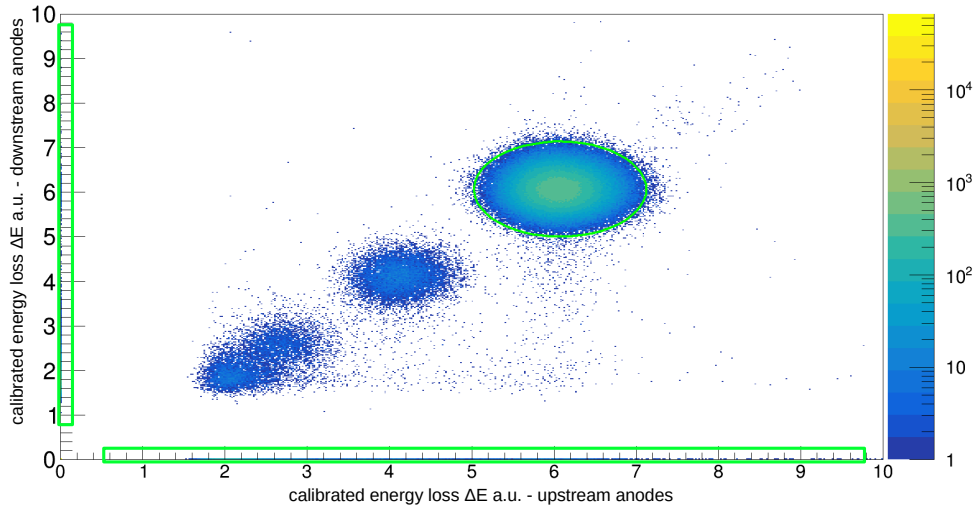


Figure 20: Two dimensional Gaussian fit with  $3.5 \sigma$  fit range on identified carbon isotopes in TWIN MUSIC. The horizontal and vertical side bars contain events where either the eight upstream anodes or downstream anodes have no hit entry. The cluster at  $\bar{Z} \approx 4.5$  corresponds to boron isotopes ( $Z=5$ ). The broad cluster observed for  $\bar{Z} \leq 3.5$  originates from events in which the  $^{12}\text{C}$  ion undergoes fragmentation into multiple light charged particles. In such cases, the total energy loss of the resulting particle combinations is measured in the TWIN MUSIC, which does not permit their individual separation.

two independent MDPP modules with slightly different thresholds also events along the histogram axes with no hit entry in either the upstream anodes or downstream anodes are analyzed. For those events a one dimensional Gaussian cut is applied using the parameters from equation 24 (see horizontal and vertical bars in figure 20).

A preliminary estimate of the charge changing cross section, neglecting the influence of the geometrical acceptance of the TWIN MUSIC detector, can be derived from the raw event numbers using Eq. 19:

$$\sigma = -\frac{1}{N_t} \ln \left( \frac{N_1^E}{N_2^E} \cdot \frac{N_2}{N_1} \right),$$

where the number of surviving carbon isotopes,  $N_2/N_2^E$ , for the target and corresponding empty-target runs is obtained via the two-dimensional Gaussian fit shown in Fig. 20. The preliminary results are presented in Fig. 21, where the fit range in the 2D distribution was fixed to  $3.5\sigma$ .

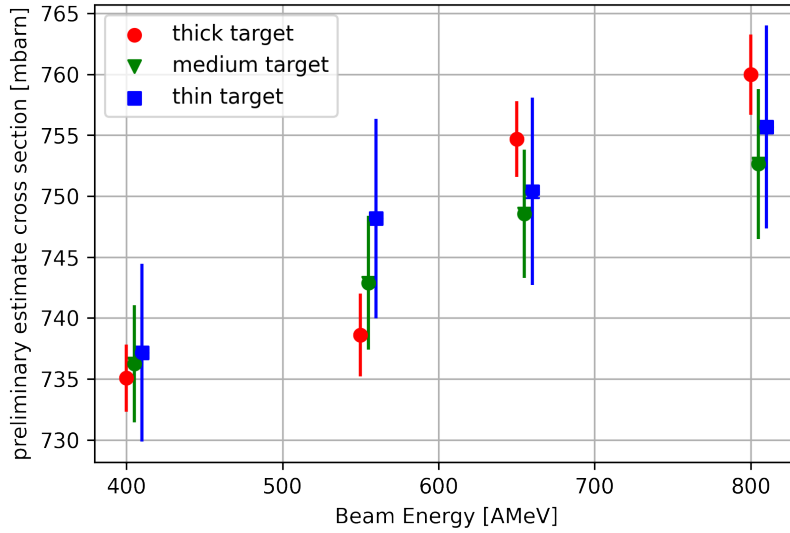


Figure 21: Preliminary estimate of charge-changing cross sections obtained by applying a two-dimensional Gaussian fit to the correlation plot of the reconstructed mean charge from the eight upstream anodes ( $\bar{Z}_{\text{up}}$ ) versus the eight downstream anodes ( $\bar{Z}_{\text{down}}$ ) and considering the borders as in figure 20. Only statistical errors are shown.

To get the optimal fit range on the two dimensional Gaussian fit on the reconstructed charges of the upstream anodes versus downstream anodes the charge changing cross section for all targets and all energies was systematically measured for  $\sigma$ -fit ranges between one and five  $\sigma$ , see figure 22. In the region around  $3.5\sigma$  the variation of the cross section is minimal.

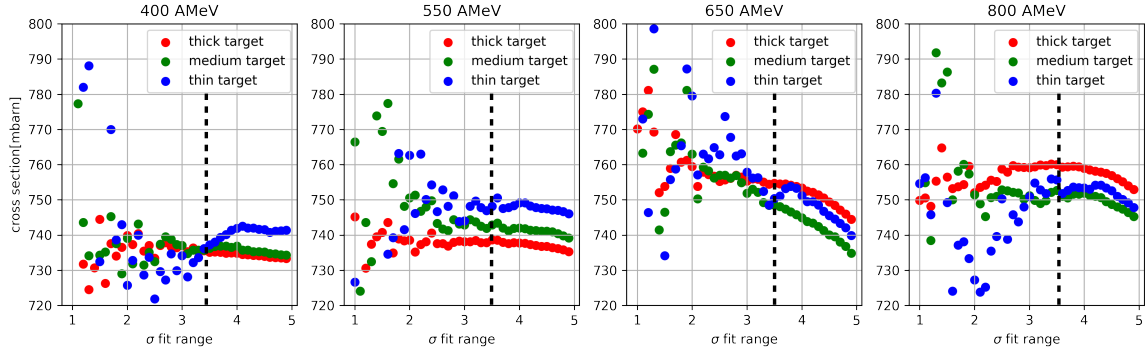


Figure 22: Preliminary estimate of the charge changing cross sections according to the  $\sigma$  fit range applied on the figure 20 (with borders) for the different target thicknesses and beam energies.

For the sake of completeness, Appendix D presents alternative methods for hit selection in multi-hit events in the TWIN MUSIC detector – such as selecting the hit with the highest energy deposition in multi-hit anodes – as well as different strategies for defining the charge selection cuts around  $Z = 6$ . Nevertheless, the approach presented in this section has proven to be the most stable and robust for the present analysis.

## 4.4 Geometric Corrections

During the S444 experiment only an active area of 11 x 11 cm was used, see section 3.3.2. Particles which undergo elastic or inelastic scattering or simply exit the target at larger angles due to the multiple scattering process, may therefore not be fully confined in the active volume of the TWIN MUSIC. To visualize the restricted geometric acceptance of the TWIN MUSIC the position in x and y (perpendicular plane to the beam direction) on the MWPC1 in front of the ionization chamber was plotted, for comparison without any conditions on the TWIN MUSIC and with the condition of having identified a carbon isotope (with the 2D Gauss-fit method as described in chapter 4.3.3), see figure 23. The large active surface area of 200 x 200 mm<sup>2</sup> of the MWPC1 affirms a larger acceptance<sup>31</sup> whereas the TWIN MUSIC behind it, with an active surface of 110 x 110 mm<sup>2</sup> (section 1), is – as mentioned – not sensitive to the scattered fragments with large deflection angle.

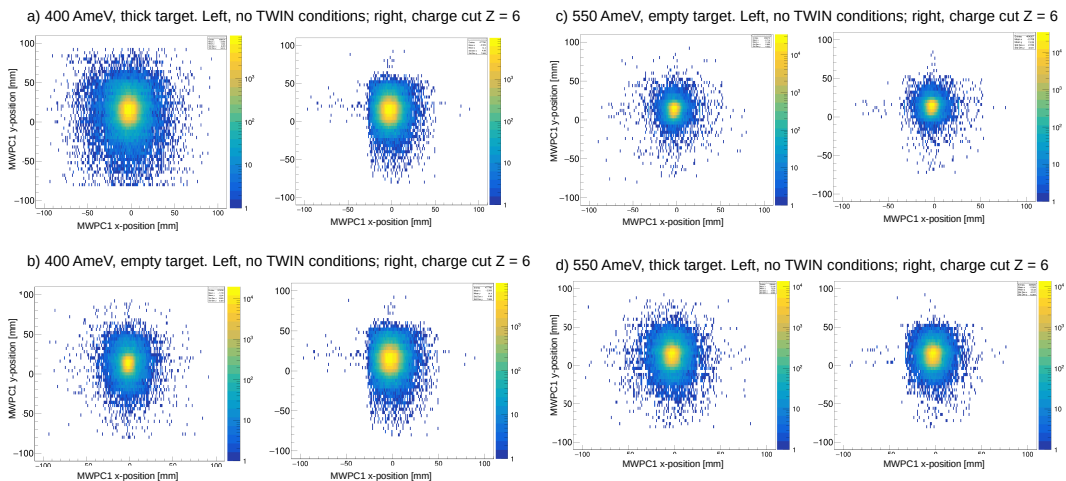


Figure 23: Distribution in x and y on MWPC1 for different energies with and without target.

The relative acceptance of the detection system is influenced by both the target thickness and the beam energy. Thicker targets lead to a broader angular distribution of the fragments due to increased multiple scattering and energy loss, thereby reducing the geometric acceptance. In contrast, higher beam energies result in smaller scattering

<sup>31</sup>This statement does not hold for light fragments as protons or deuterons. Their deflection angle exceeds the geometric acceptance of the MWPC1.

angles owing to relativistic boost effects, which in turn increase the acceptance. Consequently, the acceptance correction must be evaluated and applied individually for each specific beam-target configuration. It is important to note that acceptance effects cannot be corrected by referencing to empty target runs. All these acceptance effects can be observed in figure 23.

To compensate correctly for the geometric acceptance it has to be considered that for the charge changing cross section measurement only the carbon isotopes after the target are counted in the TWIN MUSIC. Therefore the correction should only be applied to the carbon isotopes ( $Z = 6$ ) on the x-y distribution on the MWPC1, see figure 23. The geometric efficiency correction is done graphically on the x-y distribution of the MWPC1 for carbon isotopes by following procedure:

### 1. Correction for the x-position distribution:

- (a) First fit x-distribution with double-gaussian function with five free parameters and common mean value  $\mu_x$

$$f(x) = A \cdot \exp\left(-\frac{(x - \mu_x)^2}{a^2}\right) + B \cdot \exp\left(-\frac{(x - \mu_x)^2}{b^2}\right) \quad (25)$$

- (b) Fit again within range  $\mu_x \pm \epsilon_x$ . The parameter  $\epsilon_x$  is fixed by educated guess, TODO. As  $\mu_x$  take the value from the fit in the previous step. A fit for the central region of the x-distribution is obtained,

$$f(x)_{central}(A_{central}, a_{central}, B_{central}, b_{central}, \mu_{central}).$$

- (c) The obtained fit function  $f(x)_{central}$  is then used to compare with the data distribution( $f(x)_{data}$ ) in the border regions  $[-100, \mu_{central} - \epsilon_x]$  and  $[\mu_{central} + \epsilon_x, 100]$ . Since only the left border region (low x-positions) is affected by the limited geometric acceptance, the right border region can be used for correction:

$$\Delta_{xcorr} = \int_{\mu_{central} + \epsilon_x}^{100} f(x)_{data} - f(x)_{central} - \int_{-100}^{\mu_{central} - \epsilon_x} f(x)_{data} - f(x)_{central} \quad (26)$$

### 2. Correction for the y-position distribution:

- (a) First fit y-distribution with double-gaussian function with five free parameters and common mean value  $\mu_y$

$$f(y)_{fit} = C \cdot \exp\left(-\frac{(y - \mu_y)^2}{c^2}\right) + D \cdot \exp\left(-\frac{(y - \mu_y)^2}{d^2}\right) \quad (27)$$

- (b) The obtained fit function  $f(y)$  is then used to compare the data distribution ( $f(y)_{data}$ ) in the border regions  $[-100, \mu_y - \epsilon_y]$  and  $[\mu_y + \epsilon_y, 100]$ . The parameter  $\epsilon_y$  is fixed by educated guess, TODO. As  $\mu_y$  take the value from the fit in the previous step. Same as for the x-correction both border regions are compared. The high border region (high y-positions) affected by the limited geometric acceptance while the low border region (low y-positions) has full geometric acceptance.

$$\Delta_{ycorr} = \int_{-100}^{\mu_{central}-\epsilon_y} f(y)_{data} - f(y)_{fit} - \int_{\mu_x+\epsilon_y}^{100} f(y)_{data} - f(y)_{fit} \quad (28)$$

3. To correct the number of survived carbon isotopes  $N_2 = N_{carbon}$  both corrections in x and y are applied<sup>32</sup>

$$N_2^{corr} = N_2 + \frac{\Delta_{xcorr} + \Delta_{ycorr}}{N_2} \quad (29)$$

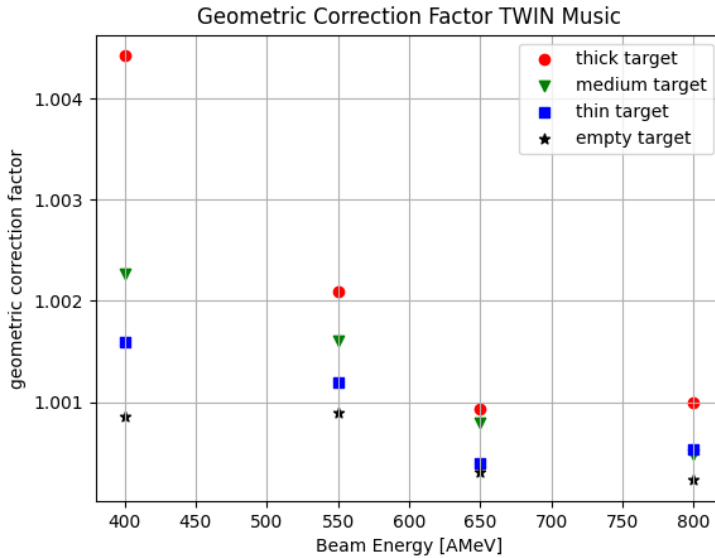


Figure 24: Geometric correction factors from limited geometric efficiency of TWIN MUSIC.

Figure 24 summarizes the geometric correction factors  $\epsilon_{geo\_corr}$  obtained from the graphical reconstruction of missed TWIN MUSIC events as described above. The correction factor is subsequently applied to the charge-changing cross-section, resulting in the final corrected charge-changing cross-section:

$$\sigma_{geo\_corr} = -\frac{1}{N_t} \ln\left(\frac{N_1^E}{N_2^E} \frac{N_2}{N_1} \cdot \epsilon_{geo\_corr}\right) = -\frac{1}{N_t} \left( \ln\left(\frac{N_1^E}{N_2^E} \frac{N_2}{N_1}\right) + \ln(\epsilon_{geo\_corr}) \right) \quad (30)$$

---

<sup>32</sup>Under the assumption that x and y are uncorrelated where the x-y distribution on the MWPC1 is given by  $f(x, y) = f(x) \cdot f(y)$ .

Figure 25 shows the measured charge changing cross section once without considering

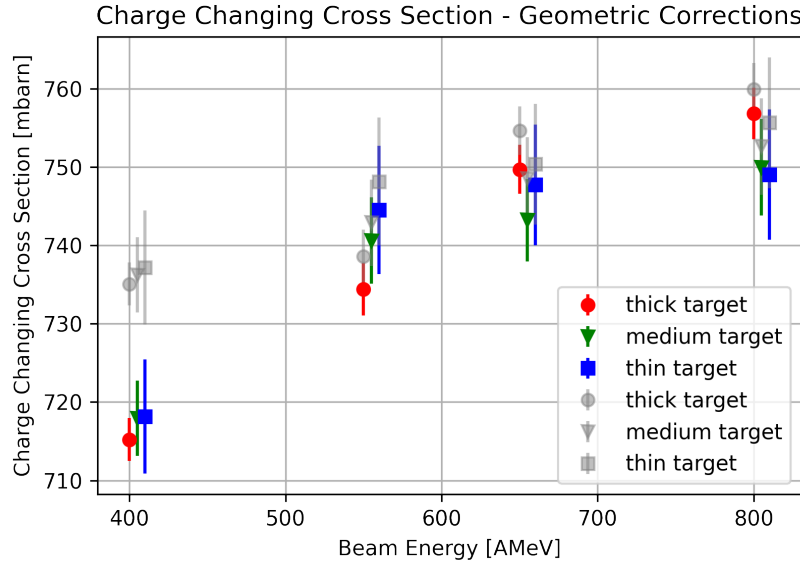


Figure 25: Charge changing cross section with applied geometry corrections. In gray: charge changing cross section measurements before applying corrections, as in figure 21.

the limited geometric acceptance of the TWIN MUSIC and once applying the geometric correction factors as presented in equation 30. As expected significantly affected by the geometric correction are runs with 400 and 550 AMeV beam energy whereas at beam energies of 650 and 800 AMeV the effect is exceptionally small since at high beam energies the fragments after the target perceive a strong boost effect in beam direction which constrains the distribution in the x-y-plane.

## 4.5 Isotope Correction - Total Interaction Cross Section

The general formulation for the calculation of cross sections in equation 19 can be used to determine the cross section for specific channels depending on the definition of  $N_2$ . In the previous subsection 4.3 where the charge changing cross section was measured,  $N_2$  had to be sensitive to the charge of the outgoing fragment. Therefore  $N_2$  was defined as the number of survived carbon isotopes, i.e.  $N_2 = N_2^{Z=6}$ . For the measurement of the total interaction cross section  $N_2$  has to be sensitive to both proton and neutron number of the fragments.  $N_2$  is herefore restricted to the number of survived  $^{12}\text{C}$  isotopes, i.e.  $N_2 = N_2^{^{12}\text{C}}$ . Since  $N_2^{^{12}\text{C}}$  is a subset of  $N_2^{Z=6}$ ,  $N_2^{^{12}\text{C}}$  can be determined by identifying and disentangling the number of survived  $^{12}\text{C}$  isotopes from the set of events with carbon isotopes  $N_2^{Z=6}$ . For that reason the positional correlations on the x-coordinate of MWPC2 (upstream to GLAD) and the MWPC3 (downstream to GLAD) are exploited.

The GLAD magnet, which acts as a mass spectrometer, deflects the passing through fragment. Depending on its proton to neutron ratio the fragment is deflected more or less, described by the formula for magnetic rigidity:

$$B \cdot \rho = \frac{\gamma \cdot m \cdot v}{q} \quad (31)$$

where:

- $B$  is the strength of the magnetic field,
- $\rho$  is the radius of curvature of the particle's trajectory,
- $\gamma$  is the Lorentz factor,
- $v$  is the velocity of the particle,
- $m$  is its rest mass,
- $q$  is its charge.

Figure 60 shows the x distribution on MWPC2 versus MWPC3 for the thick target run at a beam energy of 400 AMeV. The main diagonal line corresponds to the  $^{12}\text{C}$  isotopes. From all isotopes they have the largest mass to proton ratio ( $n+p/p$ ) and are therefore less deflected by the magnetic field of GLAD. The less prominent line below corresponds to  $^{11}\text{C}$  isotopes and on the lower edge few events with  $^{10}\text{C}$  are visible. To identify the number of survived  $^{12}\text{C}$  fragments a graphical selection of the  $^{12}\text{C}$  isotopes - the main diagonal line - is applied.

#### Graphical Selection Algorithm:

- Fit the main diagonal line, which corresponds to the  $^{12}\text{C}$  isotopes, with a linear fit function  $f(x_{mw2}) = a \cdot x_{mw2} + b$ .
- To get the most accurate intersection line between  $^{12}\text{C}$  isotopes and all lighter carbon isotopes the linear fit function from the previous step is taken as starting point. Iteratively the offset value  $b$  is reduced by  $b_i = b_{i-1} - 1$ . For all iteration steps the ratio  $r_{^{12}\text{C}(i)}$  of hits below the linear fit function and the total number of hits in the histogram is calculated.
- The derivative  $\frac{dr_{^{12}\text{C}}(i)}{db_i}$  is calculated.
- Finally the offset  $b_i$  with the largest value for  $\frac{dr_{^{12}\text{C}}(i)}{db_i}$  is selected as cutting line between  $^{12}\text{C}$  isotopes and  $^{11}\text{C}/^{10}\text{C}$  isotopes<sup>33</sup>.

---

<sup>33</sup>For empty target runs the offset  $b$  is manually selected

The ratio  $r_{12C}$  is unaffected by detector efficiencies of MWPC2 and MWPC3<sup>34</sup> and therefore the ratio  $r_{12C}$  can be applied directly as isotope correction to calculate the total interaction cross section:

$$\sigma_I = \sigma_{geo\_corr} + \sigma_{iso}$$

With the isotope correction cross section  $\sigma_{iso}$ :

$$\sigma_{iso} = -\frac{1}{N_t} \ln(r_{12C})$$

To calculate the isotope correction cross section six different methods were employed and compared with each other:

- **MWPC2 and MWPC3 data with own "hit-clustering" level:**

- **MWPC1 and MWPC3 hit-level data:**

To get the ratio  $r_{12C}$  it is necessary to correlate the x position before and after the GLAD magnet. This task can be completed by MWPC3 with respect to MWPC2 or MWPC1. Since the MWPC1 is upstream to MWPC2 the positional distribution of the carbon fragments narrower which as consequence makes it more difficult to disentangle  $^{12}\text{C}$  and  $^{11}\text{C}/^{10}\text{C}$  isotopes, see figure 26. Moreover MWPC1 had two noisy pads which distorts the distribution when using the standard *cal-to-hit* step to get the position value, see figure 26.

- **MWPC1 and MWPC3 data with own "hit-clustering" level:**

Again, to overcome the issue with potentially wrong x-position reconstruction in the MWPCs the own hit clustering reconstruction method, as described above, was applied to MWPC1 and MWPC3 resulting in the 2D plot 27.

- **MWPC2 and MWPC3 with own clustering, quadrant selection in MWPC2:**<sup>35</sup>

The limited geometric acceptance of TWIN MUSIC, described in section 4.4, affects the isotope correction too. The x distribution on the MWPC1/2/3 is cut off on the lower end and the y distribution on the higher end, see figure 23. The  $^{11}\text{C}/^{10}\text{C}$  isotopes are expected to have a broader x and y distribution. Missing the lower and higher edges in the x and y distribution respectively distorts the  $r_{12C}$  ratio towards higher values. This results in a lower cross section contribution of the isotope correction, especially for the low energy runs. To correct for this the x-y distribution in MWPC1 was split into four quadrants, see figure 28. The

---

<sup>34</sup>Under the assumption of constant efficiency over  $x_{mw2}$  and  $x_{mw3}$

<sup>35</sup>I did the quadrant selection also in MWPC2, outcome really similar, TODO: add to appendix...

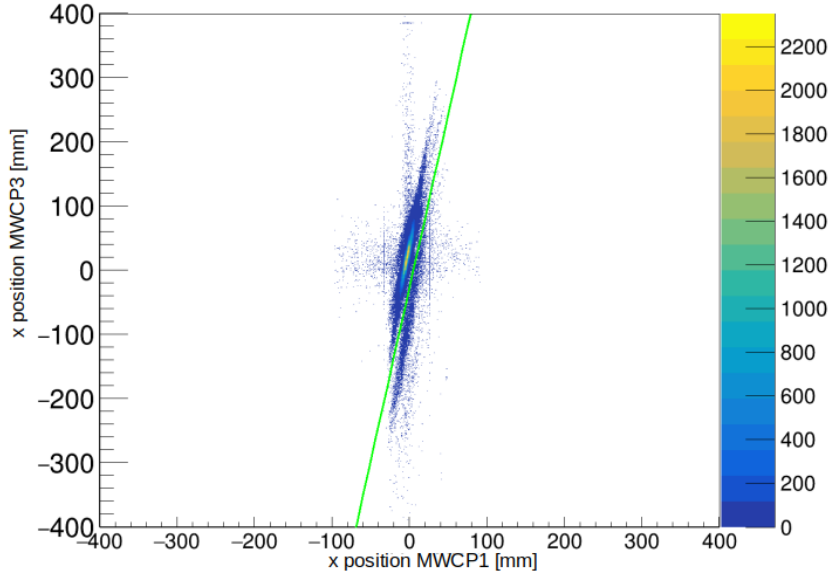


Figure 26: Distribution of x in MWPC1 and MWPC3. Thick target run, beam energy 400 AMeV. The two vertical lines stem from two noisy pads in MWPC1.

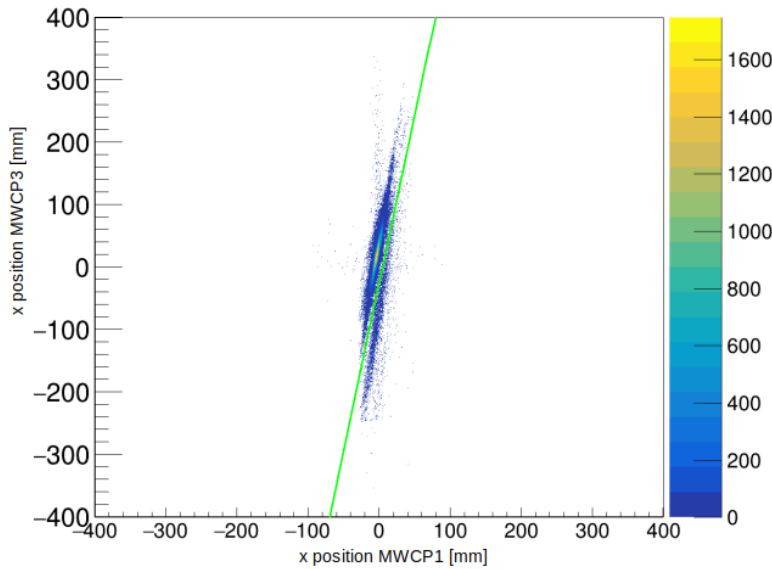


Figure 27: Distribution of x in MWPC1 and MWPC3 using the own hit clustering reconstruction. Thick target run, beam energy 400 AMeV.

intersection lines were derived by the mean of the Gaussian fit of the x and y distribution. The cross section contribution of the isotope correction was measured for all four quadrants.

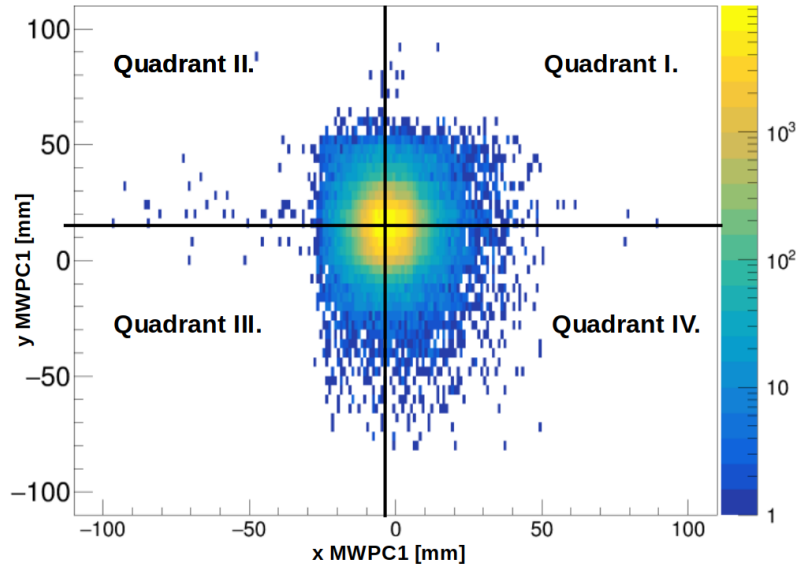


Figure 28: Distribution of x and y in MWPC1 split up in four quadrants. Thick target run, beam energy 400 AMeV.

#### 4.5.1 Results for Isotope Correction Methods

- MWPC2 and MWPC3 hit-level data:

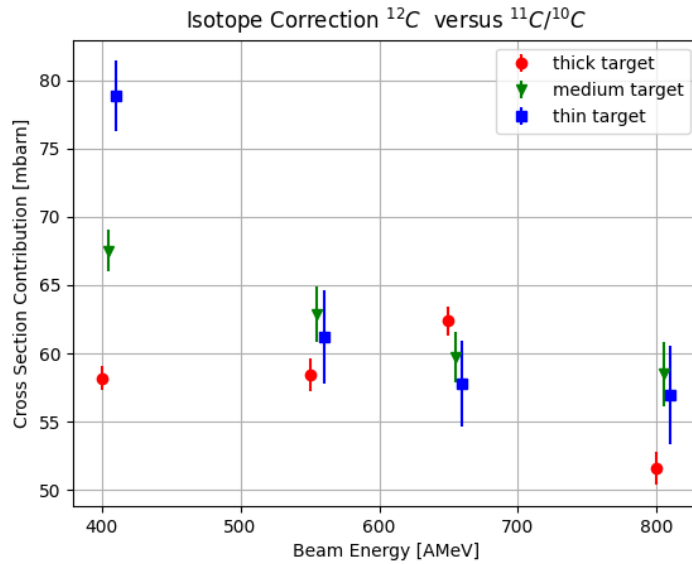


Figure 29: Isotope correction contribution to the total interaction cross section using standard hit level data in MWPC2 and MWPC3.

- MWPC2 and MWPC3 data with own "hit-clustering" level:
- MWPC1 and MWPC3 hit-level data:
- MWPC1 and MWPC3 data with own "hit-clustering" level:
- MWPC2 and MWPC3 with own clustering, quadrant selection in MWPC1:

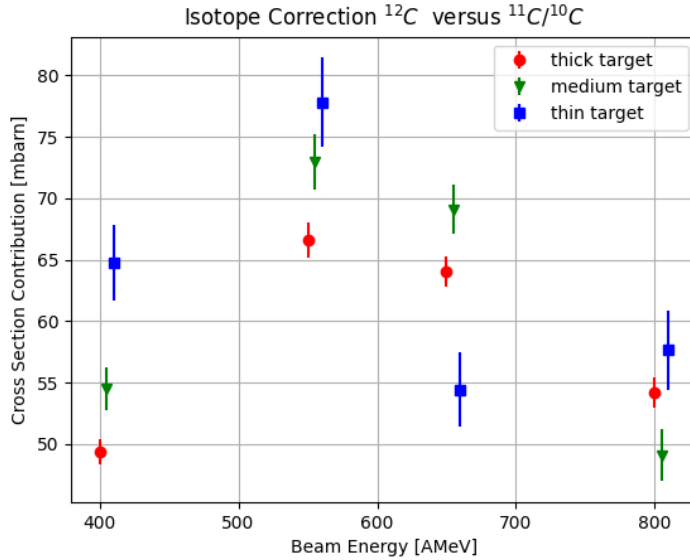


Figure 30: Isotope correction contribution to the total interaction cross section using own hit clustering in MWPC2 and MWPC3.

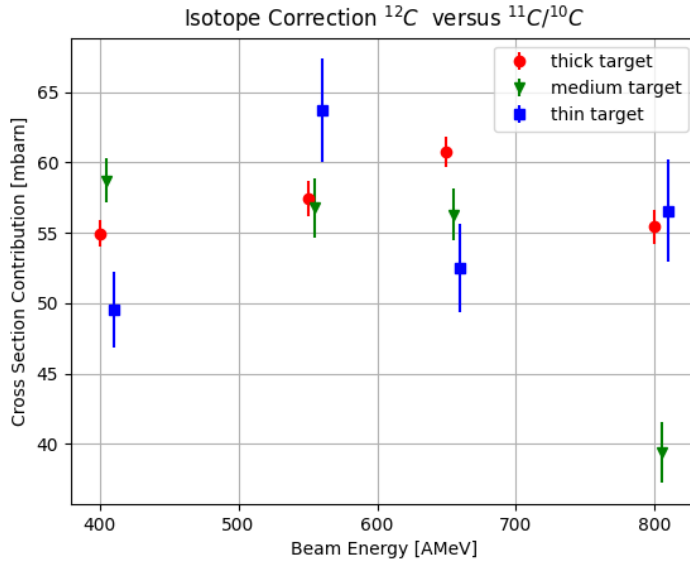


Figure 31: Isotope correction contribution to the total interaction cross section using standard hit level data in MWPC1 and MWPC3.

## 4.6 Statistical and Systematic Error Analysis

All three measurements presented in this section, the charge changing cross section, the isotopic cross section correction cross section and the total interaction cross section, rely on the transmission method and the error analysis of those measurements are treated the same accordingly. The generic formula for all three measurements was presented in

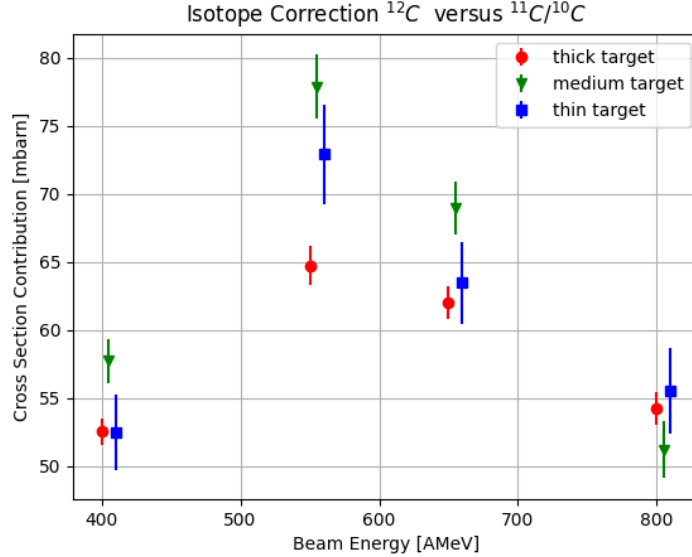


Figure 32: Isotope correction contribution to the total interaction cross section using own hit clustering in MWPC1 and MWPC3.

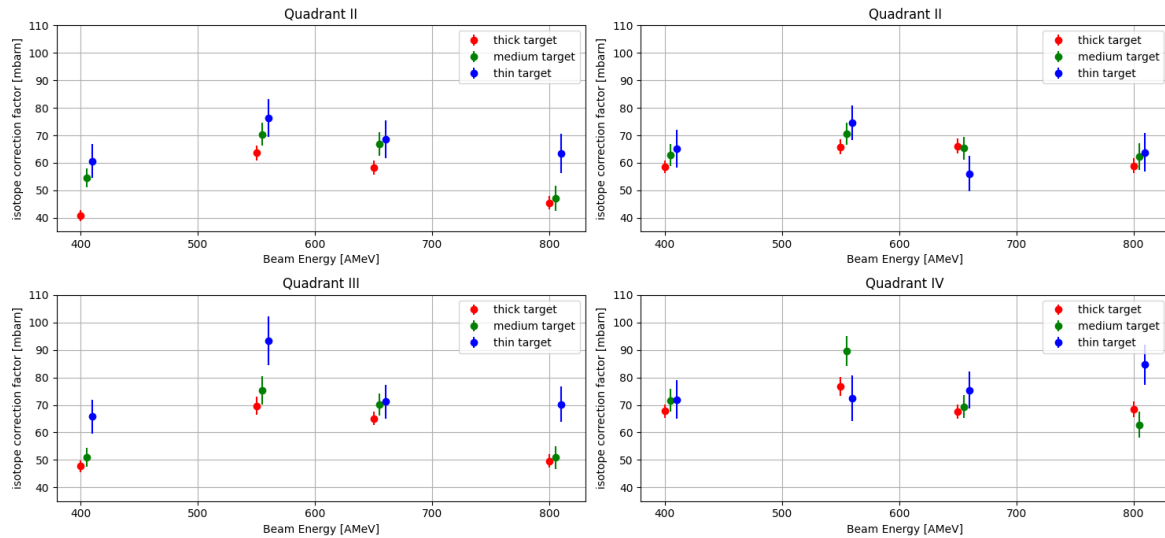


Figure 33: Isotope correction contribution to the total interaction cross section using own hit clustering in MWPC2 and MWPC3. Comparison for different quadrant selection in MWPC1. Quadrant four is the preferred one as it is not affected by limited geometric acceptance of TWIN MUSIC.

section 4.1, equation 18.

Since all quantities in equation 18 are mutually independent, the Gaussian error prop-

agation for statistical and systematical uncertainties is given by:

$$\Delta_{\text{stat./syst.}} = \sqrt{\sum_{i=1}^n \left( \frac{\partial f}{\partial x_i} \cdot \Delta_{x_i} \right)^2} \quad (32)$$

with:

- $f(x_1, x_2, \dots, x_n)$  the error prone cross section function,
- $x_i$  the independent variables ( $N_1, N_2, N_t$ ; see equation 18),
- $\Delta_{x_i}$  stat./syst. uncertainties associated to independent variable  $x_i$

#### 4.6.1 Statistical Uncertainties

For the charge changing cross section the combined statistical error is:

$$\Delta\sigma_{\text{stat.|cc}} = \sqrt{\left( \frac{\partial\sigma_{cc}}{\partial N_t} \Delta N_t \right)^2 + \left( \frac{\partial\sigma_{cc}}{\partial P_{\text{surv|cc}}} \Delta P_{\text{surv|cc}} \right)^2 + \left( \frac{\partial\sigma_{cc}}{\partial P_{\text{surv|cc}}^E} \Delta P_{\text{surv|cc}}^E \right)^2} \quad (33)$$

where  $\Delta N_t$  accounts for the uncertainty in the measurement of the target thickness.  $P_{\text{surv|cc}}$ , the surviving probability of having a carbon isotope in the final state, follows a binomial distribution with  $N_1$  independent experiments and a boolean valued reaction output (survived vs. non-survived). Therefore  $P_{\text{surv|cc}}$  follows the standard error of binomial distributed variable:

$$\Delta P_{\text{surv|cc}}^{(E)} = \sqrt{\frac{P_{\text{surv|cc}}^{(E)} \cdot (1 - P_{\text{surv|cc}}^{(E)})}{N_1^{(E)}}} \quad (34)$$

Inserting in equation 33 gives:

$$\Delta\sigma_{\text{stat.|cc}} = \sqrt{\left( \frac{\sigma_{cc}\Delta N_t}{N_t} \right)^2 + \frac{1}{N_t^2} \left( \frac{1 - P_{\text{surv|cc}}}{P_{\text{surv|cc}}N_1} + \frac{1 - P_{\text{surv|cc}}^{(E)}}{P_{\text{surv|cc}}^{(E)}N_1^E} \right)} \quad (35)$$

Similar for the isotopic correction cross section with  $P_{\text{surv|iso}}$  the ratio of reconstructed  $^{12}\text{C}$  isotopes to all identified carbon isotopes in the x-position correlation plots for MWPC2 and MWPC3:

$$\Delta\sigma_{\text{stat.|iso}} = \sqrt{\left( \frac{\sigma_{iso}\Delta N_t}{N_t} \right)^2 + \frac{1}{N_t^2} \left( \frac{1 - P_{\text{surv|iso}}}{P_{\text{surv|iso}}N_1} + \frac{1 - P_{\text{surv|iso}}^{(E)}}{P_{\text{surv|iso}}^{(E)}N_1^E} \right)} \quad (36)$$

For viewing the statistical uncertainties of the total interaction cross section measurements the uncertainties in the target thickness as well as the uncertainties of the carbon

isotope surviving probability  $P_{surv|cc}$  and the  $^{12}C$  surviving probability  $P_{surv|iso}$  have to be accounted for:

$$\Delta\sigma_{\text{stat. tot}} = \sqrt{\left(\frac{\sigma_{tot}\Delta N_t}{N_t}\right)^2 + \frac{1}{N_t^2} \left( \frac{1 - P_{surv|cc}}{P_{surv|cc}N_1} + \frac{1 - P_{surv|cc}^{(E)}}{P_{surv|cc}^{(E)}N_1^E} \right) + \frac{1}{N_t^2} \left( \frac{1 - P_{surv|iso}}{P_{surv|iso}N_1} + \frac{1 - P_{surv|iso}^{(E)}}{P_{surv|iso}^{(E)}N_1^E} \right)} \quad (37)$$

#### 4.6.2 Systematic Uncertainties

### 4.7 (Preliminary) Results Total Interaction Cross Section

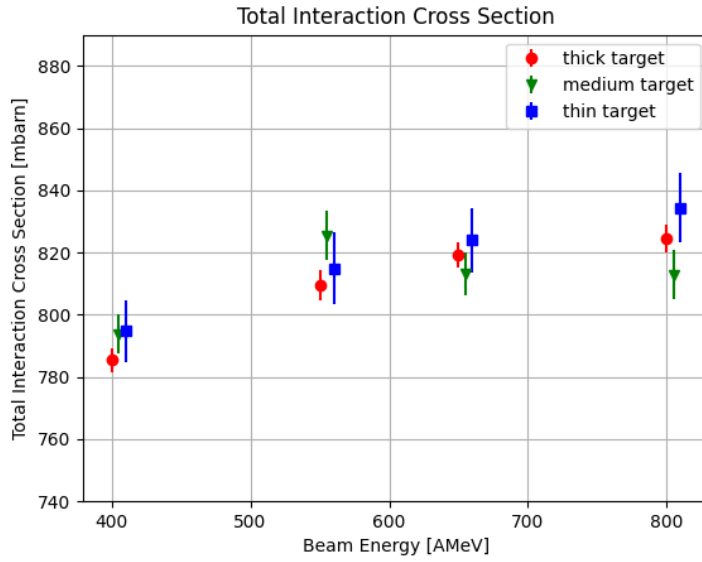


Figure 34: Total interaction cross section using the quadrant IV. selection in MWPC1 x-y plot (see figure 28) for the isotope correction and applying the geometric correction on the charge changing cross section.



## 5 Qualitative Analysis -

### Quasi-Free Scattering $^{12}\text{C}(\text{p},2\text{p})^{11}\text{B}$

Until the S444 experiment in 2020 CALIFA consisted out of a prototype frame filled with up to 64 CsI(Tl) crystals. The geometric coverage was therefore limited. For the S444 experiment CALIFA got its final frame and was fully filled in the forward barrel and 35%filled in the iPhos region, CEPA was not installed yet. With these improvements it was possible to commission QFS-experiments with CALIFA at  $\text{R}^3\text{B}$ . In the follow up experiment S467, also in 2020, the first experimental run to study single-particle structures of neutron-rich Ca isotopes via QFS reactions was carried out.

Even though great improvements in the detector development were achieved the correction factors to correct for geometric acceptance would be much too high ( $\approx 10$ ) for precise cross section measurements for QFS-reactions since the correction factors would in turn rely on a simplified reaction model. A precise analysis of the acceptance correction factor and the development of a more sophisticated and data driven reaction model is out of the scope of this work. Therefore this analysis focuses on the methods of QFS-reaction identification and the extraction of the key information discussed in section 2.5. TODO: add more stuff here...

#### 5.1 Setup-Calibration

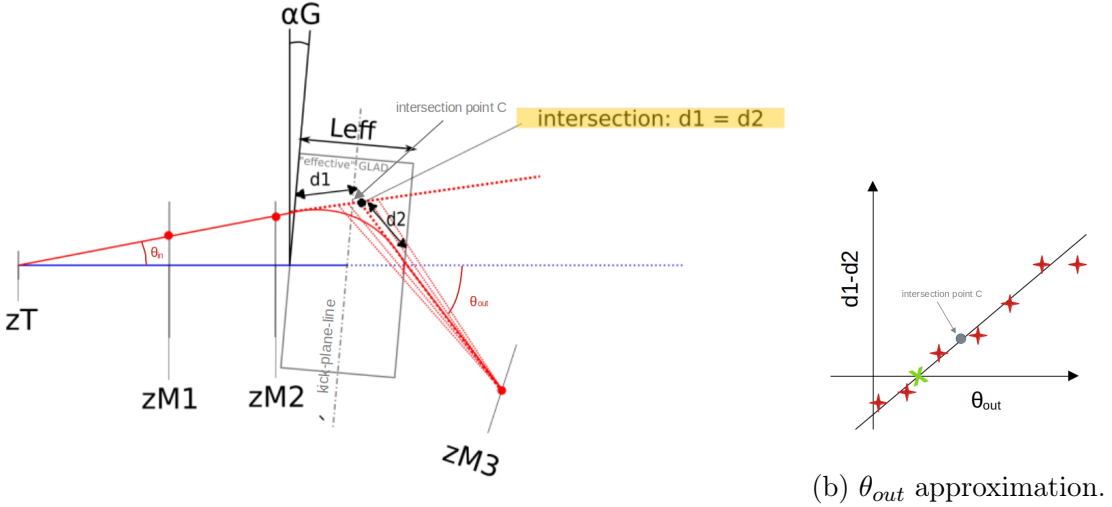
For setup description refer to section 4. For all detectors except the SOFIA (Study On FIission with Aladin) Time of Flight Wall the calibration parameters investigated by the respective detector-expert group were adopted. Herefore we will subsequently only describe the Time of Flight Wall calibration in this subsection.

##### 5.1.1 Flight-Path Reconstruction

The procedure to calibrate the Time of Flight (ToF) Wall involves beforehand a precise flight-path reconstruction of the projectile from the entrance of Cave C downstream to the ToF Wall. Since only one tracking detector downstream to GLAD was in operation for the S444 experiment no angle of the deflected fragment/beam  $\theta_{out}$  could be directly extracted. Herefore an advanced tracking algorithm was developed, motivated from ref. [65] (section 3.4).

- The first step is to measure the scattering angle after target,  $\theta_{in}$ , and draw an extended line from the target position through the effective magnetic field of GLAD.

- Draw a trajectory line from the hit position in MWPC3 to the intersection point C (see figure 35a) of the "kick-plane-line" and the reconstructed and extended track line upstream to GLAD.
- Now sweep along the reconstructed track line upstream to GLAD. For each step a value for  $\theta_{out}$  and  $d1 - d2$  is gathered, see figure 35b.
- As in figure 35b shown, fit the data-points from previous step with a linear fit function and find the corresponding  $\theta_{out}$  value where the fit line intersects with the abscissa. This corresponds to the case where  $d1 = d2$ . This is the approximated "kickpoint" in GLAD.
- Previous steps need to be executed for all events accordingly.



(a) Flightpath reconstruction with "Leff" being the effective active width of the magnetic field of GLAD For detailed information see text.

Figure 35: Flightpath tracking and reconstruction of the fragment/beam after the target.

Now that the scattering angle after the target  $\theta_{in}$  and the angle after GLAD,  $\theta_{out}$  is known and the position outside the magnetic field of GLAD are fixed, with  $(z_1, x_1)$  the entrance point on the GLAD field and  $(z_2, x_2)$  the exit point, the bending radius  $r$  from the magnetic deflection can be determined:

$$r = \frac{L_{eff}}{2 \cdot \sin\left(\frac{\theta_{in} + \theta_{out}}{2}\right) \cdot \cos\delta} \quad (38)$$

where  $L_{eff}$  is the effective active width of the magnetic field of GLAD, which corresponds  $L_{eff} \approx 2.06 \text{ m}$ . This value could also be verified by extracting  $L_{eff}$  from the formula

for the magnetic rigidity  $B \cdot r = \gamma\beta m/q$  for empty target runs with known values of the B-field<sup>36</sup>.

The angle  $\delta$  in equation 38 is given by the trajectory line going through  $(z_1, x_1)/(z_2, x_2)$  and the line parallel to the GLAD magnet width  $L_{eff}$ .

A detailed derivation of equation 38 can be found in appendix G. The arc trajectory  $l_{GLAD}$  of the fragment within GLAD can be reconstructed using the bending radius  $r$  and the entry and exit points  $(z_1, x_1)/(z_2, x_2)$ :

$$l_{GLAD} = r \cdot \omega \quad \text{with} \quad \omega = 2 \cdot \arcsin(t_{1/2}(2 \cdot r)) \quad (39)$$

where  $\omega$  is the central angle and  $t_{1/2}$  is the cord length between  $(z_1, x_1)$  and  $(z_2, x_2)$ .

At this stage the full pathlength  $L$  from the Start detector to the ToFW is fixed:

**From Start to the target  $l_{ST}$ :** For this path section a straight flightpath parallel to the z-coordinate is assumed. The pathlength is taken from the position measurements of the Start detector and the target accordingly ( $= 118.3\text{ cm}$ ).

**Target to GLAD entrance point  $(z_1, x_1)$ ,  $l_{in}$ :** For the exact position assignment of  $(z_1, x_1)$  both MWPC1 and MWPC2 position measurements have been calibrated with empty target runs by including an offset value in order to center the x-position in both detectors around zero. From the position measurement of the central position of GLAD, its tilting angle  $\alpha$  and  $L_{eff}$  the intersection point of the fragment trajectory before GLAD and the "effective GLAD magnetic field rectangle",  $(z_1, x_1)$ , can be determined and with it the according flightpath section  $l_{in}$ .

**Arc trajectory within GLAD,  $l_{GLAD}$ :** This flightpath passage is determined by reconstructing  $(z_1, x_1)$  and  $(z_2, x_2)$ , as it has been described in detail in the previous section. Hence the magnetic bending radius can be determined, see equation 38, and finally the arc trajectory  $l_{GLAD}$  as in equation 39.

**GLAD exit point  $(z_2, x_2)$  to ToFW,  $l_{out}$ :** The hit position  $(z_{MWPC3}, x_{MWPC3})$  in MWPC3 is given by the reconstructed hit position in this detector and the position measurement of the detector itself. The exit point  $(z_2, x_2)$  was reconstructed in the previous steps. Hence the trajectory line from  $(z_2, x_2)$  to  $(z_{MWPC3}, x_{MWPC3})$  is fixed and is expanded to the intersection with the ToFW plane for the concluding  $l_{out}$  measurement.

---

<sup>36</sup>For detector calibration, primarily for the ToFWall, we had several "empty sweep runs", with empty target and different B-field strength settings. Those runs were optimal to validate  $L_{eff}$ .

The resulting flightpath  $L$  recombines from:

$$L = l_{ST} + l_{in} + l_{GLAD} + l_{out}$$

In the flightpath reconstruction the deflections in the y-dimension were omitted as the angular straggling in the target is small (TODO: give sigma value) and since the deflection of the fragment within GLAD is independent from its y-position this contribution can be disregarded.

### 5.1.2 Time of Flight Calibration

For the time of flight measurement in the S444 setup the time is recorded and digitized by the VFTX, VME-FPGA Time-to-Digital Converter (TDC) Modules based on tapped delay line (TDL) TDCs[66]. These modules provide for each detected signal a coarse time, is determined by counting cycles of a 200 MHz readout clock, resulting in a 5 ns binning resolution, and a fine time, which is obtained using an FPGA-based Time-to-Digital Converter (TDC), which employs a tapped delay line (TDL). In this approach, the signal propagates through a series of delayed logic modules within the FPGA until the subsequent clock cycle terminates the sampling process. The number of delay elements traversed by the signal is used to compute the time difference between the signal onset and the end of the clock cycle. The translation of the resulting fine time, with reasonable assumption of an uniform distribution, is achieved via a calibrated linear function. This procedure assigns to each preamplifier signal in the start detector (left/right) and the ToF Wall (up/down) a calibrated raw time  $raw\_t$ :

$$raw\_t = coarse\_time\_clocks \cdot 5\text{ns} + offset[fine\_time]$$

Finally, the raw time of flight is reconstructed by combining all four time measurements:

$$RawTof = 0.5 * (raw\_t_{i,down} + raw\_t_{i,up}) - 0.5 * (raw\_t_{start,right} + raw\_t_{start,left}) \quad (40)$$

where  $i$  ( $\in 0 \dots 27$ ) refers to the scintillator number of the ToF Wall. Since the mentioned time measurements are standalone and not synchronized the  $RawTof$  has to be corrected by an offset which has to be determined again for each scintillator bar  $i$  of the ToF Wall:

$$\Delta_{ToF}[i] = \overline{L[i]} / v_{beam} - \overline{RawTof[i]}$$

where  $\overline{L[i]}$  is the mean reconstructed path length for all events in empty target runs which hit scintillator bar  $i$  of the ToF Wall. The beam velocity  $v_{beam}$  is directly taken from the given beam settings, e.g. 400 AMeV beam, empty target corresponds to

$v_{beam} = 214,2\text{mm/ns}$ . The mean raw ToF  $\overline{\text{RawTof}[i]}$  again results from all events which hit scintillator bar  $i$  and is extracted from the mean value of a Gaussian fit to the raw ToF. The resulting calibrated ToF can then be expressed as:

$$\text{ToF}[i] = 0.5 * (\text{raw\_}t_{i,\text{down}} + \text{raw\_}t_{i,\text{up}}) - 0.5 * (\text{raw\_}t_{\text{start,right}} + \text{raw\_}t_{\text{start,left}}) + \Delta_{\text{ToF}}[i]$$

To estimate the time of flight resolution for events with hit in ToF Wall bar  $i$  it has to be noted that the ToF is affected by the flight path. Hence the the time of flight should be written as:

$$\widetilde{\text{ToF}} = \frac{\overline{L[i]}}{\frac{L[i]}{\text{ToF}[i]}}$$

$\overline{L[i]}$  is the mean pathlength, whereas  $L[i]$  and  $\text{ToF}[i]$  are event-wise selected. By reconstructing the fligh-path as described in subsection 5.1.1 and employment of the mentioned time calibration steps the average time resolution  $\sigma_t$  results  $\approx 90\text{ps}$ <sup>37</sup>.

## 5.2 Event Selection

For the precise measurement of the total interaction cross section  $^{12}C + ^{12}C$ , as detailed in the section 4, event selection was of critical importance, requiring stringent cuts on the TPats (see table 4), as well as on the charge and position of the incoming particles. In contrast, for this qualitative QFS analysis, these factors played a minor role, allowing for only minimal cuts on the incoming ions:

- Both left and right preamplifiers of the start detector have seen a coincident signal.
- Exactly one hit in MWPC0 in the hit-level data.

However, for the identification of fragments downstream of the target, various detector signals and event parameters are required:

- One hit (in the hit-level data) in the MWPC tracking detectors, MWPC1 and MWPC2 upstream to GLAD, MWPC3 downstream to GLAD.
- Charge measurement in the TWIN-MUSIC.
- One hit scintillation bar in ToF Wall with signal from both up/down PMTs.

---

<sup>37</sup>To remove events with large angular straggling, a cut of  $\pm 20\text{mm}$  on the beam spot for the y-position on the MWPC3 was applied.

### 5.3 Fragment Identification

The first step for the identification of the QFS-reaction channel  $^{12}C(p, 2p)^{11}B$  is the identification of the fragment  $^{11}B$  via the formula for the magnetic rigidity:  $B \cdot r = \gamma\beta m/q$  where the  $\gamma$  factor accounts for the increase in momentum for relativistic particles. From the flightpath reconstruction and the ToF measurement as described in previous sections  $r, \beta$  and  $\gamma$  are obtained whereas the charge of the fragment  $q$  is measured by the energy loss ( $\Delta E \sim Z^2$ ) in the TWIN MUSIC detector.

The measured values for  $\frac{A}{q}$  and  $q$  are shown in figure 36 where the fragment of interest  $^{11}B$  is expected to be at  $\frac{A}{q} = 11/5 \approx 2.2$  and  $q = 5$ . The correlation plot exhibits a broad distribution in  $\frac{A}{q}$ , which may result from misidentification of hit positions in one of the MWPC tracking detectors when multiple signal hits occur. Even minor deviations in MWPC1 and MWPC2 can significantly affect the radius reconstruction, thereby impacting the accuracy of the  $\frac{A}{q}$  determination.

An intriguing feature is the distinct cluster observed at  $Z \approx 8.5$  and  $\frac{A}{q} \approx 2$ , which corresponds to pileup events. These occur when two ion signals arrive within a short time window in the TWIN MUSIC detector, preventing them from being resolved as separate events and instead being reconstructed as a single signal<sup>38</sup>. Moreover attention should be paid that it seems to be there a cut from analysis side at  $Z \approx 4$ . This is actually not the case. The TWIN MUSIC was optimized for the subsequent experimental run S467 with *Ca* isotopes and therefore the charge measurement was optimized for  $Z \approx 20$ . Everything below  $Z \approx 4$  was below the signal threshold of TWIN MUSIC.

Furthermore, it is important to note the apparent cut at  $Z \approx 4$  in the data. However, this is not an artifact of the analysis but rather a consequence of the experimental setup. The TWIN MUSIC detector was optimized for the subsequent S467 experiment, which focused on calcium isotopic chain ( $Z = 20$ ). As a result, the charge measurement was calibrated for  $Z \approx 20$ , and signals corresponding to  $Z \lesssim 4$  fell below the detection threshold of TWIN MUSIC.

For this qualitative analysis, the upper charge bound of  $^{11}B$  was determined by locating the intersection point of the Gaussian-fitted distributions corresponding to the  $Z = 5$  and  $Z = 6$  peaks. The lower bound was set by applying an offset of minus one unit.

A similar approach was employed to select the specific boron isotope  $^{11}B$ . The charge selection was performed using the previously defined boundary cuts. To isolate the  $^{11}B$  isotopes, the lower bound was determined by identifying the intersection point of

---

<sup>38</sup>For instance, if two carbon ions ( $Z = 6$ ) interact simultaneously, the total energy loss within TWIN MUSIC is approximately twice that of a single ion. Since the energy loss follows the relation  $\Delta E \sim Z^2$ , the reconstructed charge is given by  $\sqrt(2) Z_{carbon} \approx 8.5$ .

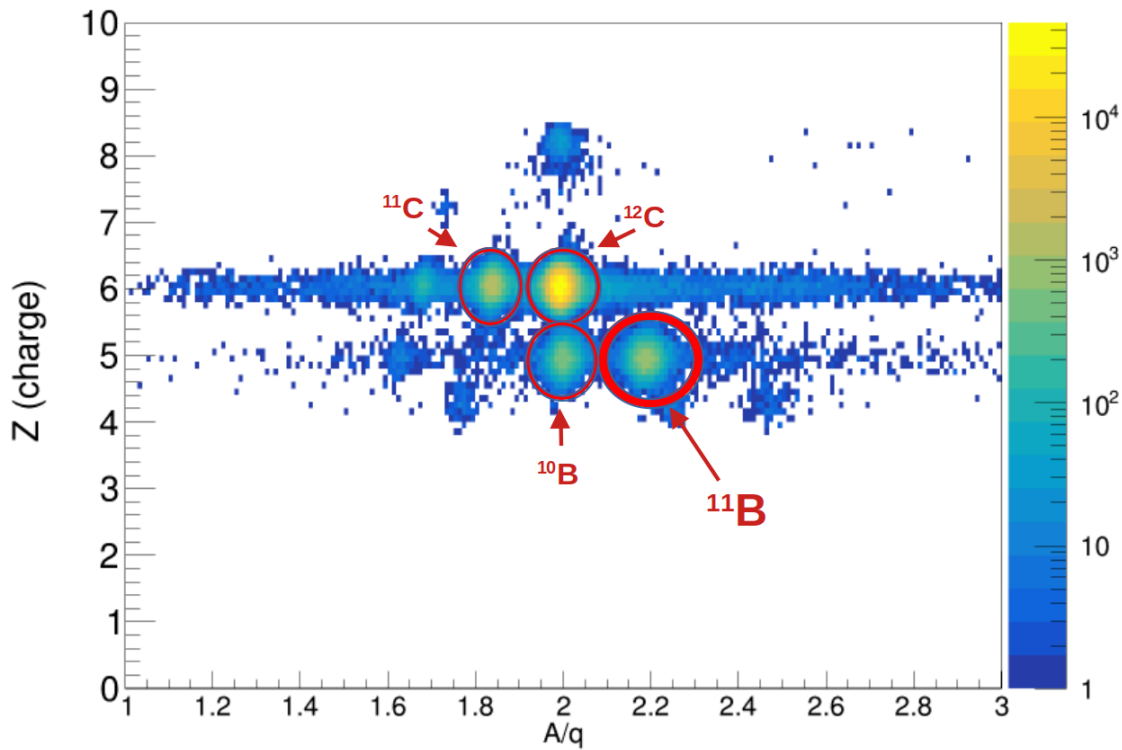


Figure 36: Fragment identification is performed using the correlation between the atomic number  $Z$  and the mass-to-charge ratio  $\frac{A}{q}$ . For the quasi-free scattering (QFS) analysis of the reaction  $^{12}C(p,2p)^{11}B$ , the fragment of interest is  $^{11}B$ , which is emphasized with a bold red circle.

the Gaussian-fitted distributions corresponding to the  $^{10}B$  and  $^{11}B$  peaks. The upper bound was established by measuring the distance from this intersection point to the peak of  $^{11}B$ .

## 5.4 QFS-Protons

Following the identification of the fragments through precise flight path reconstruction and time measurement, as detailed in the previous subsection, and the subsequent selection of the  $^{11}B$  isotope, the analysis focuses on the two correlated protons to fully characterize the quasi-free scattering channel  $^{12}C(p, 2p)^{11}B$ .

For a proper interpretation of the data, it is essential to consider the geometric acceptance of CALIFA during the S444 experiment in 2020. The central *BARREL* region (Ring 3 and Ring 4), covering the polar angular range from  $43^\circ$  to  $88^\circ$ , was fully operational. In contrast, the forward region, referred to as *iPhos* ( $19^\circ$  to  $43^\circ$ ), was only partially equipped, with a coverage of approximately 35%. The forward endcap, known as *CEPA*, was not installed, and the backward barrel remained unoccupied. The corresponding geometry is illustrated in figure 37.

For the proton selection and the application of reasonable cuts it is important to un-

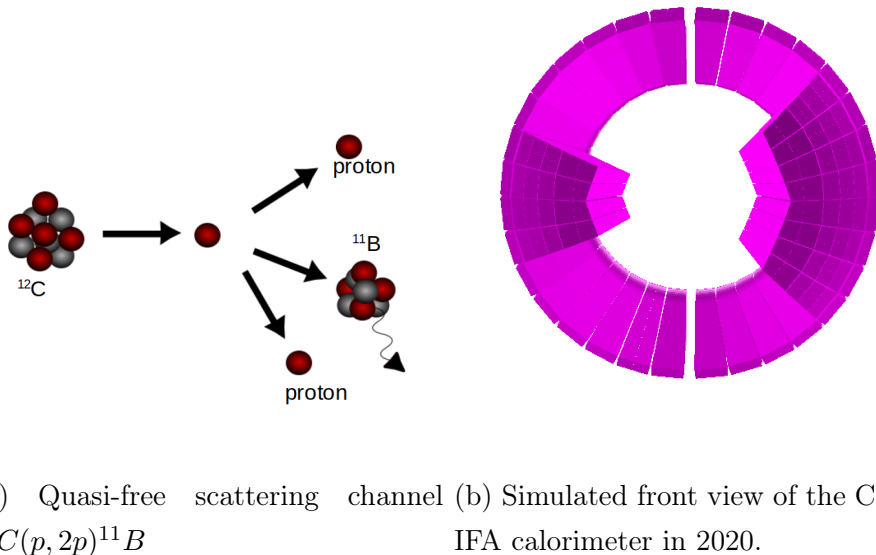


Figure 37: Tagging the  $^{12}C(p, 2p)^{11}B$  channel with only partly filled CALIFA calorimeter for the detection of the two correlated protons.

derstand the processing steps of the raw *mapped* level data to the *cal* level and finally *hit* level data. The *mapped* level data has following structure for each CALIFA hit: For an accurate proton selection and the application of appropriate cuts, it is crucial

to understand the data processing steps from the raw *mapped*-level to the *cal*-level and finally to the *hit*-level. The *mapped*-level data for each CALIFA hit is structured as follows:

- CrystalID: each crystal channel gets assigned a unique ID. Gamma range channels are in the range up to 2550, proton range ones from 2550 up to ..
- Uncalibrated Energy
- Slow Component  $N_s$ , extracted from the signal shape, see [51], section 2.
- Fast Component  $N_f$ , extracted from the signal shape, see [51], section 2.
- WRTS: White Rabbit Time Stamp[67], interpolated from FEBEX inner clock.
- Time over Threshold, optionally activated for  $\gamma$ -range channels to reconstruct energies beyond range.

The *cal*-level data is structured as in the *mapped*-level, however with calibrated energy by applying the calibration parameters from calibration run to each crystal channel.

For the calibration runs a  $^{22}Na$  (with peaks at 511keV and 1275keV) or a  $^{60}Co$  (with peaks at 1173keV and 1332keV) source is used. For each crystal channel a linear fit on the two photo-peaks is performed. Using this fitting function, the uncalibrated energy, expressed in energy channels, can be converted into calibrated energy values.

For the final *hit*-level data, the energy-calibrated hits from the *cal*-level are merged into clusters. High-energy proton hits ( $E_{hit} > 15MeV$ ) and low-energy  $\gamma$  hits are first listed and sorted in descending energy order. Clusters are then formed using a cone-shaped approach, where each cluster is centered around the highest-energy hit with a half-opening angle of  $\theta_c = 14.3^\circ$ . All hits within this angular region are merged into the cluster. This process is iteratively repeated until both the high- and low-energy lists are empty. To improve the signal-to-noise ratio in this analysis, hits with energy values below the threshold of  $E_{thr} = 100keV$  are discarded during clustering.

The resulting correlations in azimuthal and polar angles, with the only cut to have at least two high energy clusters with energy larger 15 MeV, with respect to the simulated  $p2p$ -simulations are shown in figure 38 and figure 39 accordingly.

From the azimuthal correlation plot in Figure 38, the geometric acceptance limitations of CALIFA become evident. In the so-called *iPhos* region, CALIFA was instrumented only within the azimuthal ranges of  $\pm 45^\circ$  and  $157.5^\circ$  to  $202.5^\circ$ . Due to relativistic kinematics, both protons undergo a forward boost, leading to their predominant detection in the iPhos array. Consequently, any acceptance loss in this region has a substantial

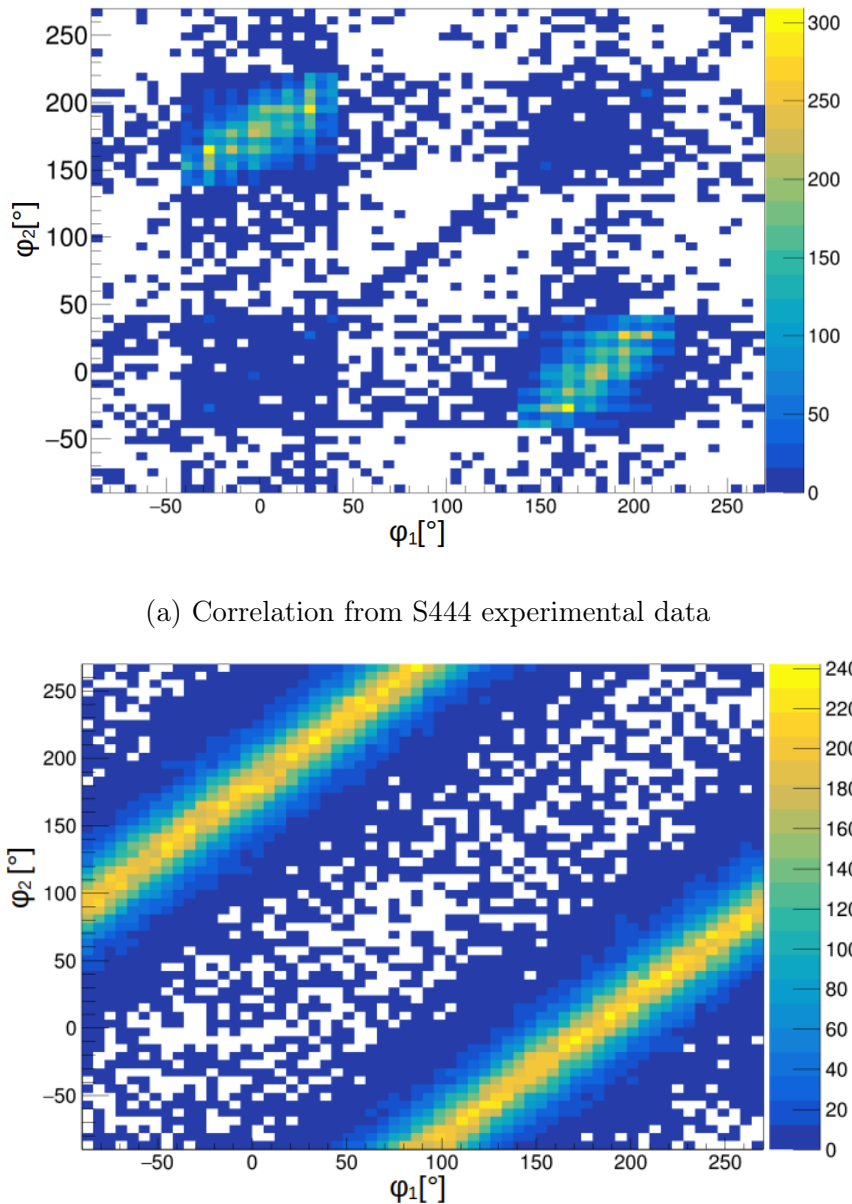


Figure 38: Azimuthal angular correlation  $\varphi_1$  versus  $\varphi_2$  of the two clusters with highest energy in CALIFA

impact on the overall detection efficiency.

Moreover, the correlation plot exhibits a distinct correlation line at  $\varphi_1 \approx \varphi_2$ . This feature primarily arises from inaccuracies in cluster reconstruction, where proton cluster hits fall outside the predefined cone size of the reconstruction algorithm, resulting in the erroneous identification of two separate hits. This effect is particularly pronounced in the *iPhos* region as it is the primary detection region for the protons. Such misidentified events are systematically excluded in analyses focusing on the clean  $^{12}C(p, 2p)^{11}B$  channel.

The polar angular correlation in figure 39 shows as expected a strong anti-correlation between the two proton clusters. For beam energies up to approximately 500 AMeV the anti-correlation line is expected to be uniformly distributed over the polar range as the momentum transfer  $t = -Q^2$ , which defines the angular distributions  $\theta_{1/2}$ , does not effect the cross section in this energy regime<sup>39</sup>.

Moreover in figure 39 the two off-diagonal lines should be noted. This artifact arises from wrong cluster reconstruction where proton cluster hits fall outside the predefined cone size of the reconstruction algorithm, resulting in the erroneous identification of two separate hits. As the resulting clusters are in close proximity, they exhibit a systematic offset from the diagonal in the polar angular correlation plot.

The information of azimuthal and polar angles of the two protons can merged in the opening angle of the two reconstructed protons via the geometric formula:

$$\theta_{p2p} = \arccos(\sin(\theta_1)\sin(\theta_2)\cos(\varphi_2 - \varphi_1) + \cos(\theta_1)\cos(\theta_2)) \quad (41)$$

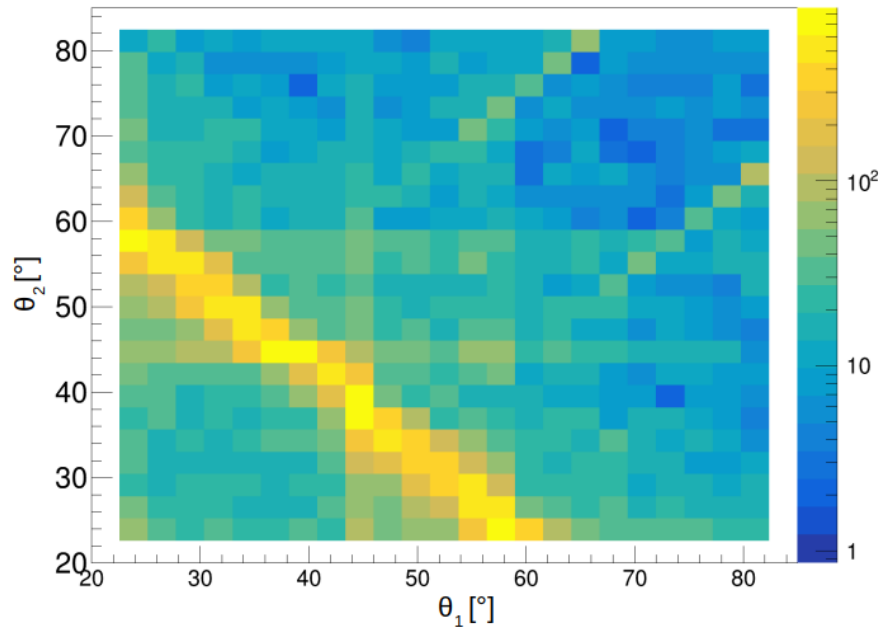
Figure 40 presents the opening angle  $\theta_{p2p}$  for the reconstructed protons. In both the simulated and experimental data, the distribution exhibits a peak at approximately 81°. While the simulated distribution shows a strict upper limit around 82°, the experimental data features a pronounced tail extending toward larger values. This effect is primarily attributed to final-state interactions (FSI) and can be significantly reduced by applying appropriate selection criteria to the polar and azimuthal angular correlations of the two reconstructed high-energy hits.

Herefore in the next considerations only events with following criteria are selected:

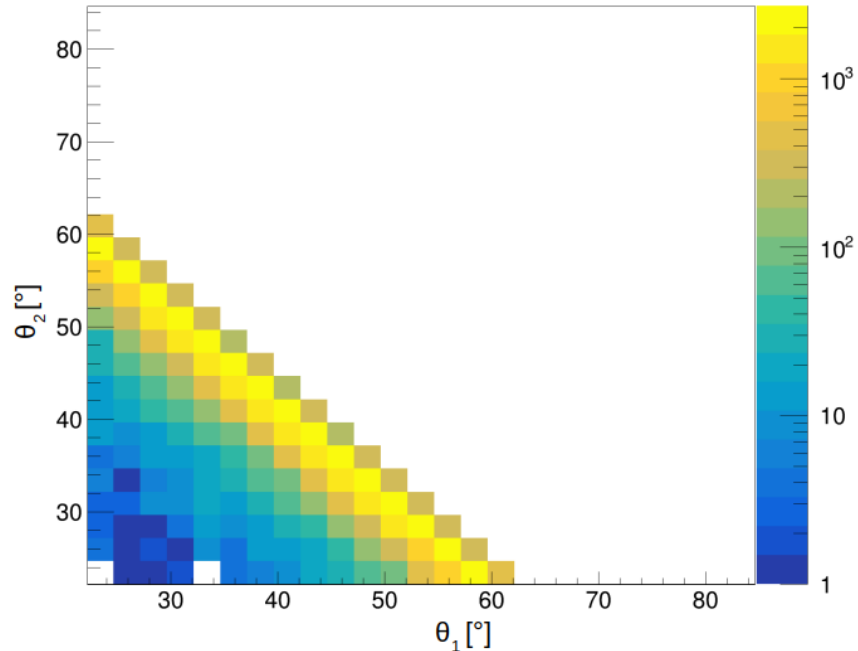
- $\theta_1 + \theta_2 < 90^\circ$
- $\Delta\varphi < 180 \pm 40^\circ$

---

<sup>39</sup>At higher beam energies, parameterizations of the cross section as a function of  $t$  often take the form  $\frac{d\sigma}{dt} = Ce^{bt}$ , where  $C$  and  $b$  are empirically determined parameters.



(a) Correlation from S444 experimental data



(b) Simulated data using based on QFS kinematical code by Leonid Chulkov, GSI.

Figure 39: Polar angular correlation  $\theta_1$  versus  $\theta_2$  of the two clusters with highest energy in CALIFA

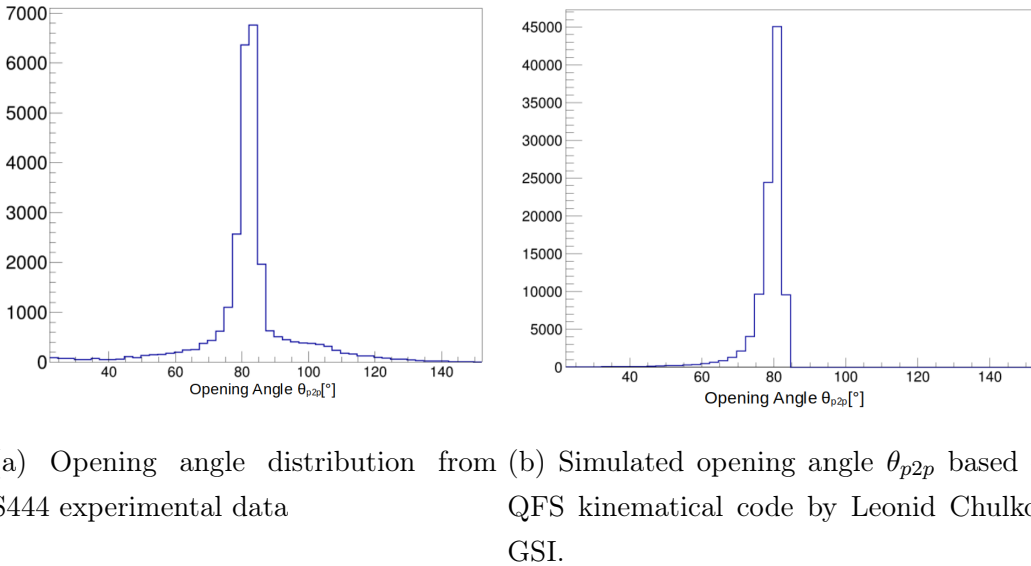


Figure 40: Reconstruction of the opening angle  $\theta_{p2p}$  as in equation 41 from the two clusters with highest energy in CALIFA

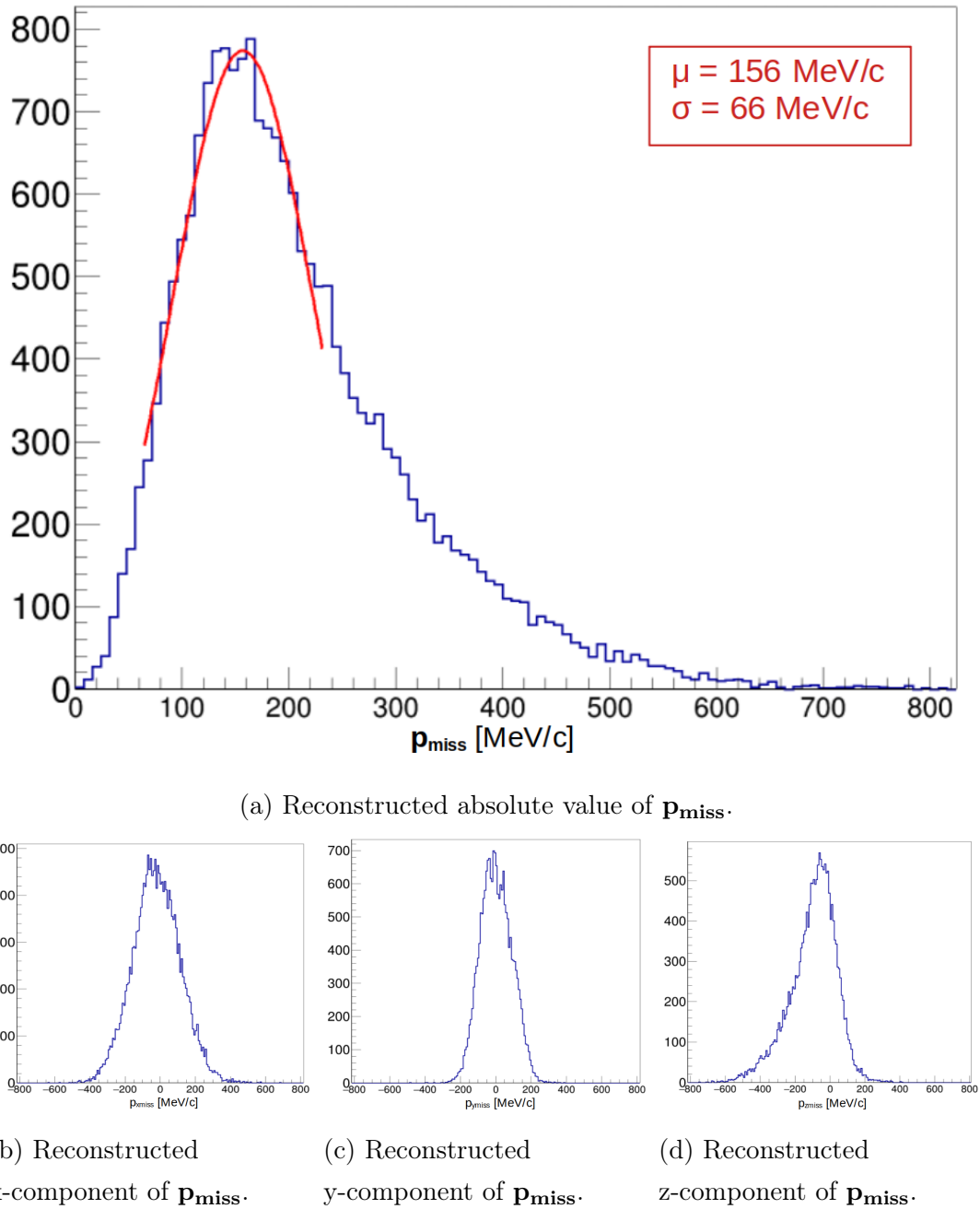
#### 5.4.1 Missing Momentum $\mathbf{p}_{\text{miss}}$ Reconstruction

As discussed in Section 2.5, the momentum of the knocked-out proton inside the  $^{12}C$  nucleus can be reconstructed, assuming higher-order perturbations are negligible, as described by Equation 8. For this reconstruction, the momenta of the two detected protons,  $\mathbf{p}_{1/2}$ , and the initial target proton,  $\mathbf{p}_0$  (which is approximately zero in the laboratory frame), must be known and transformed into the center-of-mass frame of the  $^{12}C$  nucleus. The resulting distribution of the missing momentum,  $\mathbf{p}_{\text{miss}}$ , obtained from experimental data, is presented in Figure 41.

Compared to previous experimental results, such as those reported in Ref. [14], where the measured Fermi momentum for  $^{12}C$  was determined to be  $221 \pm 5$  MeV/c, corresponding to a mean internal proton momentum of 171 MeV/c, the reconstructed mean value in the present analysis is found to be 156 MeV/c.

While this value is slightly lower than the reference, it is important to consider the specific experimental conditions. The geometric acceptance of CALIFA, particularly in the forward region, was not fully instrumented, which may introduce some distortions in the reconstructed  $\mathbf{p}_{\text{miss}}$  distribution. Nevertheless, the obtained results remain consistent within the expected systematic uncertainties.

Furthermore, the beam energy, assumed to be constant at 400, AMeV, plays a crucial role in transforming the reconstructed proton momenta into the center-of-mass frame of the  $^{12}C$  nucleus. Small variations in the actual beam energy could have a non-negligible

Figure 41: Reconstructed  $\mathbf{p}_{\text{miss}}$  and its components in the  $^{12}\text{C}$  rest frame

impact on the missing momentum reconstruction. Since no precise event-by-event beam energy information was available for this analysis, a constant value of 400 AMeV was used.

Additionally, as shown in Figure 41d, the distribution of the z-component of  $\mathbf{p}_{\text{miss}}$  exhibits a slight asymmetry, with a tail extending toward lower values. Since the z-component is particularly sensitive to deviations in the mean beam energy, this effect further contributes to the shift of the mean  $\mathbf{p}_{\text{miss}}$  value toward lower values. Future studies with improved acceptance corrections and access to event-wise beam energy measurements could further refine the results and enhance the accuracy of the  $\mathbf{p}_{\text{miss}}$  reconstruction.

#### 5.4.2 Correlations between $^{11}B$ Fragment and the reconstructed inner Proton

In Subsection 5.4.1, the momentum of the inner proton,  $\mathbf{p}_{\text{miss}}$ , was reconstructed using data exclusively from the CALIFA calorimeter. As a next step, this reconstructed momentum can be correlated with the momentum of the  $^{11}B$  fragment in the rest frame of the  $^{12}C$  nucleus.

Since the total momentum in the rest frame must be zero by definition, the momentum vectors of the inner proton and the  $^{11}B$  fragment should be directed oppositely. Consequently, the cosine of the angle  $\gamma$  between these two constituents should be approximately  $-1$ , which is confirmed by the experimental data, as shown in Figure 42a.

Furthermore, Figures 42b and 42c illustrate the correlation between the x- and y-components of  $\mathbf{p}_{\text{miss}}$  and the corresponding components of the  $^{11}B$  fragment. A strong anti-correlation is observed in both cases. While the correlation in the y-component is relatively sharp, the x-component exhibits a more blurred distribution.

This effect arises from the geometry-dependent resolution of the sub-detectors:

- For the x-component, it is important to consider that only the lateral halves of CALIFA were instrumented in the *iPhos* region ( $\varphi_{1/2}$  within  $\pm 45^\circ$  and  $157.5^\circ$  to  $202.5^\circ$ ). The azimuthal resolution is moderate ( $\approx \frac{6^\circ}{\sqrt{12}}$ ), and since the x-component is reconstructed as  $\propto \cos(\varphi)$ , the derivative  $\sin(\varphi)$  remains small for  $\varphi \approx 0$ , leading to lower sensitivity in this region.
- The x-component of the  $^{11}B$  fragment is reconstructed from position measurements immediately after the target, where the lever arm for momentum recon-

struction is relatively short.

- In contrast, the y-component of the  $^{11}B$  fragment is determined from its position in MWPC3 after GLAD, where the larger lever arm improves resolution. Moreover, the y-component remains largely unaffected by the GLAD magnet, further enhancing its reconstruction accuracy.

TODO:->Maybe also correlations between fragment and proton pair, see Chulkov.

#### 5.4.3 Proton Separation Energy $S_p$

The proton separation energy  $S_p$  of  $^{12}C$  from the reaction channel  $^{12}C(p, 2p)^{11}B$  is defined by the masses and energies of the initial and final state particles in the  $^{12}C$  rest frame. One can write the full energy conservation in the rest frame of  $^{12}C$ :

$$M_{^{12}C} + \gamma \cdot m_p = E_1^* + E_2^* + (M_{^{11}B} + E_{ex}) + T_{^{11}B^*} \quad (42)$$

where  $E_1^*$  and  $E_2^*$  are total energies of the two protons in the  $^{12}C$  rest frame,  $E_{ex}$  is residual excitation in  $^{11}B$  and  $T_{^{11}B^*}$  the kinetic energy of the  $^{11}B$  in the  $^{12}C$  rest frame. Using this equation, one can express the total binding energy  $B$  of the knocked out nucleon:

$$B = S_p - E_{ex} = M_{^{12}C} - M_{^{11}B} - E_{ex} - m_p = E_1^* + E_2^* + T_{^{11}B^*} - \gamma \cdot m_p - m_p \quad (43)$$

Using Lorentz transformation from lab to  $^{12}C$  rest frame one can obtain for  $E_1^*/E_2^*$ :

$$E_{1/2}^* = \gamma \cdot m_p + \gamma \cdot T_{1/2} - \beta \cdot \gamma \cdot p_{1/2} \cdot \cos(\theta_{1/2})$$

The kinetic energy of the  $^{11}B$  in the  $^{12}C$  rest frame can be written as:

$$T_{^{11}B^*} = \frac{p_i^2}{2 \cdot M_{^{11}B}}$$

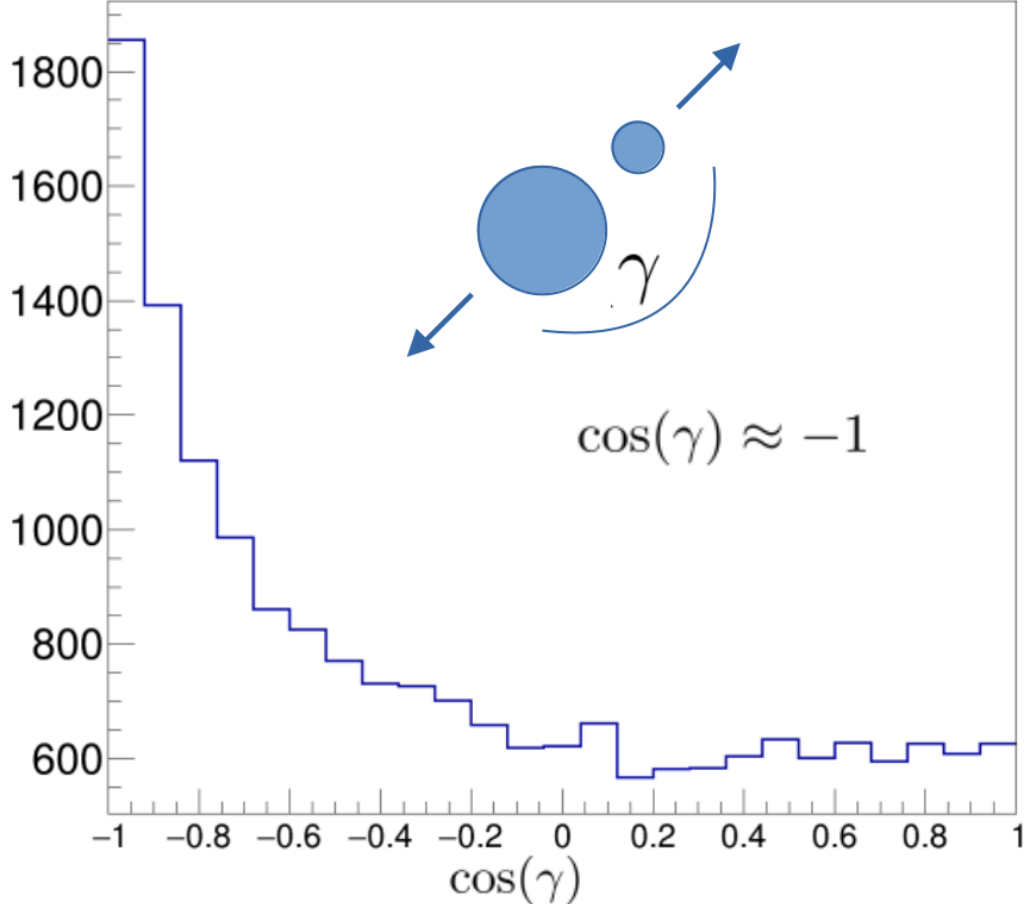
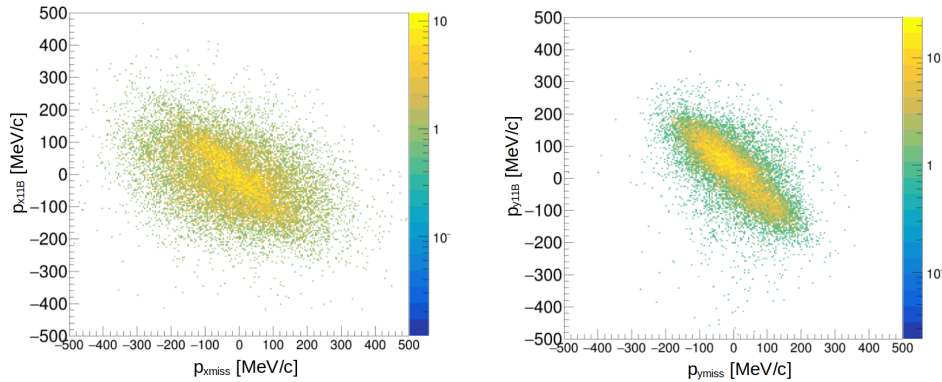
with  $p_i$  the inner momentum of the proton knocked out of the  $^{12}C$  projectile, see equation 8. Putting this in the previous equation one finally gets for the binding energy  $B$ :

$$B = (\gamma - 1) \cdot m_p + \gamma \cdot (T_1 + T_2) - \beta \cdot \gamma \cdot (p_1 * \cos(\theta_1) + p_2 * \cos(\theta_2)) + T_{^{11}B} \quad (44)$$

For  $E_{ex} = 0$ , i.e. the fragment  $^{11}B$  in the ground state, the binding energy  $B$  is equal to the one proton separation energy  $S_p$ <sup>40</sup>.

---

<sup>40</sup>Since the  $^{11}B$  fragment predominantly remains in its ground state—implying that, in most cases, the outermost protons are removed—the binding energy  $B$  and the proton separation energy  $S_p$  are used interchangeably, also due to the limited energy resolution.

(a) Cosine of the angle  $\gamma$  between inner proton and  $^{11}B$ .(b) x-component correlation between inner proton and  $^{11}B$ .(c) y-component correlation between inner proton and  $^{11}B$ .Figure 42: Correlation plots between inner proton and  $^{11}B$  in the  $^{12}C$  rest frame.

As for the S444 experiment no target detector tracking system was available. Consequently the energies as well as the azimuthal ( $\varphi$ ) and polar( $\theta$ ) angles of the two correlated protons had to be fully reconstructed using the CALIFA calorimeter. The calorimeter

provided an energy resolution  $\frac{\Delta E}{E}(@100\text{MeV}) \lesssim 1\%$ , along with angular resolutions of approximately  $\Delta\varphi \approx \frac{6^\circ}{\sqrt{12}}$ , and  $\Delta\theta \approx \frac{2^\circ}{\sqrt{12}}$ . The best way to visualize the separation energy  $S_p$  is to plot it against the summed energy of the two protons in the  $^{12}\text{C}$  rest frame as shown in figure 43. Two vertical lines are visible. They correspond to the two QFS-reaction types within the  $\text{CH}_2$  target: the proton within the  $^{12}\text{C}$  projectile can either scatter on the hydrogen (proton-like) part or on the carbon part of the plastic target. For the first case only the separation energy  $S_p$  as derived in equation 5.4.3 is necessary to remove the proton of the projectile within the  $^{12}\text{C}$  nucleus. In the second case the QFS-reaction is between two protons both bound within a carbon nucleus – the projectile carbon and the target carbon part. Therefore more energy is needed to free both protons from their nuclear bond. This corresponds to the left vertical line in figure 43. It should be noted that the reconstructed one-proton separation energy  $S_p$  is shifted with respect to the mean value of  $\approx 16\text{MeV}$ . For a precise measurement the accurate position of the target and the reaction vertex would be needed, as well as a precise measurement of the kinetic energy of the incoming  $^{12}\text{C}$  would be required (for the actual measurements the beam energy value was set to  $400\text{AMeV}$ ).

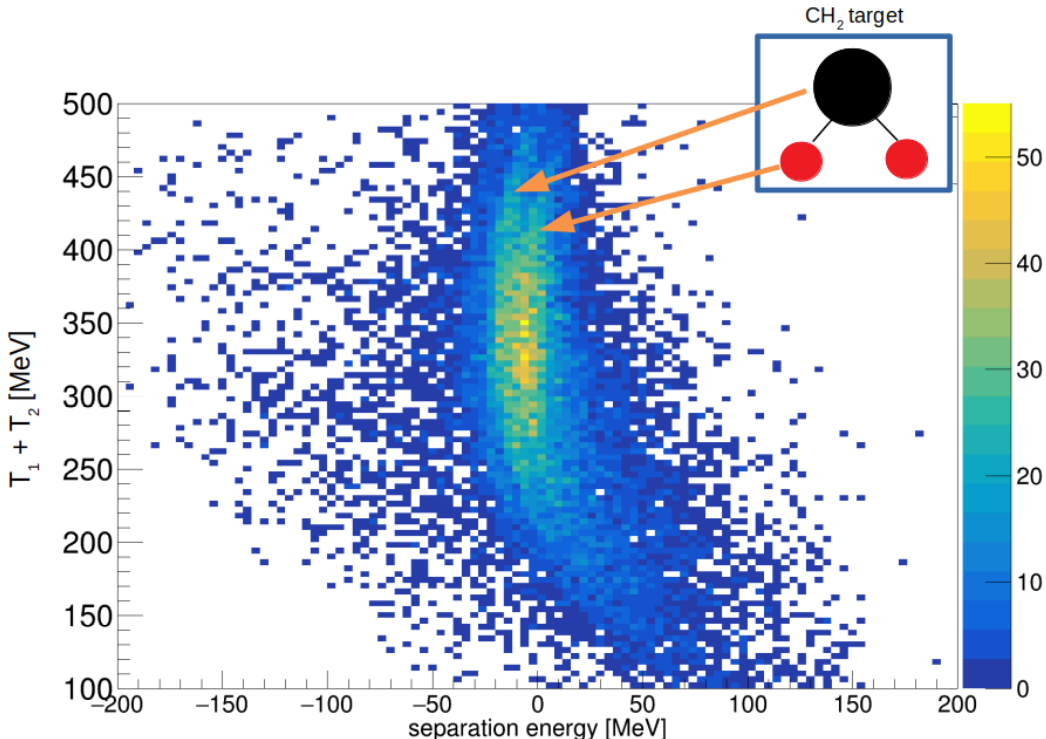


Figure 43: Sum of the kinetic energies of the two correlated protons ( $T_1/T_2$ ) versus the one proton separation energy  $S_p$ . Since this energy is needed to solve the proton from the nucleus' core, its value has conventionally a negative sign.

## 5.5 Reconstruction of excited $^{11}\text{B}$ states

In order to achieve a complete kinematic reconstruction of the reaction products, the use of the CALIFA detector as a  $\gamma$ -ray spectrometer in the low-energy regime (down to  $E_\gamma \geq 100$  keV) is essential. This is particularly relevant for reactions such as  $^{12}\text{C}(p, 2p)^{11}\text{B}$  in quasi-free scattering (QFS) kinematics. In such cases, it is possible to simultaneously identify and measure the energy of the two correlated protons (as demonstrated in previous sections) as well as detect  $\gamma$ -rays emitted during the de-excitation of  $^{11}\text{B}$  from excited states to its ground state ( $3/2^-$ ).

$\gamma$ -ray spectroscopy serves as a sensitive probe for investigating the population of low-lying discrete nuclear states. In the case of exotic nuclei, this allows exploration of previously uncharted excited states. For well-known nuclei such as  $^{11}\text{B}$ , it provides an opportunity to test theoretical shell-model predictions and extract spectroscopic factors with high precision. The established level scheme of  $^{11}\text{B}$  is illustrated in Figure 44.

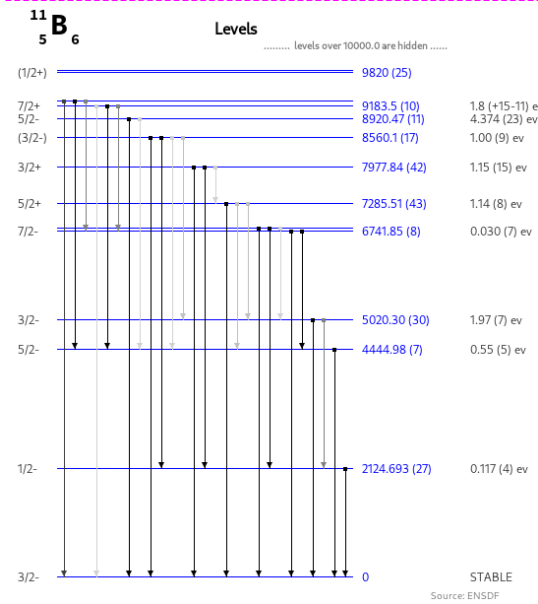


Figure 44: Level scheme of  $^{11}\text{B}$  taken from [68].

Assuming the ground-state proton configuration of  $^{12}\text{C}$  as  $(s_{1/2})^2(p_{3/2})^4$ , the removal of a single proton from the  $p$ -shell is expected to result in a hole state with quantum numbers corresponding to either  $3/2^-$  or  $1/2^-$ . The population of higher angular momentum states is strongly suppressed due to the absence of significant contributions from indirect two-step processes and the limiting influence of ground-state correlations in  $^{12}\text{C}$  [69].

Some excited states of  $^{11}\text{B}$ , such as the  $5/2^-$  state with a known transition energy of 4.4 MeV, are not expected to be populated under QFS conditions. This state arises from the coupling of angular momenta of multiple unpaired nucleons (e.g., two nucleons

in the  $p_{3/2}$  orbital coupled to  $J_{12} = 2$ , and a third nucleon in  $p_{1/2}$  with  $J_3 = 1/2$ ). The population of such states via a QFS reaction would contradict the fundamental mechanism of QFS, which involves the interaction of the probe (typically a proton) with a single nucleon, while the remaining  $A - 1$  nucleons act as spectators.

As the  $^{11}\text{B}$  fragments produced in the reaction carry nearly the full beam energy and move predominantly in the forward direction, the emitted  $\gamma$ -rays from their de-excitation experience relativistic Doppler shifts. Therefore, Doppler correction must be applied to the measured  $\gamma$ -ray energies. Following standard textbooks (e.g., [70]), the relation between the observed  $\gamma$ -ray energy in the laboratory frame and the rest-frame energy of the emitting nucleus is given by:

$$E_\gamma = E_0 \cdot \gamma \cdot (1 - \beta \cos \theta) \quad (45)$$

where  $E_0$  is the intrinsic  $\gamma$ -ray energy in the rest frame of  $^{11}\text{B}$  (approximately the same as the rest frame of the incoming  $^{12}\text{C}$ ),  $\gamma = 1/\sqrt{1 - \beta^2}$  is the Lorentz factor,  $\beta = v/c$  is the velocity of the  $^{11}\text{B}$  fragment normalized to the speed of light, and  $\theta$  is the polar angle of the emitted  $\gamma$ -ray with respect to the beam axis in the laboratory frame<sup>41</sup>.

The high granularity of the CALIFA calorimeter enables a precise determination of the emission angle  $\theta$  of detected  $\gamma$ -rays. For each  $\gamma$ -ray event, the angle  $\theta$  is defined by the position of the individual crystal within the  $\gamma$ -cluster that recorded the maximum deposited energy. This crystal is assumed to represent the most probable direction of the primary  $\gamma$ -ray emission. The angle is then used—relative to the known target position—to perform the Doppler correction and reconstruct the rest-frame  $\gamma$ -ray energy  $E_0$ , according to the relativistic transformation described in Eq. (45). The resulting Doppler-corrected  $\gamma$ -ray spectrum is presented in Figure 45, which was obtained after applying the following reaction selection criteria:

- Identification of the  $^{11}\text{B}$  fragment via time-of-flight measurements between the START detector and the TOFW (Sofia), as detailed in Section 5.3.
- Detection of two high-energy hits corresponding to protons, each with an energy deposition  $E_{\text{hit}} > 30 \text{ MeV}$ .

In Figure 45, both peaks associated with the de-excitation of the  $^{11}\text{B}$  nucleus from the  $1/2^-$  and  $3/2^-$  excited states are visible. From the fit to the  $1/2^-$  peak, an energy resolution of approximately  $0.24 \text{ MeV}$  (FWHM) is extracted.

---

<sup>41</sup>Since the excited state  $1/2^-$  of  $^{11}\text{B}$  has a lifetime  $T_{1/2} = 3.8\text{fs}$  (which corresponds to a width of  $\Gamma = 0.117\text{eV}$ , see level scheme in Fig. 44) it is an immediate transition already occurring in the target region.

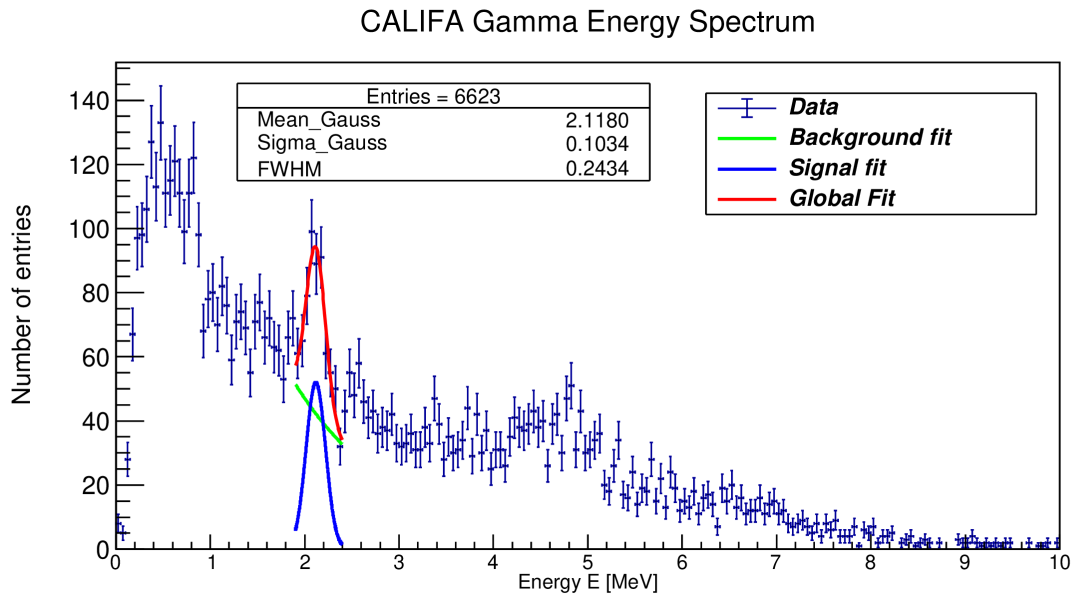


Figure 45: Doppler-corrected  $\gamma$ -ray spectrum in coincidence with the  $^{12}\text{C}(p, 2p)^{11}\text{B}$  quasi-free scattering reaction. The prominent peak at  $E_\gamma \approx 2.1$  MeV corresponds to the de-excitation of the  $^{11}\text{B}$  nucleus from its first excited state ( $1/2^-$ ) to the ground state. This peak is fitted with a Gaussian function (blue), while the underlying background is described by an exponential distribution (green). A broader and less well-defined structure is observed at  $E_\gamma \approx 5$  MeV, associated with the de-excitation of the  $3/2^-$  state.

According to the detector specifications, the expected crystal-wise relative energy resolution is given by  $\Delta E/E = \frac{6\%}{\sqrt{E/\text{MeV}}}$ , which for a 2.1 MeV  $\gamma$ -ray corresponds to an ideal resolution of about 0.09 MeV (FWHM). The observed deviation from this expected value is non-negligible and can be attributed to several experimental and geometrical effects.

First, the Doppler correction relies on the reconstructed polar angle  $\theta$  of the  $\gamma$ -ray, derived from the position of the crystal with the highest energy deposition within the detected cluster. However, this may not correspond to the actual primary interaction point of the photon within the scintillator. This spatial uncertainty becomes increasingly relevant for large opening angles, leading to additional broadening of the reconstructed energy peak.

Second, mechanical factors such as slight tilts or misalignments of the CALIFA detector halves, as well as minor displacements of individual crystals within the carbon alveolar frame, may further contribute to the degradation of energy resolution.

The broader and less well-defined peak at  $E_\gamma \approx 5$  MeV, associated with the  $3/2^-$  state, was not fitted due to its complex structure. This broadening is likely a result of reduced cluster reconstruction efficiency for higher-energy  $\gamma$ -rays. In particular, for photon energies exceeding the pair production threshold ( $E_\gamma > 2m_e c^2 \approx 1.022$  MeV), electron-positron pair production becomes a significant interaction mechanism. Above  $E_\gamma \gtrsim 6$  MeV, it becomes dominant. These interactions can result in spatially separated energy depositions or partial energy loss due to annihilation photons escaping detection. Consequently, this can impair both the accuracy of cluster reconstruction and the effectiveness of Doppler correction, leading to a smeared peak structure.

As anticipated, no enhancement is observed around 4.4 MeV, which would correspond to the population of the  $5/2^-$  state. This is consistent with the quasi-free scattering mechanism, which does not favor the population of such states involving complex multi-nucleon configurations.

It should be emphasized that this experiment represents the first measurement campaign using CALIFA in its final mechanical configuration. The successful reconstruction of Doppler-corrected  $\gamma$ -ray spectra in coincidence with the  $^{12}\text{C}(p, 2p)^{11}\text{B}$  reaction serves as a proof of concept, demonstrating the capability of CALIFA as a key instrument for performing correlated measurements of  $\gamma$ -rays and light charged particles. These results contribute significantly to the overarching goal of achieving full kinematic reconstruction of nuclear reactions under investigation.

## 5.6 Fission via Quasi-Free Scattering reaction

In 2021, the S455 experiment conducted at the R<sup>3</sup>B experiment marked a significant advancement in experimental nuclear physics through the realization of an unprecedented fission study employing quasi-free scattering as a reaction mechanism. This approach induces fission via particle-hole excitations, which can span excitation energies from a few MeV up to several tens of MeV.

Since the discovery of the nuclear fission by O. Hahn and F. Straßmann 1939 [71] and the first interpretations of the underlying process by Lise Meitner and R. O. Frisch [72] and the theoretical approach of Bohr and Wheeler [73] with help of the liquid drop model numerous fission experiments were carried out for better understanding of fission as consequence of a dynamic instability of the considered nucleus.

To induce fission an activation energy  $T_a$  has to be supplied to overcome the Coulomb wall. The final energy released in form of kinetic energy of the fission products  $T_f$  is given by:

$$Q = (m_i - m_f)c^2 = T_f - T_a$$

where  $m_i$  is the initial mass of the fissile nucleus and  $m_f$  the sum of the masses of the fission products. Figure 46 shows the potential curve for the fission process into two fission fragments.

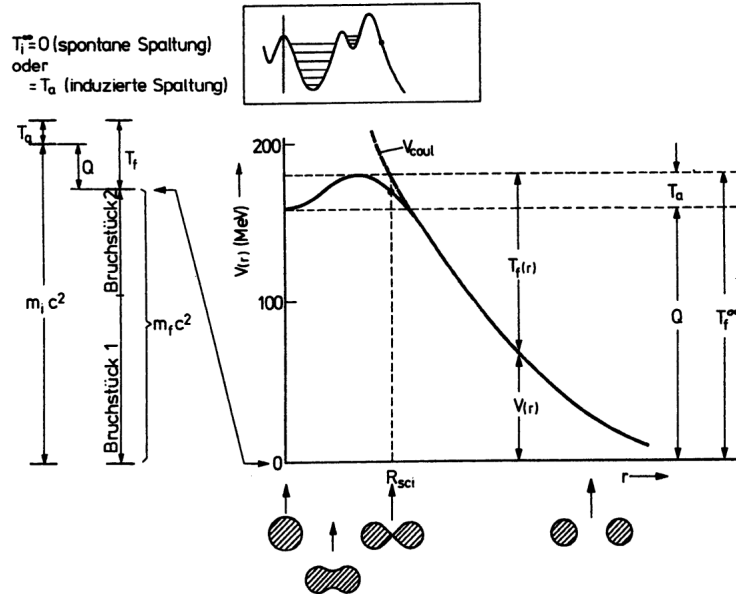


Figure 46: Energy levels and potential profile during fission. *Left:* Energy diagram. *Right:* Potential profile according to the liquid drop model. *Top inset:* Detail of the potential barrier for a more realistic description using the fission hybrid model. The ground state is deformed in this case. Figure taken from [74].

In case of low fission barriers  $T_a$  spontaneous fission(s.f.) may occur. For many other nuclei a higher potential wall is expected where no spontaneous fission is observed. In that case a relatively small energy  $T_a$  needs to be supplied to induce fission. From previous fission experiments fission yields for a large range of exotic nuclei were measured together with the mass/charge distribution of the (two) fission fragments. It has been observed that there are distinct regions of symmetric mass distribution and as well as asymmetric regions which cannot be understood by liquid drop model approximations. Moreover many different processes associated with fission have shown that the fission barrier does not always have a single maximum as predicted by the liquid drop model [75]. It follows that, within the framework of theoretical models, the description must generally combine concepts from both the liquid-drop model and the shell model giving high importance to the fine structure of the topography of the potential-energy surface (PES) as shown in Figure 48, implemented in scission models which focuses on the specific configuration of the fissioning nucleus just before it splits into fragments, considering factors like potential energy and shell effects [76, 77, 78].

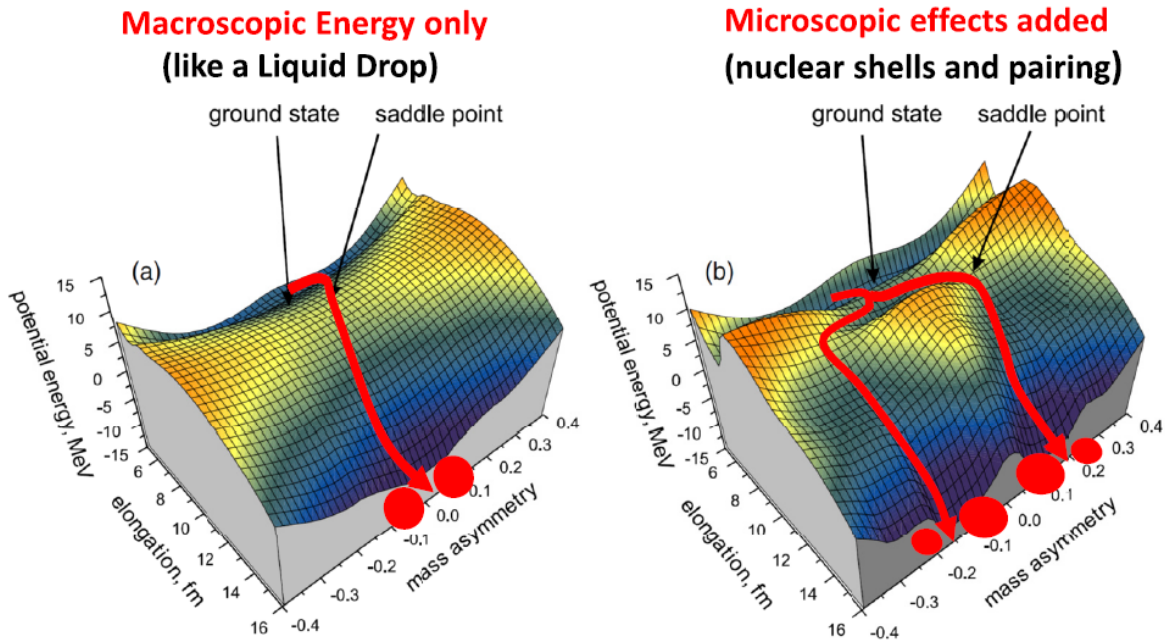


Figure 47: Most probable fission paths (red arrows) in the a) liquid drop model which postulates symmetric fission fragment masses. b) includes shell effects introducing asymmetry in the fragment's mass distribution. Figure from [79].

However, when microscopic effects – such as nuclear shell corrections and pairing interactions – are taken into account, the PES becomes substantially more complex and requires higher-resolution experimental techniques for validation.

To test these more nuanced theoretical predictions, a detailed and differential mapping of the PES is necessary. Fission induced via QFS reactions offers a promising experimental approach for this purpose. In QFS-induced fission, the projectile interacts with an individual nucleon within the target nucleus, leading to localized and controlled excitation of the residual system. This allows for event-by-event measurement of the fission process, enabling a direct correlation between the excitation energy and the resulting fission fragment charge and mass distributions, as well as the fission probabilities.

Such differential data facilitate a more precise determination of the temperature dependence of the fission process and the underlying fission barrier heights for exotic, neutron-rich heavy nuclei. By systematically analyzing these correlations, QFS-induced fission can provide critical constraints on theoretical models of the PES and improve our understanding of fission dynamics far from stability.

In the S455 experiment, as proof of principle, for fission via quasi-free scattering the reaction  $^{238}U(p,2pf)$  was analyzed, with an intermediate excited nucleus Protactinium ( $\text{Pa}^*$ ) which undergoes fission. An overview of the reaction mechanism is shown in Figure 48.

The realization of the proposed experiment required a finely tuned setup was needed

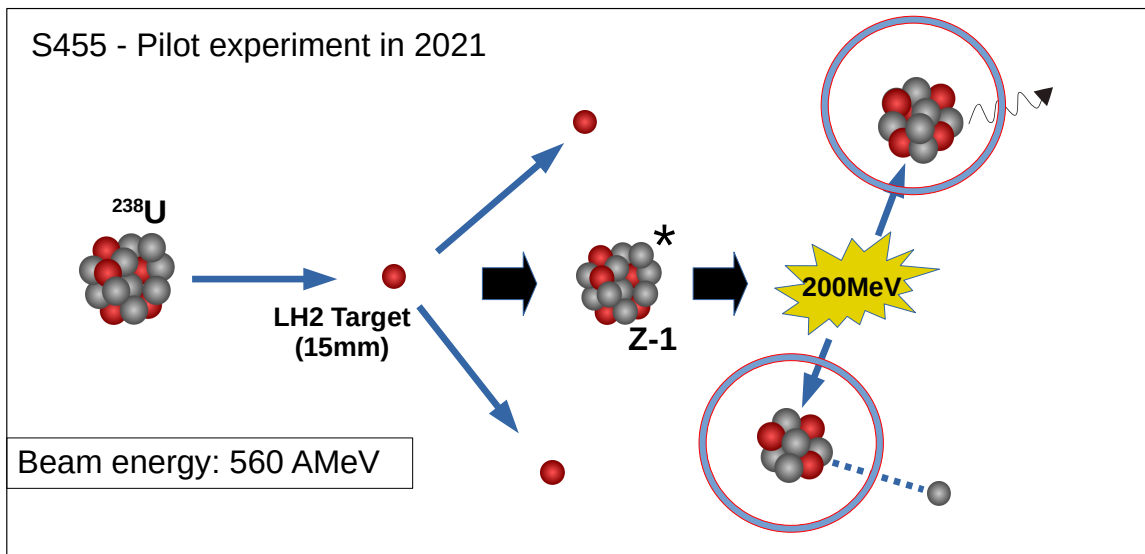


Figure 48: Overview of reaction mechanism  $^{238}U(p,2pf)$  in inverse kinematics.

for a complete identification of the fission fragments and the determination of the neutrons emitted in coincidence. Moreover a precise measurement of the momentum of the knockout protons was required for a full characterization of the fissioning process.

Central detector for the simultaneous charge measurement of the fission fragments is the

TWIN MUSIC thanks to its four-section geometry (for more details see: Section 3.3.2). The final energy/charge calibration employs many fine-tuning steps to retrieve the final charges of the two fission products, as shown in Fig. 49.

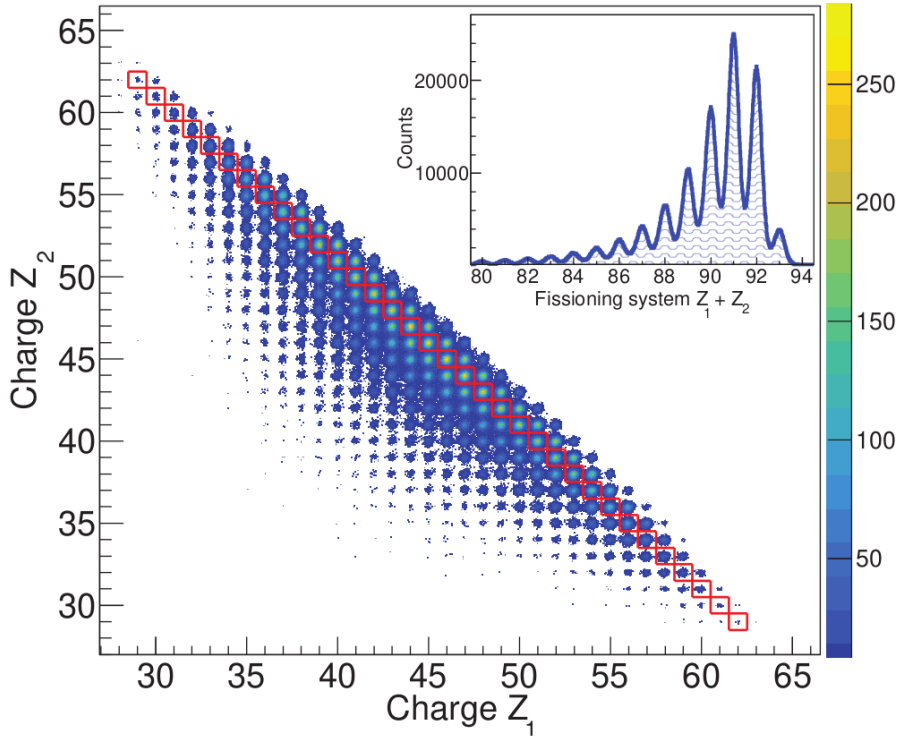


Figure 49: Charge distribution of the charges  $Z_1$  and  $Z_2$  of both fission fragments for all fissioning systems. The inset shows the fissioning system distribution. The red diagonal frame shows the charge distribution when selecting the fissioning system  $Z_1 + Z_2 = 91$ . Figure taken from [45].

The key detector for the identification of the quasi-free scattering part of the reaction was the CALIFA calorimeter. For this experiment the CALIFA DAQ was operated for the first time in multi-event readout mode since high CALIFA event rates were expected and from the experience from the S444 experiment, where CALIFA was operated in a fully self triggered mode, which slowed down the event-building rate and capabilities of the full R3B DAQ<sup>42</sup>.

However, for offline analysis this configuration posed several data unwrapping steps to correctly assign the hits within the asynchronous multi-event readout blocks to the according recorded events.

After successful assignment of the CALIFA detector data, it was possible to extract both the energy and angular information of the two correlated protons emitted in the  $^{238}\text{U}(p, 2pf)$  reaction. A significant observation is that the opening angle between the

<sup>42</sup>For more details about the CALIFA DAQ readout modes see [56], Section 5.2

two protons – an observable directly related to the excitation energy available for fission – shows a strong correlation with the charge distribution of the resulting fission fragments, as illustrated in Fig. 50. Specifically, events characterized by large proton

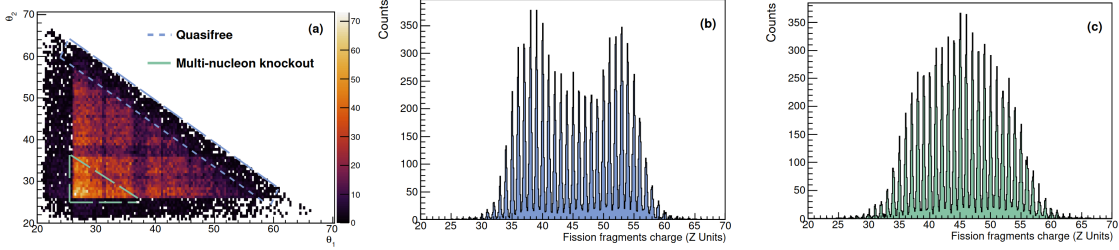


Figure 50: (a) Polar angle correlation between the two protons emitted in fission events following quasi-free scattering (QFS) conditions. Panel (b) shows the resulting fission fragment charge distribution for quasi-free ( $p, 2p$ ) events, selected from the blue-framed angular correlation region in (a). Panel (c) displays the charge distribution corresponding to multi-nucleon knockout reactions dominated by final-state interactions (FSI), selected from the green-framed region in (a). Adapted from Ref. [80], based on data from the S455 experiment conducted in 2021 at the  $R^3B$  setup, GSI.

opening angles, corresponding to low excitation energies (quasi-free scattering conditions), lead to more asymmetric fission fragment charge distributions (see Fig. 50b). Conversely, selecting events with smaller proton opening angles – typically associated with multi-nucleon interactions within the nucleus or knockout of deeply bound nucleons, and thus higher excitation energies – results in a more symmetric charge distribution (see Fig. 50c).

These first promising results, as reported in Refs. [80, 45], demonstrate the feasibility to scan finely the potential-energy surface to provide new insights into the dynamics of nuclear fission.

The second part of the S455 experimental campaign employed a complementary and well-established method to investigate the fission process and its evolution: fission induced by Coulomb excitation (coulex-induced fission). This approach aimed at a precise characterization of fission yields and properties of 100 different neutron-deficient exotic isotopes, ranging from iridium ( $Z = 77$ ) to thorium ( $Z = 90$ ).

These isotopes were produced via the fragmentation of a relativistic 1 AGeV  $^{238}\text{U}$  primary beam and subsequently separated and identified individually using the GSI Fragment Separator (FRS). In the  $\text{R}^3\text{B}$  setup, the isotopes were directed onto a segmented lead target, where they were excited to a few MeV above their ground state energy, inducing the fission into two lighter fragments, which same as for the pilot fission via qfs experiment were identified and tracked within the dedicated  $\text{R}^3\text{B}$  detector setup.

The systematic study of the data collected during ten days of experiment, revealed a transition toward increasingly asymmetric fission in neutron-deficient heavy nuclei. This marks the discovery of a new “island of asymmetric fission” in the nuclear chart, characterized by a surprising dominance of light fission fragments with atomic number  $Z = 36$ , corresponding to krypton, see Fig. 51.

The significance of this discovery was underscored by its publication in **Nature** under the title “*An asymmetric fission island driven by shell effects in light fragments*” [81]. This high-impact publication represents a major milestone for the  $\text{R}^3\text{B}$  collaboration and a notable recognition of the scientific importance of the experiment. This discovery marks a first step toward identifying the extent of a newly observed region in the nuclear chart where asymmetric fission dominates. A series of follow-up experiments is planned at FAIR, which will begin operation in 2027 within the “Early Science” campaign. At the heart of these efforts is the new Superconducting Fragment Separator (Super-FRS) – the successor of the currently operating FRS – a major upgrade that will enable the selection and delivery of even rarer and more exotic isotopes. These advancements will be key to mapping this phenomenon in much greater detail and revealing fundamental aspects of nuclear matter under extreme conditions.

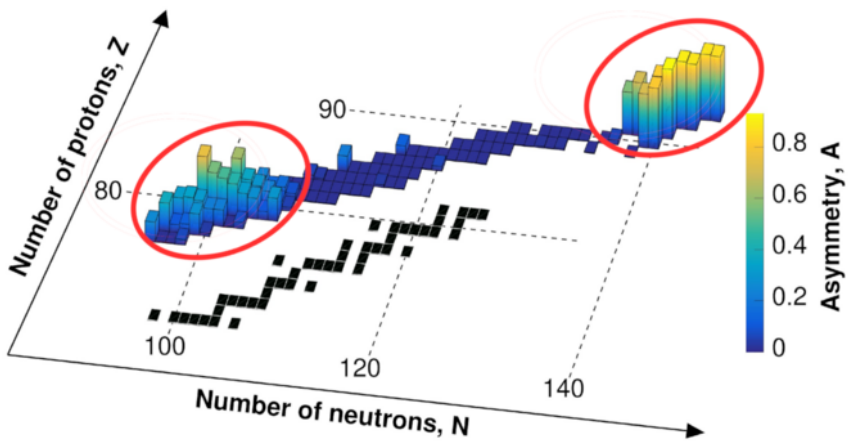


Figure 51: Three-dimensional chart of nuclides illustrating the evolution of asymmetric fission, with asymmetry  $A$  shown as a color scale. The red circles indicate two distinct regions-so-called “islands”-of asymmetric fission. The region in the upper right corresponds to the well-established asymmetric fission in the actinide range (atomic numbers  $Z = 89\text{--}103$ ), where the process is stabilized by the formation of a heavy fragment near xenon ( $Z = 54$ ). In contrast, the region in the lower left highlights the recently discovered asymmetric fission of lighter nuclei around mercury ( $Z = 80$ ), stabilized by the formation of a light fragment near krypton ( $Z = 36$ ). Black squares denote the valley of beta-stable isotopes. *Image credit: Pierre Morfouace, CEA, DAM, DIF, Arpajon, France.*

## 6 Machine Learning for the Cluster Reconstruction in the CALIFA Calorimeter at R<sup>3</sup>B

This study on improving cluster reconstruction in CALIFA using machine learning techniques was initiated in the context of data analysis for the S455 experiment, “*Fission via Quasi-Free Scattering Reaction:  $^{238}\text{U}(p, 2p)X$* ” (see Section 5.6). The R<sup>3</sup>B setup is designed to enable complete kinematic reconstruction of nuclear reactions. In the case of quasi-free scattering (QFS)-induced fission, as studied in S455, this implies that, in addition to reconstructing both heavy and light fission fragments via the dedicated SOFIA setup and detecting neutrons with the large-area NeuLAND detector, it is also possible to identify the two correlated protons from the QFS process. Furthermore, CALIFA can be used to detect the gamma rays emitted during the de-excitation of the fission fragments.

This capability enables precise measurements of the evolution of fission probabilities as a function of excitation energy  $E^*$ , as well as the determination of fission barrier heights. These observables are particularly relevant for the study of short-lived, exotic nuclei, for which experimental data are scarce.

The S455 experiment, performed with a stable  $^{238}\text{U}$  beam, served as a pilot study and proof of principle for this novel experimental approach. A key objective was to tag specific isotopes and analyze the associated gamma-ray spectra measured with CALIFA. For light actinides such as uranium, fission is predominantly characterized by asymmetric mass splitting, a consequence of shell effects [82], which results in a strong population of tin isotopes ( $Z = 50$ ). These isotopes are of particular interest for gamma spectroscopy due to their well-known structure and high-lying excited states. Accordingly, a selection on  $Z = 50$  fragments was applied, accounting for sufficient production cross-section with the presence of prominent gamma transitions. Notably,  $^{132}\text{Sn}$  exhibits a  $2^+$  state at 4.041 MeV [83], well above CALIFA’s gamma detection threshold of approximately 200 keV, and should therefore be clearly identifiable.

Initial attempts to reconstruct gamma spectra via Doppler correction for  $Z = 50$  fragments, however, yielded unsatisfactory results. The resulting spectra displayed broad distributions with no discernible peaks. Several factors contribute to the difficulty of accurate gamma energy reconstruction in this context, amongst others:

**High Background from Delta Electrons:** In heavy-ion fission experiments, numerous delta electrons are generated due to interactions between the beam particles and atomic electrons in the target and surrounding materials. These electrons create a significant number of spurious hits in CALIFA, which interfere with gamma cluster reconstruction and degrade the energy resolution.

**High-Energy Gamma Emission:** The de-excitation gamma rays from fission fragments often possess very high energies, especially in the laboratory frame at beam energies of 540 AMeV, where  $E_{\text{lab}} > 10$  MeV. This is well above the pair production threshold (1.022 MeV), making pair production the dominant interaction mechanism. Consequently, gamma-ray interactions lead to more widely distributed and sparse detector hits, further complicating the clustering and energy reconstruction process.

These challenges, along with the difficulty in extracting meaningful gamma spectra, motivated a collaboration with the *Origins Data Science Lab (ODSL)* to explore advanced machine learning techniques for improving gamma cluster reconstruction in CALIFA.

This section is structured as follows:

First, the specific challenges associated with clustering in relativistic gamma spectroscopy are discussed. Subsequently, the standard clustering model implemented in the R3BRoot framework—used for both online and offline analysis of experimental data within the R3B setup—is reviewed.

Next, the simulation framework and settings used for evaluating and comparing the performance of different clustering algorithms are introduced, along with the performance metrics used.

The agglomerative clustering model, an unsupervised learning approach that incorporates hit time information in CALIFA, is then presented.

This is followed by a description of the Edge Detection Neural Network, developed to improve clustering performance, particularly in the presence of complex hit patterns at the edges of clusters.

Finally, the performance of the proposed models is assessed, including a comparison with selected hand-labeled event examples, where the neural network-based model demonstrates superior results.

## 6.1 Gamma Spectroscopy with the Standard R3B Clustering Algorithm

### 6.1.1 Challenges in Relativistic Gamma Spectroscopy

While the detection of light charged particles such as protons typically yields well-localized energy deposits in segmented detector arrays, the detection of gamma rays which emerge from the reaction vertex presents significant challenges. These difficulties primarily arise from the inherently sparse and spatially distributed energy deposits resulting from the interaction mechanisms of photons with the scintillator material (see Fig. 52) [84].

At photon energies below approximately 300 keV, the photoelectric effect dominates

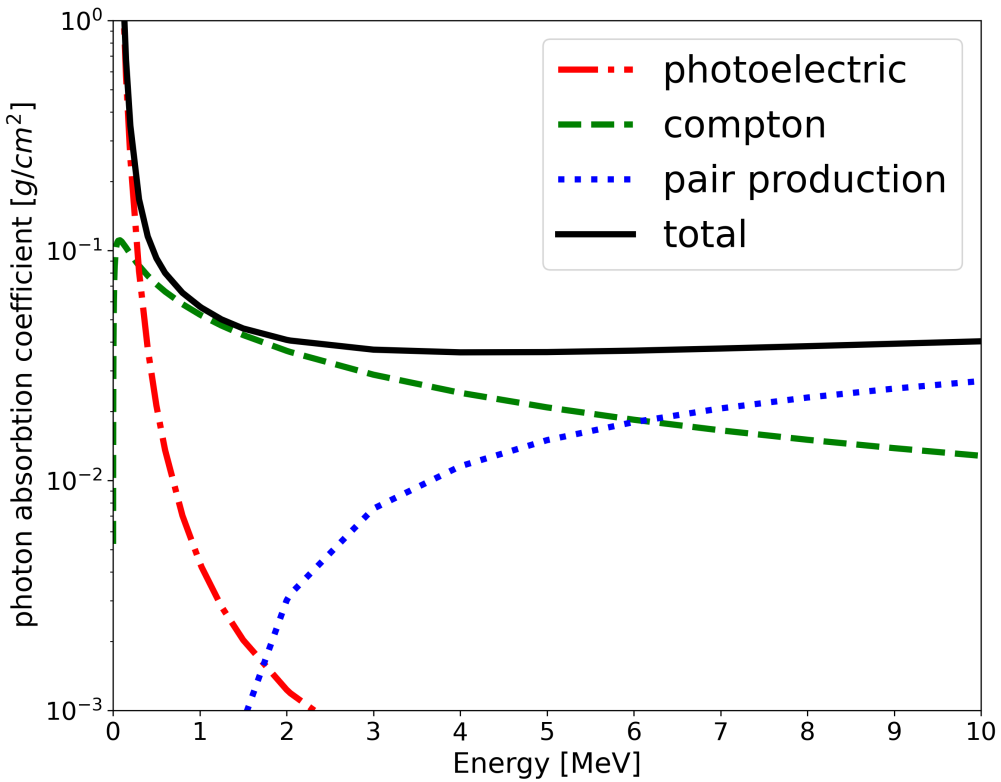


Figure 52: Mass attenuation coefficients for photons in CsI in the range from 100 keV to 10 MeV according to XCOM database [85].

the interaction cross-section. As the photon energy increases, Compton scattering becomes the predominant process. For photon energies exceeding the pair production threshold ( $E_\gamma > 2m_e c^2 \approx 1.022\text{MeV}$ ), electron-positron pair creation becomes possible and is the dominant interaction mechanism above  $E_\gamma \approx 6\text{ MeV}$ .

Compton scattering broadens the clustering by the deflection of the incident gamma ray. According to the KleinâŠNishina formula, the scattering is predominantly forward-focused for moderate to high photon energies [86], leading to clusters in neighboring crystals.

In the case of pair production, which occurs above the  $2m_e c^2$  threshold, the resulting annihilation of the positron yields two 511 keV gamma photons. These secondary photons often escape the initial interaction site, leading to a significant fraction of the incident photonâŽs energy being deposited in multiple detector elements.

For gamma rays emitted by nuclei at rest, this behavior gives rise to well-defined single- and double-escape peaks in the recorded energy spectra – corresponding to the escape of one or both 511 keV photons, respectively – if these photons exit the cluster volume

without interaction.

In experiments involving relativistic ions, such as those conducted at  $R^3B$ , Doppler broadening significantly distorts spectral features, including single- and double-escape peaks[87]. This effect hinders accurate reconstruction of the photon energy and complicates the extraction of absolute gamma-ray yields and reaction cross sections.

### 6.1.2 The Standard R3B Clustering Algorithm

In the standard data acquisition (DAQ) configuration, all CALIFA detector hits occurring within a  $\pm 4\mu s$  time window are grouped into a single event. Each individual hit  $i$  in CALIFA is represented by a data structure containing the following calibrated information, as already introduced in Section 5.4:

- Energy deposit  $E_i$
- Polar angle  $\theta_i$
- Azimuthal angle  $\phi_i$
- Time stamp  $t_i$  (via White Rabbit Precision Time Protocol [88])

In the standard R3B clustering approach, the time information  $t_i$  is not utilized during the spatial reconstruction of clusters.

The initial stage of the clustering algorithm begins by sorting all hits in descending order of energy. A user-defined geometric condition, typically a conical cluster shape with a default aperture of 0.25 rad, is applied. This value has been found to provide an optimal compromise between compact high-energy clusters from light charged particles and more diffuse gamma-ray showers.

The hit with the highest energy defines the seed or center of the first cluster. The algorithm then iterates through the remaining hits and includes each hit in the current cluster if it lies within the specified cone aperture relative to the seed direction. Once the list is fully processed for the current cluster, the next highest-energy unassigned hit becomes the seed of a new cluster. This procedure repeats until no unassigned hits remain. The procedure steps are graphically summarized in Figure 53.

## 6.2 Data Simulation and Selection

### 6.2.1 Simulation Setup

To evaluate and compare the clustering algorithms presented in this work, simulated datasets are employed to assess their performance. For both unsupervised approaches,

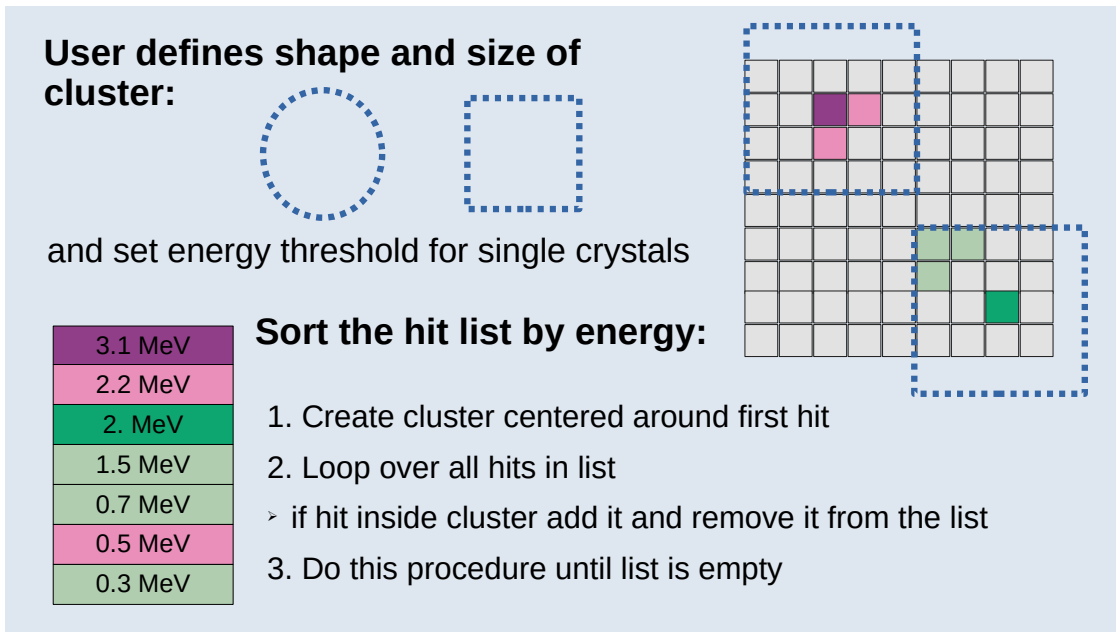


Figure 53: Stepwise graphical representation of the Standard R3B clustering procedure. The cluster shape and size are predefined by the user and remain fixed throughout the clustering process.

such as agglomerative clustering, and supervised machine learning methods, such as the Edge Detection Neural Network, which will both be introduced in detail in the following section, access to ground truth labels is required. For this purpose, the R3BROOT framework [89] with a Geant4-based Monte Carlo [90] backend was employed.

The CALIFA detector geometry used in the simulation corresponds to the configuration implemented in early 2024. At that time, the iPhos region (polar angles  $19^\circ - 43^\circ$ ) was fully instrumented, while only the forward half of the Barrel region ( $43^\circ - 87^\circ$ ) was active. The forward-most CEPA region ( $7^\circ - 19^\circ$ ) was not yet equipped.

Gamma-ray energies were sampled from a uniform distribution between 0.3 MeV and 10 MeV. The interaction of the primary gamma rays with the CsI(Tl) scintillation material was modeled using Geant4 transport physics.

To emulate realistic event topologies, three gamma rays were generated per event, resulting in multiple detector hits. Timing information was coarsely simulated by assigning each primary gamma a random emission time within the  $\pm 4\ \mu\text{s}$  event window. The corresponding hit times were then Gaussian-smeared with a standard deviation of 200 ns to reflect typical electronic channel timing variations.

The resulting dataset was split into training and test subsets, comprising 13,000 and 7,000 events, respectively.

### 6.2.2 Performance Metrics

To quantitatively assess the performance of the clustering algorithms presented in this work, a set of four custom metrics was defined. Three of these are event-based, while an optional fourth metric evaluates clustering quality on a per-cluster basis:

- **True Positive (TP):** All hits in an event are correctly assigned to their respective clusters.
- **False Positive (FP):** At least one hit in an event is incorrectly merged into a cluster it does not belong to.
- **False Negative (FN):** At least one hit is not merged into its true cluster and instead forms a spurious cluster.
- **False Mixed (FM):** An event is classified as false mixed if it contains both FP and FN characteristics—i.e., at least one hit is incorrectly merged, and at least one true cluster is partially reconstructed.

In addition, a cluster-based metric is defined:

- **Well Reconstructed (WR):** The ratio of correctly reconstructed clusters to the total number of true clusters in the dataset.

These metrics allow a comprehensive evaluation of clustering accuracy, robustness, and failure modes. Figure 54 illustrates the definitions of the four event-based metrics in a graphical manner.

Special attention must be given to the false negative rate, which is closely associated with pair creation and subsequent annihilation processes. These processes produce widely spread hits that cannot be merged using the standard R3B clustering method, thereby motivating the development of a multi-layer perceptron architecture to improve clustering performance at the boundaries.

## 6.3 Agglomerative Clustering Model

To incorporate temporal information into the clustering process—unlike the standard R3B algorithm, which omits it—a generic, well-established method was adopted: agglomerative clustering [91] as implemented in the SciPy library [92]. This unsupervised learning algorithm enables flat clustering based on hierarchical linkage with a user-defined threshold.

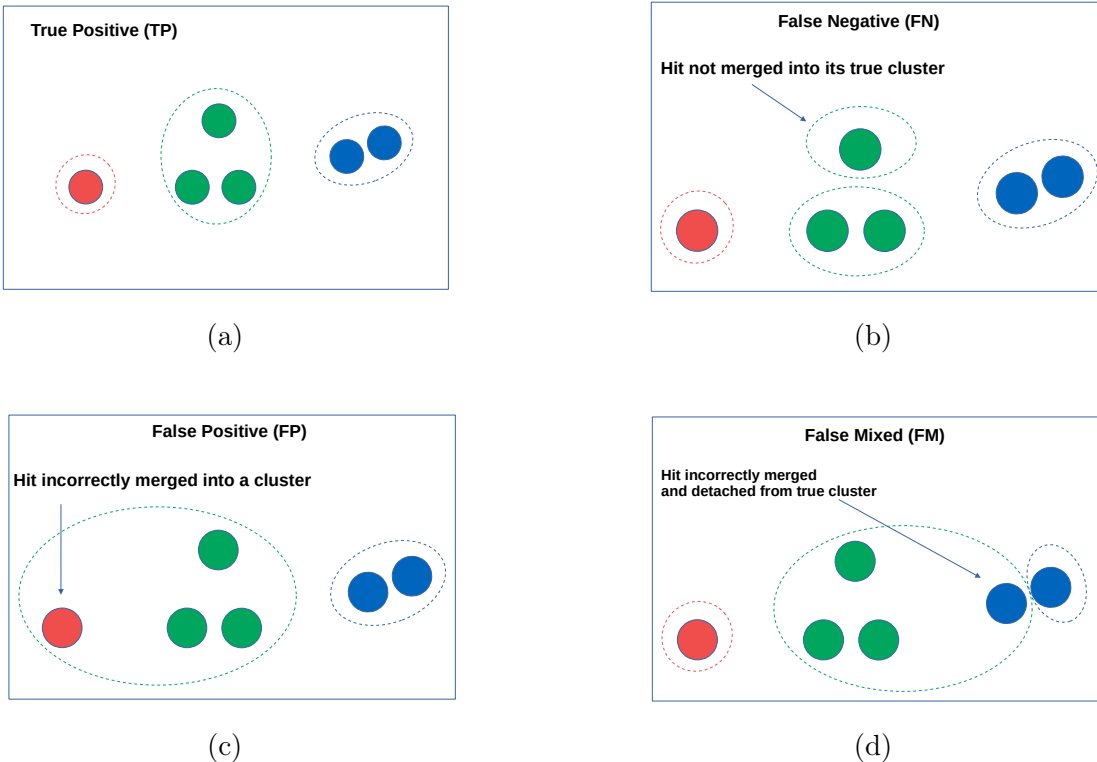


Figure 54: Defined event-based metrics, a) TP, b) FN, c) FP, d) FM

Each hit was mapped into spherical coordinates  $(\theta, \phi, r)$ , where the radial component  $r$  encodes time information. To ensure non-negative radii, the acquisition time window of  $\pm 4\mu\text{s}$  was shifted by  $+4.5\mu\text{s}$ . The Ward linkage criterion [93], which minimizes intra-cluster variance, was employed as the distance metric.

The threshold parameter was optimized to yield the best performance according to the custom-defined *true positive* (TP) and *well reconstructed* (WR) metrics. A comparison between the standard R3B clustering and the agglomerative method is presented in Figure 55. As shown in Figure 55, the agglomerative clustering algorithm demonstrates improved performance both on an event level (true positive rate) and on a cluster level (correctly reconstructed clusters). However, this improvement is accompanied by an increased false negative rate, indicating that the algorithm tends to under-merge hits near the edges of clusters. This limitation motivated the development and application of an edge detection neural network, which is introduced in the following subsection.

## 6.4 Edge Detection Neural Network

To enhance the clustering performance, particularly at the boundaries of hit distributions, a multi-layer perceptron architecture was developed using the Pytorch library [94] to perform pairwise classification of detector hits. This model is applied either to in-

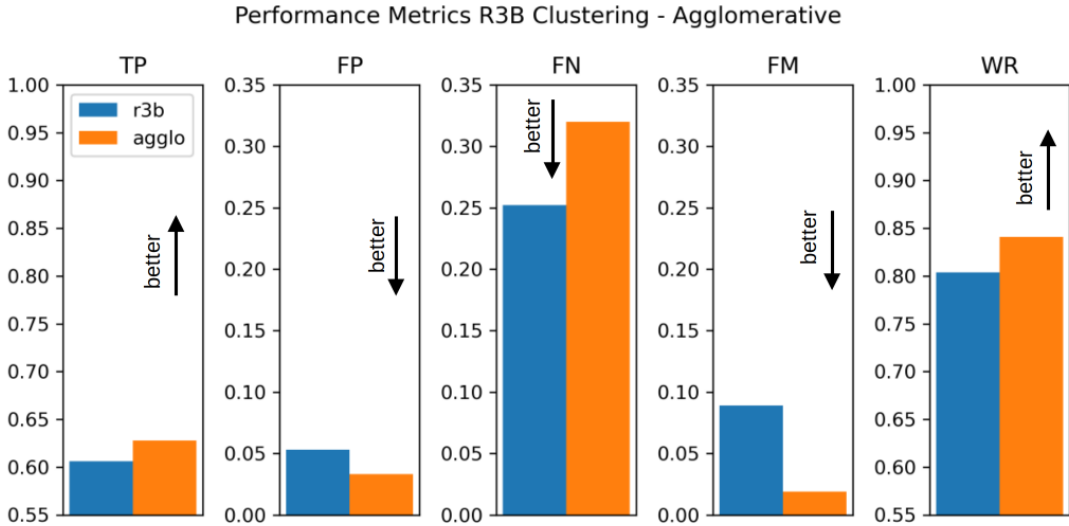


Figure 55: Comparison of clustering performance on the test dataset using standard R3B clustering (blue) and agglomerative clustering (orange) incorporating hit-time information. The dataset comprises simulated  $\gamma$ -rays with energies uniformly distributed between 0.3 and 10 MeV. The metrics shown include event-based and cluster-based measures:  $TP$ ,  $FP$ ,  $FN$ ,  $FM$ , and  $WR$ ; see also Subsection 6.2.2.

dividual raw hits or to hits pre-clustered via agglomerative clustering, on an event-by-event basis.

The model takes 12 input features for each hit pair  $(i, j)$ : absolute values of energy ( $E_i, E_j$ ), polar angle ( $\theta_i, \theta_j$ ), azimuthal angle ( $\phi_i, \phi_j$ ), and time ( $t_i, t_j$ ). Additionally, four differential features are computed:  $\Delta E = |E_i - E_j|$ ,  $\Delta\theta = |\theta_i - \theta_j|$ ,  $\Delta\phi = |\phi_i - \phi_j|$ , and  $\Delta t = |t_i - t_j|$ . These differential inputs are helpful for training stability and convergence with our limited model sizes tested. In particular,  $\Delta\phi$  resolves the discontinuities caused by the periodicity of the azimuthal angle (e.g., distinguishing between  $\phi = 355^\circ$  and  $\phi = 5^\circ$ ), which would otherwise introduce large erroneous differences in angular comparisons.

Of the 12 features, only the hit time is normalized to the  $[0, 1]$  interval; all other values are used in their native physical units. The neural network architecture takes the 12-dimensional input vector and passes it through a fully connected feed-forward network with one hidden layer of  $10^3$  nodes, followed by a ReLU activation. Two additional hidden layers, each with  $10^2$  nodes, are applied sequentially. The output layer consists of a single node with a sigmoid activation, yielding a score in the interval  $[0, 1]$ , where values close to 1 indicate that the hits (or clusters) are likely to originate from the same event cluster.

Training is performed using the binary cross-entropy loss function [95, 96] and stochastic gradient descent (SGD) [97] with a fixed learning rate of  $5 \times 10^{-3}$ . Given the moderate size of the training dataset, full-batch training is employed without mini-batching. The model is trained for  $8 \times 10^4$  epochs. After training, a threshold is applied to the prediction scores to classify hit pairs. This threshold is tuned to optimize the performance across all defined metrics, as described in Subsection 6.2.2. Final clusters are then formed by grouping all connected hit pairs based on the predicted associations.

The edge detection NN was implemented and tested in three configurations:

- **Plain Edge NN:** The model is applied directly to individual hits without any pre-clustering. All clustering is performed based solely on the NN predictions.
- **R3B + Edge NN:** The data are first clustered using the standard R3B clustering algorithm as an initial clean-up step. For each resulting cluster, an energy-weighted center of mass is calculated, replacing individual hits. The NN is then trained exclusively on false negative cases, i.e., events where reconstructed clusters exhibit detached hits. In application, the R3B standard clustering is first applied to the test data, followed by the NN to refine cluster boundaries and reduce the false negative rate as clean-up step.
- **Agglo + Edge NN:** This strategy mirrors the R3B+Edge approach, with the key difference that time information is incorporated. As in the R3B+Edge model, the NN is trained on false negative cases to perform a final clean-up step after pre-clustering the hits using the agglomerative clustering algorithm described in the previous subsection. The significant reduction of the false negative rate achieved by the clean-up step in the Agglo+Edge implementation is demonstrated in Figure 56, which compares the reconstructed energy spectra from simulations of monoenergetic 2.1 MeV gamma events using the R3B standard clustering and the Agglo+Edge method.

## 6.5 Results

The results of this study are summarized in Table 6, organized according to increasing levels of reconstruction complexity. For completeness, the previously obtained results from the comparison between the "baseline" R3B standard clustering algorithm and the agglomerative model are also included.

The agglomerative model shows improved performance over the R3B baseline in terms

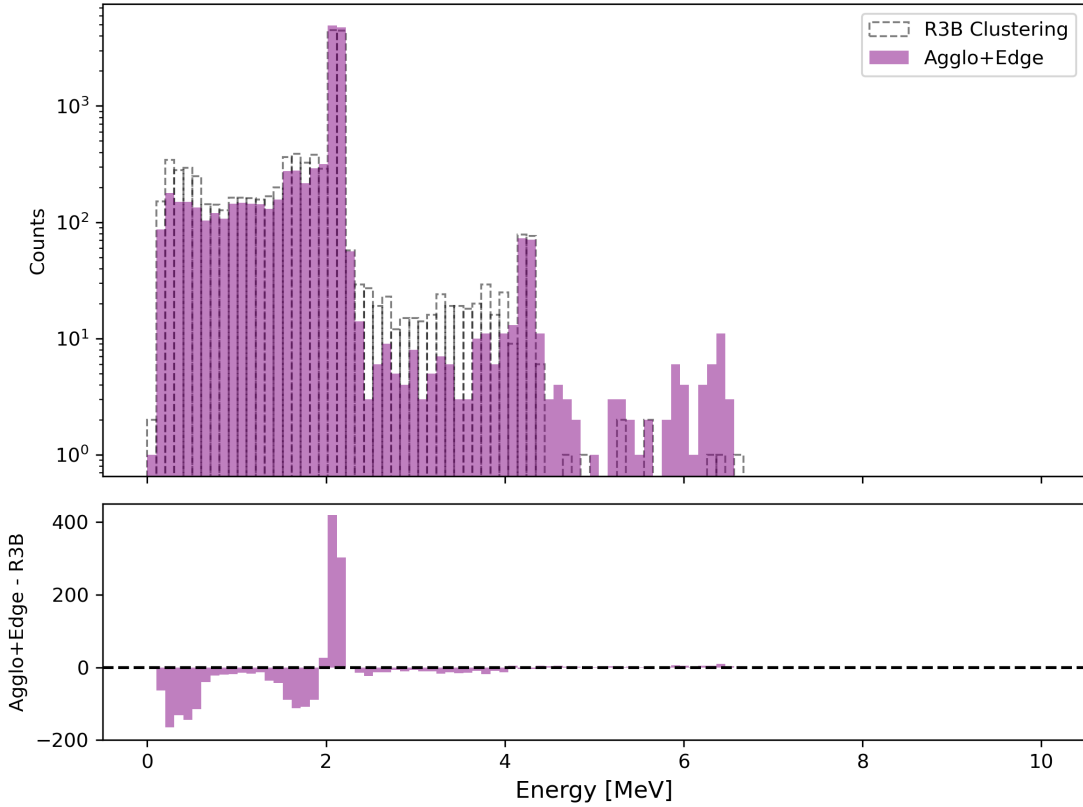


Figure 56: Reconstructed gamma energy spectrum from simulated events, each consisting of three 2.1 MeV gamma photons. The upper panel shows the comparison between the standard R3B clustering and the Aggro+Edge method. The lower panel displays the bin-by-bin count difference between the two approaches. The Aggro+Edge model demonstrates a significant improvement by successfully reattaching escaped hits, notably in cases where sparse energy deposits around 1.6 MeV and 0.5 MeV result from pair production and subsequent annihilation processes of the original gamma photons. This clean-up step leads to a marked reduction in false negatives compared to the standard R3B clustering.

of both event-level true positives (TP) and cluster-level (WR) values. However, it exhibits inferior performance with respect to the false negative (FN) rate, indicating a tendency to miss relevant hits during reconstruction. This limitation motivated the development of an Edge Detection Neural Network, initially evaluated as a standalone clustering algorithm and subsequently integrated into the agglomerative framework, yielding the combined model denoted as *Aggro + Edge*.

The *Aggro + Edge* model demonstrates superior performance across all evaluated metrics, achieving an overall correct reconstruction rate of 81.3%, significantly outperforming the *R3B Standard Clustering* algorithm, which reaches 60.6%.

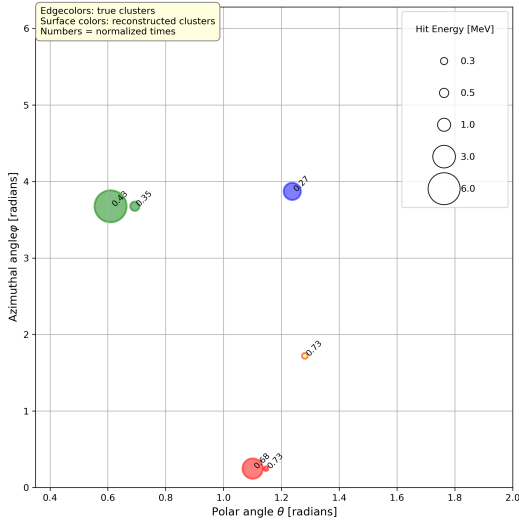
Clustering Model	TP( $\uparrow$ )	FP( $\downarrow$ )	FN( $\downarrow$ )	FM( $\downarrow$ )	WR( $\uparrow$ )
R3B Standard Clustering	60.6	5.3	25.2	8.9	80.4
Agglomerative Clustering	62.8	<b>3.3</b>	32.0	1.9	84.1
Edge Clustering (no time)	$63.4 \pm 0.3$	$7.2 \pm 0.3$	$24.8 \pm 0.7$	$4.6 \pm 0.1$	$82.4 \pm 0.1$
Edge Clustering (with time)	$74.7 \pm 0.5$	$3.4 \pm 0.6$	$20.5 \pm 1.3$	$1.4 \pm 0.1$	$89.2 \pm 0.1$
R3B + Edge (no time)	$67.4 \pm 0.3$	$8.5 \pm 0.3$	$16.0 \pm 0.4$	$8.0 \pm 0.3$	$82.2 \pm 0.1$
Aggro + Edge (with time)	<b><math>81.3 \pm 0.3</math></b>	$5.1 \pm 0.0$	<b><math>12.2 \pm 0.3</math></b>	<b><math>1.5 \pm 0.1</math></b>	<b><math>91.0 \pm 0.1</math></b>

Table 6: Summary of performance metrics as defined in Subsection 6.2.2, evaluated for the different clustering algorithms. The models *R3B Standard Clustering*, *Edge Clustering (no time)*, and *R3B + Edge (no time)* utilize only angular and energy information on a per-hit basis for cluster reconstruction. In contrast, *Agglomerative Clustering*, *Edge Clustering (with time)*, and *Aggro + Edge (with time)* additionally incorporate time-of-hit information into the clustering process. Uncertainties reported for the four edge detection neural network variants correspond to the standard deviation of the results obtained from ten independent training runs.

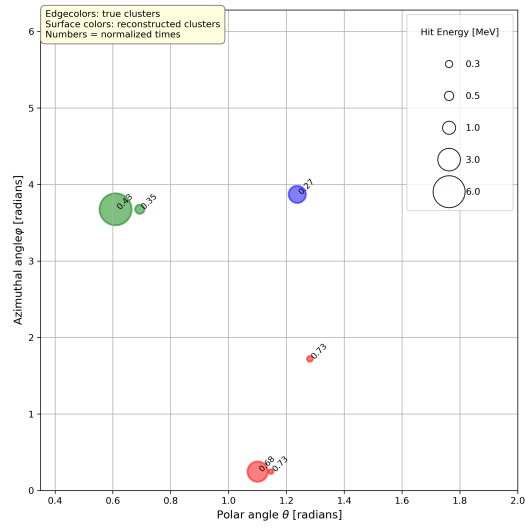
A visual representation of an event, contrasting the incorrectly merged hits from the R3B standard clustering with the correctly reconstructed clustering using the Aggro+Edge model, is shown in Figure 57.

To further explore the capabilities of neural network-based clustering approaches, two additional models were evaluated: a standalone *Edge Detection Neural Network* and a hybrid approach combining *R3B Standard Clustering* with edge-based postprocessing (*R3B + Edge*). Notably, both of these models operate without incorporating time-of-hit information, similar to the R3B baseline. Nonetheless, both outperform the *R3B Standard Clustering*, underscoring the potential of edge-based neural network models for improving cluster reconstruction in high-granularity detector systems.

The edge detection NNs presented here represent a special case of Graph Neural Networks (GNNs) [98], which, along with the more sophisticated transformer models [99, 100], have seen widespread adoption in particle physics over the past five years [101, 102, 103]. Interestingly, for this application, using an unsupervised learning algorithm (agglomerative clustering) to first define a graph structure presented a powerful inductive bias for our application which much improved our results over the standalone edge-NN. One limitation of this approach is that it cannot improve an overly aggressive pre-clustering (e.g., a false positive rate can never be decreased in the clean-up step by the edge-NN). However, the necessity of reattaching edge hits to address the high false negative rate exceeding the false positive rate by a factor of five in the baseline



(a) R3B standard clustering: the red-edged cluster with sparse hits is incorrectly split up into two clusters.



(b) Agglo+Edge clustering: successful reattaching of sparse hits.

Figure 57: Exemplary event with three simulated gamma photons in the energy range of  $0.3 \text{--} 10 \text{ MeV}$ , comparing the reconstruction performance of the R3B standard clustering and the Agglo+Edge method.

reconstruction (see Table 6) motivated this strategy.

Subsequent work could consider also adding a subsequent cluster splitting step in an end-to-end optimizable algorithm.

Although, in principle, transformers could learn the graph structure directly from hit distributions, initial tests showed limited performance, highlighting an opportunity for the community to further develop combined machine learning-based reconstruction methods.

## 6.6 Discussion and Outlook

- maybe add the discussion from the paper-draft
- add the note that it should maybe tried out to use much less nodes, factor 10-100
- mention that these results are in the way to be published in NIM-A

# Appendices

## A Pileup rejection with R3B MUSIC charge cut

As detailed in Section 4.2, a stringent event selection criterion was applied to the incoming ions. This included a precise charge cut, as illustrated in Figure 13. The application of a rigid  $\pm 1\sigma$  charge cut, in conjunction with the requirement of a single hit in the Start detector, effectively suppresses pileup events. The superior pileup rejection capability of the R3B MUSIC detector, owing to its longer shaping time compared to the TWIN MUSIC detector, is further demonstrated in Figure 58. This extended shaping time ensures that any genuine pileup event will be reliably registered by the R3B MUSIC.

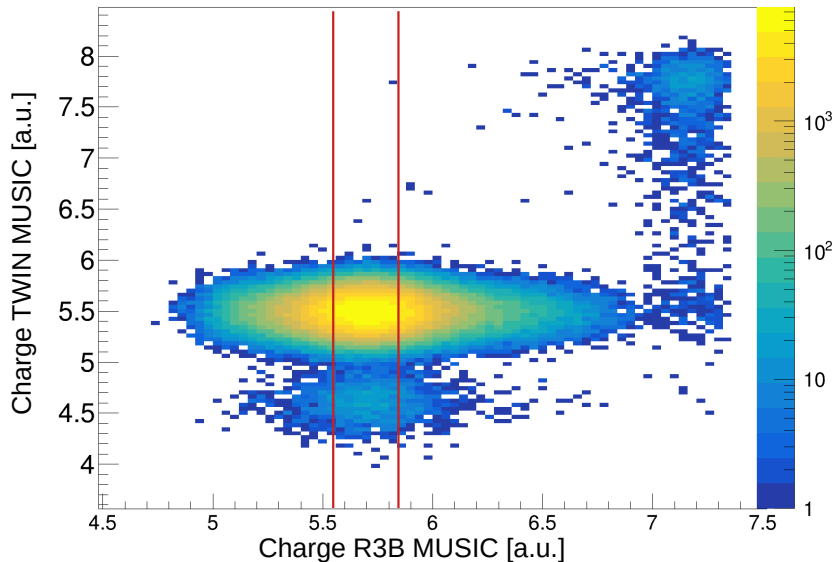


Figure 58: Charge distribution in R3B MUSIC vs TWIN MUSIC. The strict charge cut – only events within the two horizontal lines are selected for the analysis – on R3B MUSIC fully suppresses pileup events. For this plot positional cuts on the MWPC0 and the requirement of a single hit in the Start detector are applied. Target run, 550 AMeV.

## B MWPCs - *cal-to-hit* data processing

For all MWPCs the standard *cal-to-hit* step sorts the calibrated hits in the detector according to the calibrated charge deposited in the pads. The final position (in mm)

is determined by selecting the hit with the highest charge deposition  $Q_{max}$  and its left ( $Q_L$ ) and right neighbor ( $Q_R$ ) pads<sup>43</sup>. These charge and position values are inserted in the "hyperbolic squared secant" function [104] with the following charge distribution function:

$$Q(x) = \frac{a_1}{\cosh^2\left(\frac{\pi(x-a_2)}{a_3}\right)}$$

where  $a_1$  is the amplitude of the distribution  $Q_{max}$ ,  $a_2$  its centroid, and  $a_3$  derives as follows:

$$a_3 = \frac{\pi\omega}{\cosh^{-1}\left(0.5 \times \left(\sqrt{\frac{Q_{max}}{Q_L}} + \sqrt{\frac{Q_{max}}{Q_R}}\right)\right)}$$

$\omega$  being the width of the pads. The centroid of the distribution, which is used as final hit position in the *hit*-data level, can be deduced from:

$$a_2 = \frac{a_3}{\pi} \times \tanh^{-1}\left(\frac{\sqrt{\frac{Q_{max}}{Q_L}} - \sqrt{\frac{Q_{max}}{Q_R}}}{2 \sinh\left(\frac{\pi\omega}{a_3}\right)}\right)$$

Figure 59 shows the "hyperbolic squared secant" function with the inserted values for  $Q_{max}$ ,  $Q_R$  and  $Q_L$ . The "hyperbolic squared secant" function is used to determine

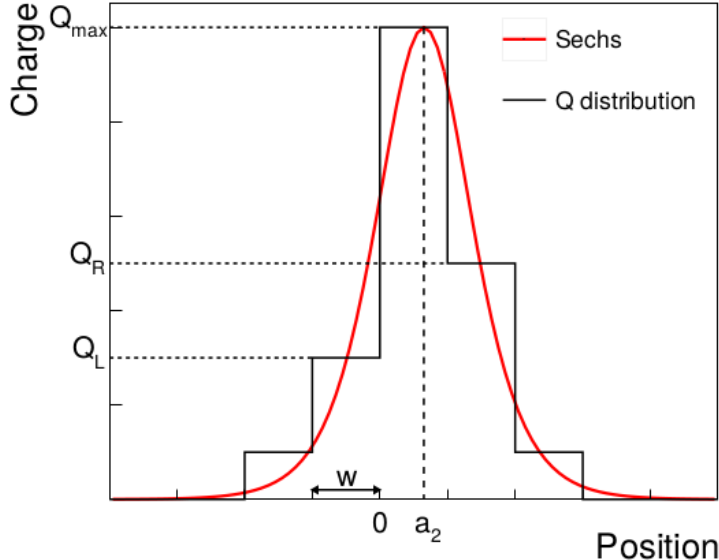


Figure 59: Figure taken from [40], with  $w$  being the width of the cathode pads of the MWPC and  $a_2$  the final position value of the hit determined by the hyperbolic squared secant function (in red). In black the measured charge deposition distribution in the MWPC.

the x hit position as well as the y hit position for all MWPCs. Figure 60 shows the

---

<sup>43</sup>In case no charge deposition in one or both neighbors the charge value is set to 1 respectively.

$x_{mw2}$  versus  $x_{mw3}$  distribution of carbon isotopes for the 400 AMeV run with the thick target. The two correlated lines corresponding to the  $^{12}\text{C}$  and  $^{11}\text{C}$  isotopes can clearly be distinguished. The vertical line can be interpreted as amount of events where the incoming centered carbon fragment gets scattered by air or the detector material in place between MWPC2 and MWPC3. The horizontal wide spread line has no physical interpretation and can rather be explained by the *cal-to-hit* step in MWPC2: For events where there is not a spatially constrained hit cluster but sparse hits the hyperbolic squared secant function may pick the wrong  $Q_{max}$  and therefore wrongly reconstructs the x position in MWPC2.

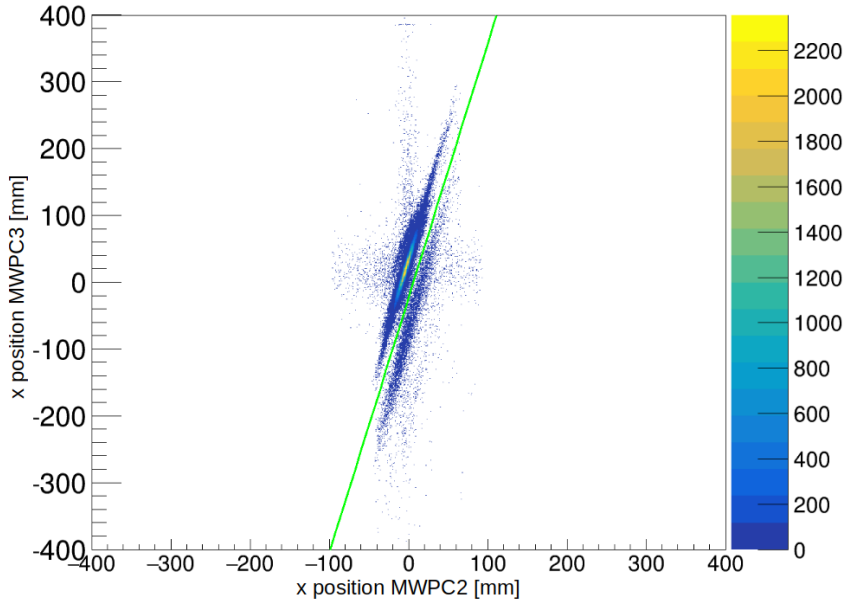


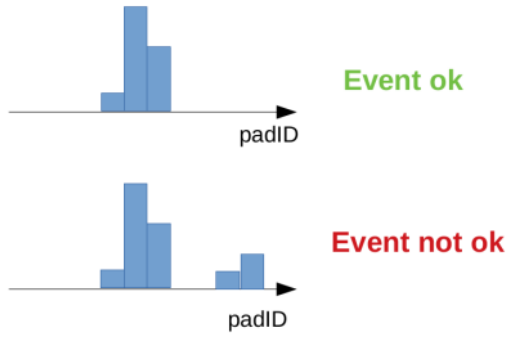
Figure 60: Distribution of x in MWPC2 and MWPC3 for the 400 AMeV run with thick target. The green line acts as reference line for the isotope separation between  $^{12}\text{C}$  and  $^{11}\text{C}/^{10}\text{C}$ .

## B.1 Coherent clustering

To overcome the issue with potentially wrong x- or y-position reconstruction in the MWPCs the event selection can be restricted to events where the MWPCs of interest have only one spatially constrained cluster (see figure 61) to avoid ambiguities in the position determination.

Figure 62 shows the distribution of x in MWPC2 and MWPC3 using the coherent clustering reconstruction. This reconstruction method removes the uncorrelated horizontal line which was observed in figure 60. However the statistics are reduced by

Figure 61: Restricted event selection for MWPC2 and MWPC3: only events with one single coherent (i.e. without any holes) cluster are accepted.



approximately 35%<sup>44</sup>.

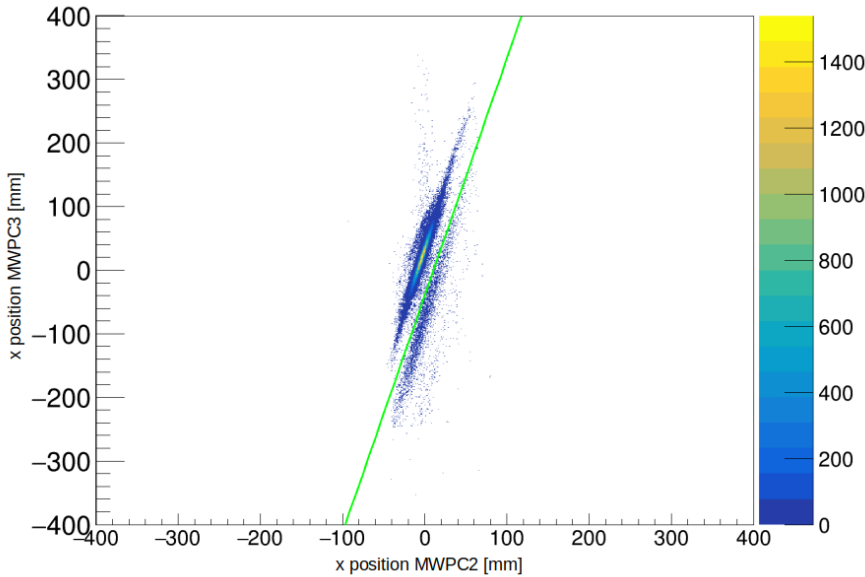


Figure 62: Distribution of  $x$  in MWPC2 and MWPC3 using the coherent clustering reconstruction. Thick target run, beam energy 400 AMeV. The green line acts as reference line for the isotope separation between  $^{12}\text{C}$  and  $^{11}\text{C}/^{10}\text{C}$ .

## C MWPC0 selection cuts

As outlined in Section 4.2, only events with hits in MWPC0 within a  $\pm 1\sigma$  around the beam spot center in both the  $x$  and  $y$  directions were selected, in order to ensure the selection of well-focused incoming particles. The standard *cal-to-hit* procedure was applied to determine the spatial coordinates of the hits.

For completeness, additional strategies were investigated to suppress misreconstructed

---

<sup>44</sup>Number of entries in the 2D plot for default reconstruction method: 533816, for the coherent clustering reconstruction: 346315 for the 400 AMeV run with thick target.

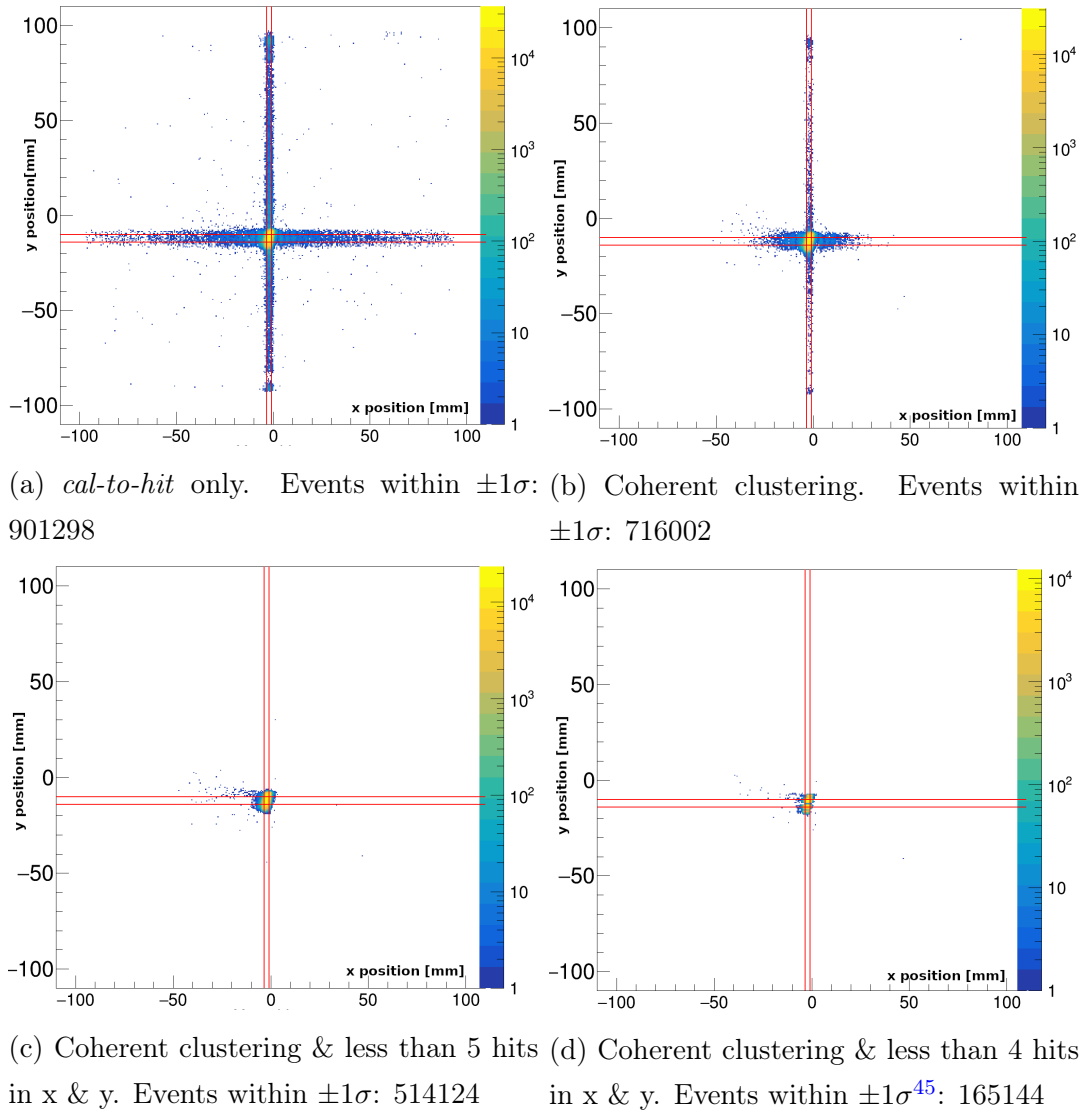


Figure 63: Overview of methods and cuts to clean up x & y distribution on MWPC0 from misreconstruction.

positions, which manifest as horizontal and vertical bars in Fig. 16. These strategies included:

- a coherent-clustering cut, restricted to events where the MWPCs of interest exhibit only one spatially confined cluster, and
- cuts on the maximum number of reconstructed hits in  $x$  and  $y$ .

The effectiveness of these approaches is illustrated in Fig. 63. While both methods, when combined, significantly reduce the number of misreconstructed events and improve the spatial hit distribution, they lead to a substantial loss in statistics of more than 40%

<sup>45</sup>The ripples in the y-reconstruction reflect the dimension of the readout pads in y-direction

(for coherent clustering & less than 5 hits in x & y).

Since the  $\pm 1\sigma$  position cuts were already chosen to be sufficiently tight for the analysis, no additional selection criteria were applied for the MWPC0 event selection.

## D Alternative methods for TWIN MUSIC hit selection and charge assignment

To quantify the impact of including or excluding border regions – i.e., cases where either  $\overline{Z}_{\text{up}} = 0$  or  $\overline{Z}_{\text{down}} = 0$  as illustrated in Fig. 20 – on the preliminary estimation of charge-changing cross sections, both scenarios were evaluated and the corresponding results are presented in Fig. 64. The observed differences are minor. Excluding the border regions leads to a slightly increased spread in the data points for the given beam energies.

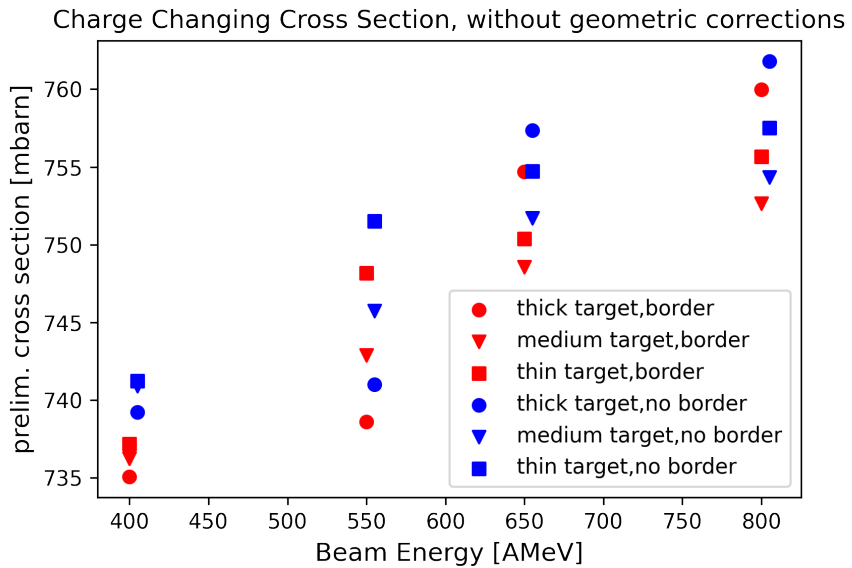


Figure 64: Preliminary estimation of charge-changing cross sections without geometry corrections. The red data points result from considering also events with only hits in the upstream or downstream anodes, the blue data points don't take these events in consideration.

Another method to assert the number survived carbon ions is to apply a diagonal cut on the 2D  $\Delta E$  histogram. To set the slope and offset of the diagonal cut line firstly the two dimensional Gaussian fit is applied, same as discussed in section 4.3.3. Then the intersection point between the  $3.5 \sigma$  ellipse and the identity line ( $\Delta E$  upstream

anodes =  $\Delta E$  downstream anodes) is found. Through this point, perpendicular to the identity line, the diagonal line is drawn. Everything above the diagonal line is considered as survived carbon ions. The borders are considered within the  $3.5\sigma$  cut, see figure 65. The effects of the two different methods used for the identification of the

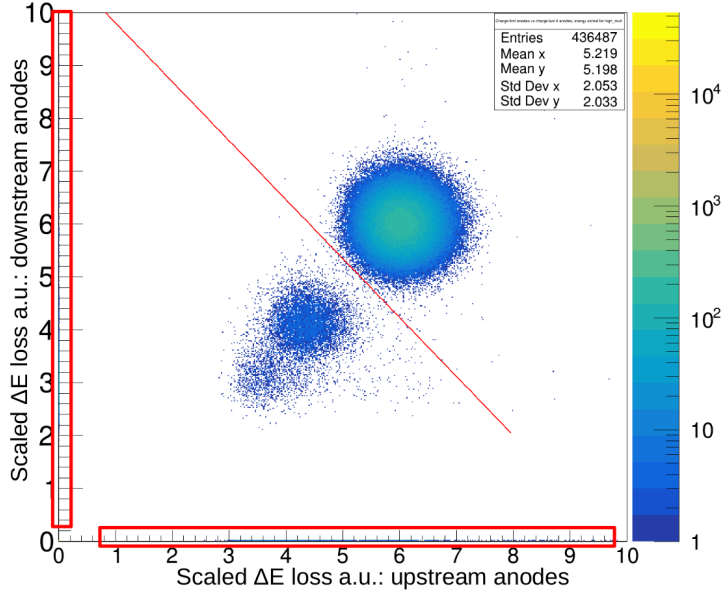


Figure 65: Diagonal cut on identified carbon isotopes along the Gaussian  $3.5\sigma$  cut with borders. All hits above the diagonal line are counted as carbon isotopes. Histogram from thick target run, 550 AMeV beam energy.

carbon isotopes for the charge changing cross section is summarized in figure 66. The differences in the measured cross sections are within the margin of error herefore both methods are comparable, as expected.

To check whether single anodes or groups of anodes are malfunctioning the charge changing cross section measurement was repeated using only certain anodes for the charge identification:

- a) anodes 2-8 versus anodes 9-15 (omitting first and last anode)
- b) anodes 1-4 versus anodes 5-8 (upstream anodes)
- c) anodes 5-8 versus anodes 9-12 (central anodes)
- d) anodes 9-12 versus anodes 13-16 (downstream anodes)

The results from the measurement are summarized in figure 67. The difference between the default Gaussian fit method (with  $3.5\sigma$  cut and considering the borders) considering

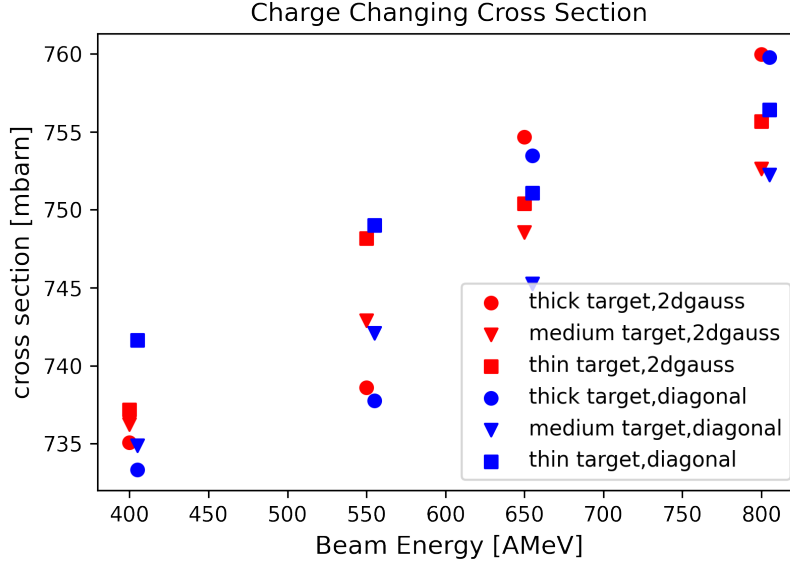


Figure 66: Comparison of the preliminary estimation of charge-changing cross sections measured via 2D Gaussian fit cut and diagonal cut. The differences are within the margin of error.

all 16 anodes and applying the same method but omitting the first and last anode is minimal over all four beam energies. When selecting only 8 out of 16 anodes instead the cross sections are systematically lower when going to high beam energies. The energy loss inside the TWIN MUSIC slightly decreases with higher beam energies (400 → 800 AMeV), according to the Bethe-Bloch formula [105]. The decrease of deposited energy for larger beam energies has as consequence a lower relative resolution in the two dimensional  $\Delta E$  loss histogram reflecting the poissonian distribution properties. In addition reducing the number of readout anodes by a factor two degrades the resolution by a factor  $\sqrt{2}$ <sup>46</sup>. This has as consequence that the ellipsis with  $3.5\sigma$  cut incorporates a non negligible amount of boron isotopes which are counted as survived carbon isotopes which in turn reduces the measured charge changing cross section.

While a time-based selection algorithm for multi-hit anodes was used in both the above measurements and in Section 4.3.3, an energy-based selection method was also tested for comparison. This algorithm selects for multi-hit anodes the hit with the highest energy as physical hit and discards all others, as they are considered as background/noise. Figure 68 compares the time based method versus the energy based

<sup>46</sup>It can be assumed a similar  $\Delta E$  distribution for all anodes. Hence the central limit theorem can be applied where  $\sigma = \frac{\sigma_{anode}}{\sqrt{n}}$  with  $n$  = number of anodes.

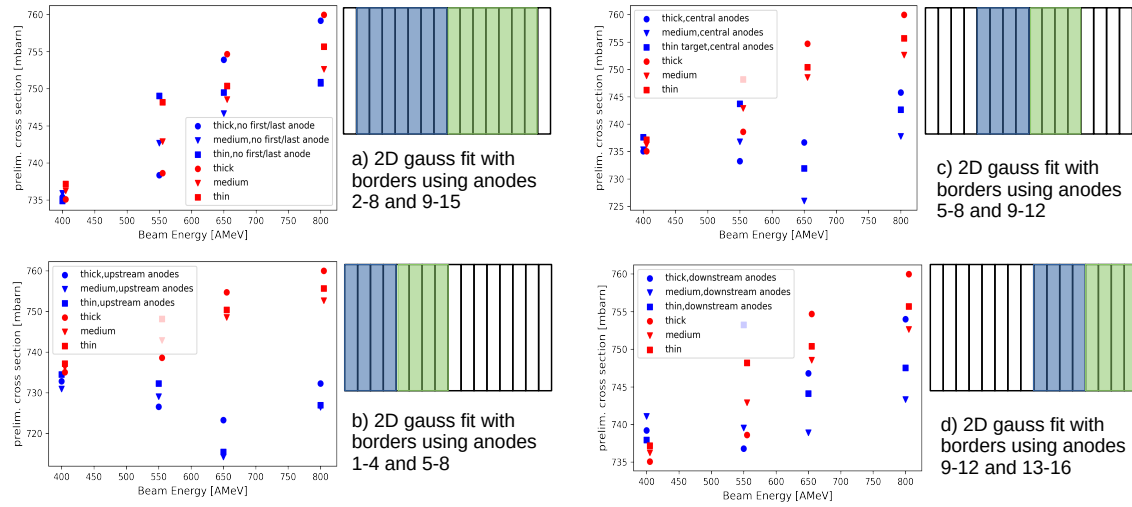


Figure 67: Measurement of charge changing cross sections using different anode sections to make the two dimensional Gaussian fit on the identified carbon isotopes. Red: using all 16 anodes. Blue: the various combinations.

method. In both cases a two dimensional Gaussian  $3.5\sigma$  cut is applied as in figure 20 and the borders are counted as well. The difference in the outcome is negligible. This can be explained since noise or background signal should be both uncorrelated to the event time and at a low energy level and are therefore filtered by both algorithms.

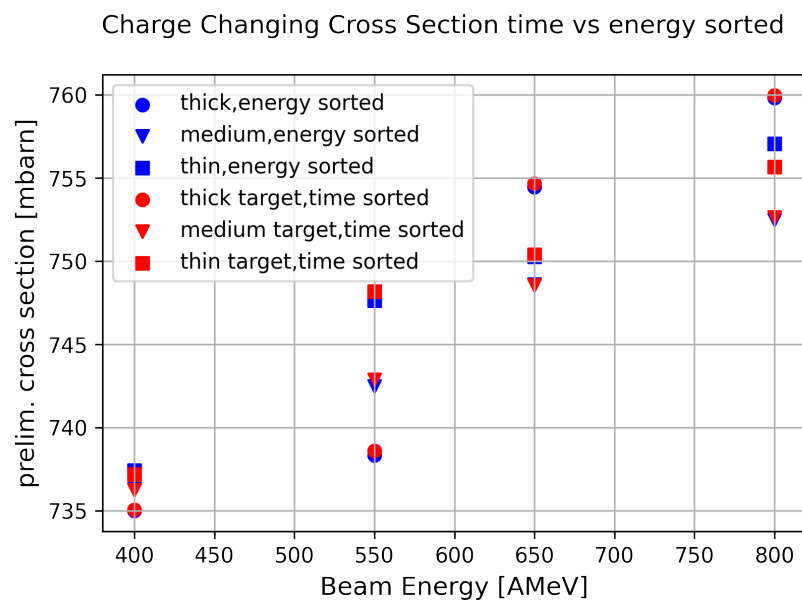


Figure 68: Comparison of charge changing cross section measurements when using time sorting algorithm(red) and energy sorting algorithm(blue) for multi-hit anodes.

## E TWIN MUSIC Geometric Acceptance Correction via Efficiency Measurement

Instead of correcting the limited geometric acceptance of TWIN MUSIC via graphical fitting (see section 4.4) it is also feasible correcting via TWIN MUSIC efficiency measurement. The correction factor is given by:

$$\epsilon_{geo\_corr} = \frac{N_{MWPC1,MWPC2}}{N_{MWPC1,MWPC2,TWIN}} \quad (46)$$

where  $N_{MWPC1,MWPC2}$  corresponds to the number of events with a hit in MWPC1 and MWPC2 whereas  $N_{MWPC1,MWPC2,TWIN}$  imposes the further condition having a hit in TWIN MUSIC too.

The corresponding correction factor  $\epsilon_{geo\_corr}$  is consequently applied on all target and empty runs. The resulting corrected charge changing cross section is shown in figure 69. The same correction factor can be applied to the total interaction cross section as

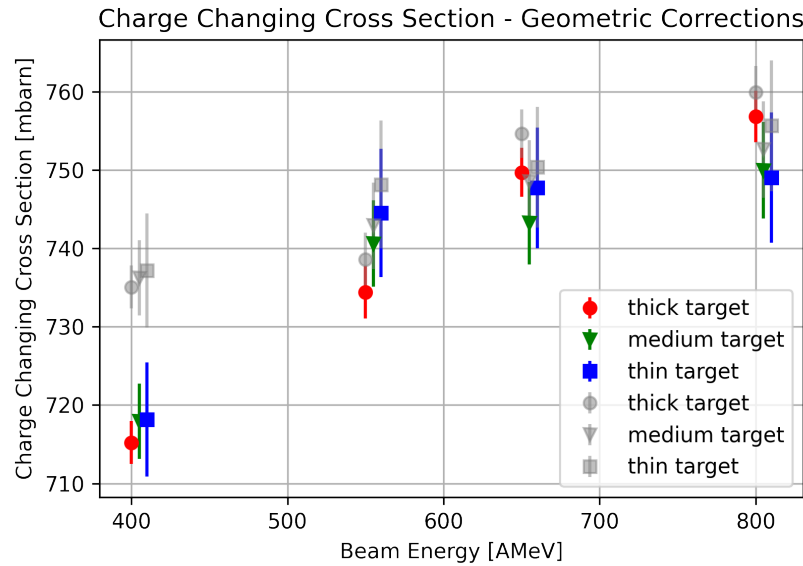


Figure 69: Charge changing cross section correction due to limited geometric acceptance of TWIN MUSIC via efficiency correction with MWPC1 and MWPC2. In gray: charge changing cross section measurements before applying corrections, as in figure 67

in figure 70.

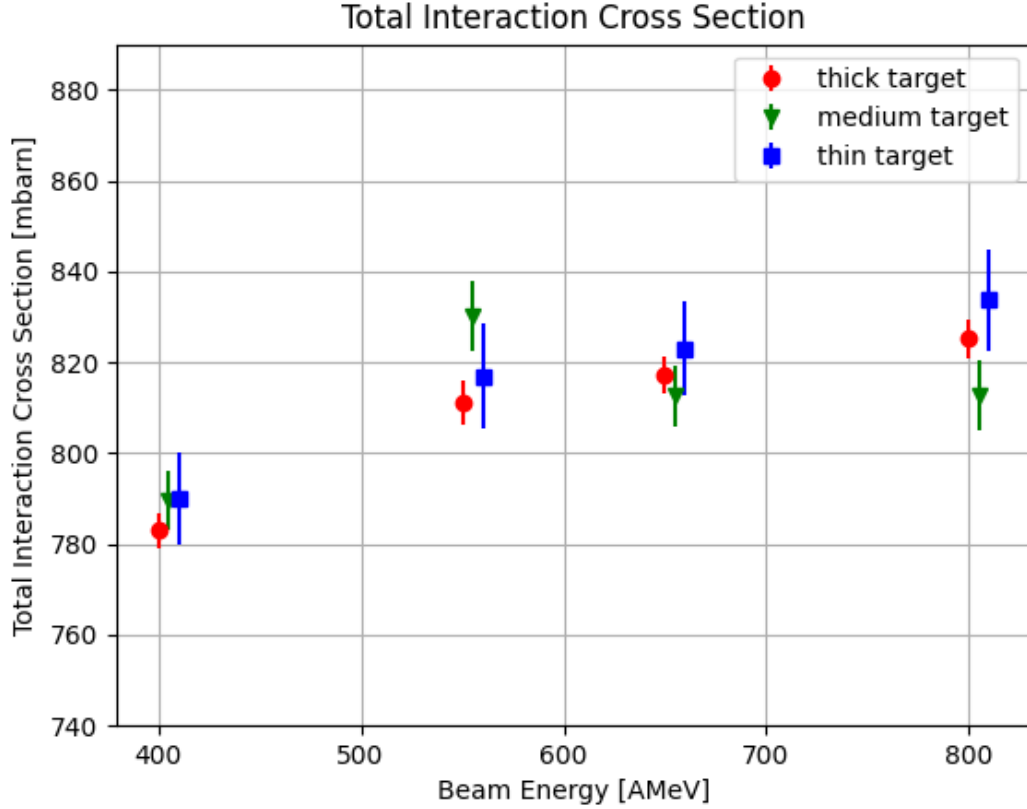


Figure 70: Total interaction cross section of  $^{12}\text{C} + ^{12}\text{C}$  using the TWIN MUSIC efficiency correction factor, see equation 46, to compensate for the limited geometric acceptance in TWIN MUSIC.

## F Overview of isotope correction methods - selection cuts on the MWPC1/2/3

## G Flight-Path Reconstruction

The first step in the radius and flightpath reconstruction is expressing the entrance point on the GLAD field  $(z_1, x_1)$  and the exit point  $(z_2, x_2)$  with the center of the circle path  $(z_0, x_0)$  as reference, see figure 71:

$$\begin{aligned}
 z_1 &= z_0 - r \cos(90^\circ - \theta_i) = z_0 - r \sin(\theta_i) \\
 x_1 &= x_0 + r \sin(90^\circ - \theta_i) = x_0 + r \cos(\theta_i) \\
 z_2 &= z_0 + r \cos(90^\circ - \theta_o) = z_0 + r \sin(\theta_o) \\
 x_2 &= x_0 + r \sin(90^\circ - \theta_o) = x_0 + r \cos(\theta_o)
 \end{aligned}$$

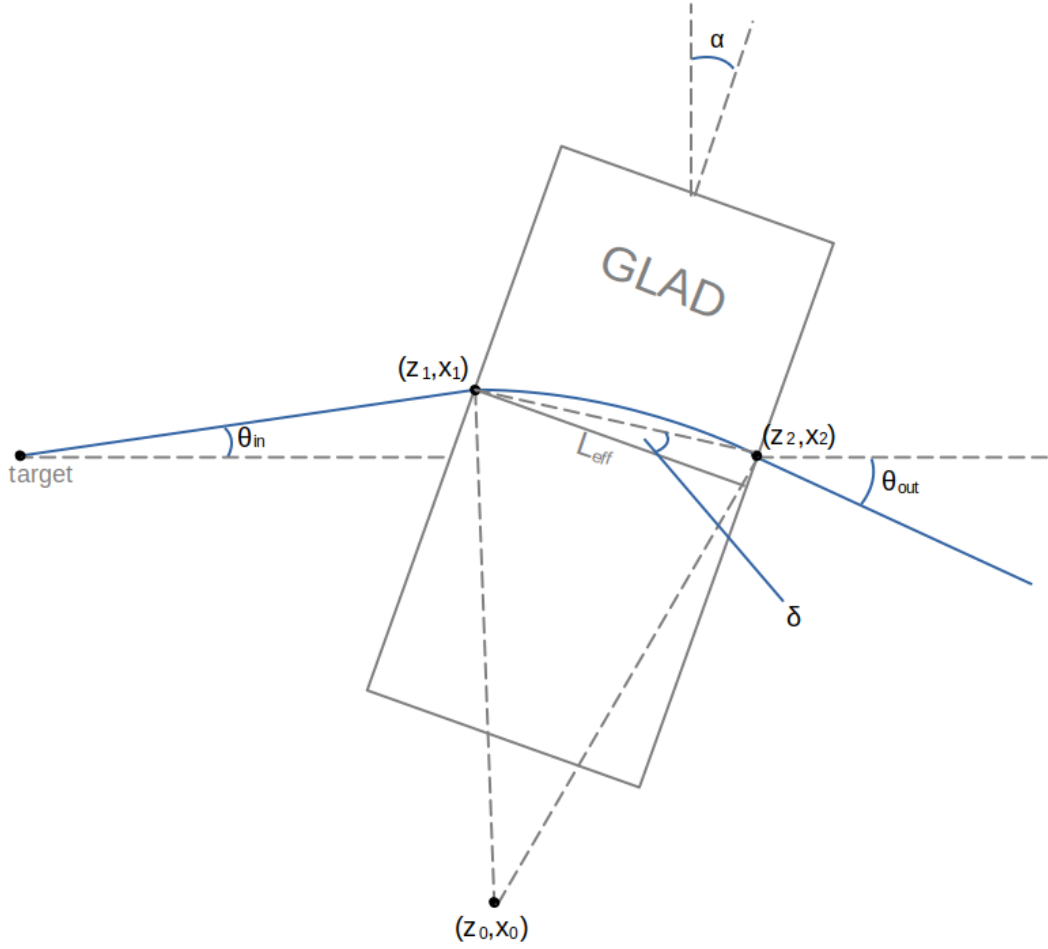


Figure 71: Flightpath reconstruction with reference positions  $(z_0, x_0)$ ,  $(z_1, x_1)$  and  $(z_2, x_2)$ . The GLAD magnet is tilted by  $\alpha = 14^\circ$ .

The slope  $m_1$  of the intersection line between  $(z_1, x_1)$  and  $(z_2, x_2)$  is given by:

$$m_1 = \frac{x_2 - x_1}{z_2 - z_1} = \frac{\cos(\theta_o) - \cos(\theta_i)}{\sin(\theta_o) + \sin(\theta_i)}$$

and with the distance between the two points given by:

$$\begin{aligned} \Delta_{i/o}^2 &= r^2 \left[ (\cos\theta_o - \cos\theta_i)^2 + (\sin\theta_o + \sin\theta_i)^2 \right] \\ &= 4r^2 \sin^2\left(\frac{\theta_i}{2} + \frac{\theta_o}{2}\right) \\ \Rightarrow \Delta_{i/o} &= 2r \sin\left(\frac{\theta_i}{2} + \frac{\theta_o}{2}\right) \end{aligned}$$

To describe the distance between  $(z_1, x_1)$  and  $(z_2, x_2)$  with the given effective GLAD length  $L_{eff}$  ( $= 2.06\text{ m}$ ) the tilting angle  $\alpha$  (see figure 71) of GLAD in relation to the incoming beam line direction has to be considered. Consequential the angle  $\delta$  between

the trajectory connecting  $(z_1, x_1)$  and  $(z_2, x_2)$  and the line parallel to the GLAD magnet width  $L_{eff}$  can be determined as:

$$\tan(\delta) = \left| \frac{m_1 - m_2}{1 + m_1 \cdot m_2} \right|$$

with  $m_2 = -\tan(\alpha)$ :

$$\delta = \text{atan} \left( \frac{\frac{\cos\theta_o - \cos\theta_i}{\sin\theta_o + \sin\theta_i} + \tan\alpha}{1 - \frac{\cos\theta_o - \cos\theta_i}{\sin\theta_o + \sin\theta_i} \cdot \tan\alpha} \right)$$

The final relation between  $L_{eff}$  and the bending radius  $r$  of the fragment within GLAD can be written as:

$$\begin{aligned} L_{eff} &= 2r \sin\left(\frac{\theta_i}{2} + \frac{\theta_o}{2}\right) \cdot \cos\delta \\ &= 2r \sin\left(\frac{\theta_i}{2} + \frac{\theta_o}{2}\right) \cdot \frac{1}{\sqrt{\delta^2 + 1}} \end{aligned} \tag{47}$$



## References

- [1] K. Wimmer, T. Kröll, R. Krücken, V. Bildstein, R. Gernhäuser, B. Bastin, N. Bree, J. Diriken, P. Van Duppen, M. Huyse, *et al.*, “Discovery of the shape coexisting  $0^+$  state in Mg 32 by a two neutron transfer reaction,” *Physical review letters*, vol. 105, no. 25, p. 252501, 2010.
- [2] R. Kanungo, C. Nociforo, A. Prochazka, T. Aumann, D. Boutin, D. Cortina-Gil, B. Davids, M. Diakaki, F. Farinon, H. Geissel, *et al.*, “One-Neutron Removal Measurement Reveals O 24 as a New Doubly Magic Nucleus,” *Physical review letters*, vol. 102, no. 15, p. 152501, 2009.
- [3] R. Krücken, for the NuSTAR collaboration, *et al.*, “The NuSTAR facility at FAIR,” *Journal of Physics G: Nuclear and Particle Physics*, vol. 31, no. 10, p. S1807, 2005.
- [4] F.-K. Thielemann, M. Eichler, I. Panov, and B. Wehmeyer, “Neutron star mergers and nucleosynthesis of heavy elements,” *Annual Review of Nuclear and Particle Science*, vol. 67, no. 1, pp. 253–274, 2017.
- [5] C. J. Horowitz, A. Arcones, B. Cote, I. Dillmann, W. Nazarewicz, I. U. Roederer, H. Schatz, A. Aprahamian, D. Atanasov, A. Bauswein, *et al.*, “r-process nucleosynthesis: Connecting rare-isotope beam facilities with the cosmos,” *Journal of Physics G: Nuclear and Particle Physics*, vol. 46, no. 8, p. 083001, 2019.
- [6] M. Heil, A. Kelić-Heil, L. Bott, T. Almusidi, H. Alvarez-Pol, L. Atar, L. Atkins, T. Aumann, J. Benlliure, K. Boretzky, *et al.*, “A new Time-of-flight detector for the R 3 B setup,” *The European Physical Journal A*, vol. 58, no. 12, p. 248, 2022.
- [7] O. Chamberlain and E. Segrè, “Proton-proton collisions within lithium nuclei,” *Physical Review*, vol. 87, no. 1, p. 81, 1952.
- [8] J. Cladis, W. Hess, and B. Moyer, “Nucleon momentum distributions in deuterium and carbon inferred from proton scattering,” *Physical Review*, vol. 87, no. 3, p. 425, 1952.
- [9] T. Maris, P. Hillman, and H. Tyrén, “Quasi-elastic scattering and nuclear structure,” *Nuclear Physics*, vol. 7, pp. 1–9, 1958.
- [10] B. Povh, K. Rith, C. Scholz, F. Zetsche, and W. Rodejohann, *Teilchen und Kerne: eine Einführung in die physikalischen Konzepte*. Springer-Verlag, 2013.

- [11] M. Patsyuk, J. Kahlbow, G. Laskaris, M. Duer, V. Lenivenko, E. Segarra, T. Atovullaev, G. Johansson, T. Aumann, A. Corsi, *et al.*, “Unperturbed inverse kinematics nucleon knockout measurements with a carbon beam,” *Nature physics*, vol. 17, no. 6, pp. 693–699, 2021.
- [12] P. Hansen and J. Tostevin, “Direct reactions with exotic nuclei,” *Annual Review of Nuclear and Particle Science*, vol. 53, no. 1, pp. 219–261, 2003.
- [13] W. Dickhoff and C. Barbieri, “Self-consistent Green’s function method for nuclei and nuclear matter,” *Progress in Particle and Nuclear Physics*, vol. 52, no. 2, pp. 377–496, 2004.
- [14] E. J. Moniz, I. Sick, R. Whitney, J. Ficenec, R. D. Kephart, and W. Trower, “Nuclear fermi momenta from quasielastic electron scattering,” *Physical Review Letters*, vol. 26, no. 8, p. 445, 1971.
- [15] A. S. Goldhaber, “Statistical models of fragmentation processes,” *Physics Letters B*, vol. 53, no. 4, pp. 306–308, 1974.
- [16] H. Feshbach and K. Huang, “Fragmentation of relativistic heavy ions,” *Physics Letters B*, vol. 47, no. 4, pp. 300–302, 1973.
- [17] L. Chulkov, F. Aksouh, A. Bleile, O. Bochkarev, D. Cortina-Gil, A. Dobrovolsky, P. Egelhof, H. Geissel, M. Hellström, N. Isaev, *et al.*, “Quasi-free scattering with  $^{6,8}\text{He}$  beams,” *Nuclear Physics A*, vol. 759, no. 1-2, pp. 43–63, 2005.
- [18] V. Panin, T. Aumann, and C. Bertulani, “Quasi-free scattering in inverse kinematics as a tool to unveil the structure of nuclei: A tribute to Mahir S. Hussein,” *The European Physical Journal A*, vol. 57, pp. 1–13, 2021.
- [19] L. Atar, S. Paschalis, C. Barbieri, C. A. Bertulani, P. Díaz Fernández, M. Holl, M. A. Najafi, V. Panin, H. Alvarez-Pol, T. Aumann, *et al.*, “Quasifree ( $p, 2p$ ) reactions on oxygen isotopes: observation of isospin independence of the reduced single-particle strength,” *Physical review letters*, vol. 120, no. 5, p. 052501, 2018.
- [20] M. Hjorth-Jensen, “The carbon challenge,” *Physics*, vol. 4, p. 38, 2011.
- [21] K. Sumiyoshi and G. Roepke, “Appearance of light clusters in post-bounce evolution of core-collapse supernovae,” *Physical Review C Nuclear Physics*, vol. 77, no. 5, p. 055804, 2008.
- [22] J. Mabiala, A. Cowley, S. Förttsch, E. Buthelezi, R. Neveling, F. Smit, G. Steyn, and J. Van Zyl, “Analyzing power and cross section distributions of the  $\text{C}^{12}(p,$

- p  $\alpha$ ) Be 8 cluster knockout reaction at an incident energy of 100 MeV," *Physical Review C Nuclear Physics*, vol. 79, no. 5, p. 054612, 2009.
- [23] L. Johannsen, A. Jensen, and P. Hansen, "The  $^{11}\text{Li}$  nucleus as a three-body system," *Physics Letters B*, vol. 244, no. 3-4, pp. 357–362, 1990.
- [24] H. Simon, D. Aleksandrov, T. Aumann, L. Axelsson, T. Baumann, M. Borge, L. Chulkov, R. Collatz, J. Cub, W. Dostal, *et al.*, "Direct experimental evidence for strong admixture of different parity states in  $^{11}\text{Li}$ ," *Physical review letters*, vol. 83, no. 3, p. 496, 1999.
- [25] C. Bertulani and M. S. Hussein, "Geometry of Borromean halo nuclei," *Physical Review C Nuclear Physics*, vol. 76, no. 5, p. 051602, 2007.
- [26] W. Xing, X.-G. Wang, and A. W. Thomas, "Electromagnetic form factors for nucleons in short-range correlations," *Physics Letters B*, vol. 846, p. 138195, 2023.
- [27] "Probing high-momentum protons and neutrons in neutron-rich nuclei," *Nature*, vol. 560, no. 7720, pp. 617–621, 2018.
- [28] S. Paschalis, M. Petri, A. Macchiavelli, O. Hen, and E. Piasetzky, "Nucleon-nucleon correlations and the single-particle strength in atomic nuclei," *Physics Letters B*, vol. 800, p. 135110, 2020.
- [29] J. Gerl, "NUCLEAR SPECTROSCOPY STUDIES AT GSI—FROM RISING TO HISPEC/DESPEC.," *Acta Physica Polonica B*, vol. 40, no. 3, 2009.
- [30] D. Ackermann, "Superheavy elements at GSI-present and future," *Nuclear Physics A*, vol. 787, no. 1-4, pp. 353–362, 2007.
- [31] T. Galatyuk, H. Collaboration, *et al.*, "HADES overview," *Nuclear Physics A*, vol. 931, pp. 41–51, 2014.
- [32] H.-J. Kluge, T. Beier, K. Blaum, L. Dahl, S. Eliseev, F. Herfurth, B. Hofmann, O. Kester, S. Koszudowski, C. Kozhuharov, *et al.*, "HITRAP: a facility at GSI for highly charged ions," *Advances in Quantum Chemistry*, vol. 53, pp. 83–98, 2008.
- [33] Z. Major, U. Eisenbarth, B. Zielbauer, C. Brabertz, J. Ohland, Y. Zobus, S. Roeder, D. Reemts, S. Kunzer, S. Götte, *et al.*, "High-energy laser facility PHELIX at GSI: latest advances and extended capabilities," *High Power Laser Science and Engineering*, vol. 12, p. e39, 2024.

- [34] C. E. Düllmann, M. Block, F. P. Heßberger, J. Khuyagbaatar, B. Kindler, J. V. Kratz, B. Lommel, G. Münzenberg, V. Pershina, D. Renisch, *et al.*, “Five decades of GSI superheavy element discoveries and chemical investigation,” *Radiochimica Acta*, vol. 110, no. 6-9, pp. 417–439, 2022.
- [35] “Starting point of the GSI accelerator facility: Ion sources.” Accessed: 2025-04-03.
- [36] “Ring accelerator SIS18 - the record holder.” Accessed: 2025-04-03.
- [37] C. Nociforo, “Time-of-flight measurements at the Super-FRS,” *Journal of Instrumentation*, vol. 9, no. 01, p. C01022, 2014.
- [38] L. Ponnath, T. Aumann, C. Bertulani, R. Gernhäuser, M. Heil, T. Almusidi, H. Alvarez-Pol, L. Atar, L. Atkins, Y. Ayyad, *et al.*, “Measurement of nuclear interaction cross sections towards neutron-skin thickness determination,” *Physics Letters B*, vol. 855, p. 138780, 2024.
- [39] G. Charpak, R. Bouclier, T. Bressani, J. Favier, and Č. Zupančič, “The use of multiwire proportional counters to select and localize charged particles,” *Nuclear Instruments and Methods*, vol. 62, no. 3, pp. 262–268, 1968.
- [40] J.-F. Martin, J. Taïeb, G. Boutoux, A. Chatillon, T. Gorbinet, E. Pellereau, L. Audouin, A. Heinz, H. Alvarez-Pol, Y. Ayyad, *et al.*, “Fission-fragment yields and prompt-neutron multiplicity for Coulomb-induced fission of U 234, 235 and Np 237, 238,” *Physical Review C*, vol. 104, no. 4, p. 044602, 2021.
- [41] GSI Helmholtzzentrum für Schwerionenforschung GmbH, “Large-acceptance dipole magnet glad.” [https://www.gsi.de/fileadmin/Kernreaktionen/GLAD\\_in\\_CaveC.jpg](https://www.gsi.de/fileadmin/Kernreaktionen/GLAD_in_CaveC.jpg), 2013. [Online; accessed September 09, 2024].
- [42] “Technical report for the design, construction and commissioning of the califa barrel.” [https://igfae.usc.es/~r3b/documentos/TDR/CALIFA\\_BARREL\\_TDR.pdf](https://igfae.usc.es/~r3b/documentos/TDR/CALIFA_BARREL_TDR.pdf). Accessed: 2024-09-24.
- [43] “Technical Report for the Design, Construction and Commissioning of the CALIFA Endcap.” [https://edms.cern.ch/ui/file/1833748/2/TDR\\_R3B\\_CALIFA\\_ENDCAP\\_public.pdf](https://edms.cern.ch/ui/file/1833748/2/TDR_R3B_CALIFA_ENDCAP_public.pdf). Accessed: 2024-09-24.
- [44] M. Bendel, *Entwicklung einer neuartigen Nachweismethode hochenergetischer Teilchen im CALIFA-Kalorimeter*. Dr., Technische Universität München, München, 2014. Technische Universität München, Diss., 2014.

- [45] J. Graña-González, J. Rodríguez-Sánchez, J. Benlliure, G. García-Jiménez, H. Alvarez-Pol, D. Cortina-Gil, L. Atar, L. Audouin, G. Authelet, A. Besteiro, *et al.*, “Fission studies in inverse kinematics with the R3B setup,” in *EPJ Web of Conferences*, vol. 290, p. 02015, EDP Sciences, 2023.
- [46] M. Bendel, *Entwicklung einer neuartigen Nachweismethode hochenergetischer Teilchen im CALIFA-Kalorimeter*. PhD thesis, Technische Universität München, 2014.
- [47] R. Murray and A. Meyer, “Scintillation response of activated inorganic crystals to various charged particles,” *Physical Review*, vol. 122, no. 3, p. 815, 1961.
- [48] S. Zazubovich, “Physics of halide scintillators,” *Radiation Measurements*, vol. 33, no. 5, pp. 699–704, 2001.
- [49] I. Holl, E. Lorenz, and G. Mageras, “A measurement of the light yield of common inorganic scintillators,” *IEEE Transactions on Nuclear Science*, vol. 35, no. 1, pp. 105–109, 1988.
- [50] A. Syntfeld-Kazuch, L. Swiderski, W. Czarnacki, M. Gierlik, W. Klamra, M. Moszynski, and P. Schotanus, “Non-proportionality and energy resolution of CsI (Tl),” *IEEE Transactions on Nuclear Science*, vol. 54, no. 5, pp. 1836–1841, 2007.
- [51] M. Winkel, *Implementierung und Erprobung einer digitalen Pulsformanalyse zur Auslese von Kalorimetern*. PhD thesis, Diplomarbeit, 2011.
- [52] M. O. Winkel, *Komplexe Pulsformalgorithmen und Teilchenidentifikation zur Echtzeit-Implementierung in CALIFA*. PhD thesis, Technische Universität München, 2016.
- [53] A.-L. Hartig, “Evolution of CALIFA: From single detector modules to benchmark reactions,”
- [54] Hamamatsu Photonics, “S8664-1010: Silicon Avalanche Photodiode.” <https://www.hamamatsu.com/jp/en/product/optical-sensors/apd/si-apd/S8664-1010.html>, 2025. Accessed: 2025-04-30.
- [55] “Mesytec.” <https://www.mesytec.com/>. [Online; accessed September 29, 2024].
- [56] K. Philipp, *Gamma detection with CALIFA*. PhD thesis, Technische Universität München, 2024.

- [57] B. Jacob, S. W. Ng, and D. T. Wang, *Memory Systems: Cache, DRAM, Disk*. Morgan Kaufmann, 2008.
- [58] “Multi Branch System (MBS).” [https://www.gsi.de/en/work/research/experiment\\_electronics/data\\_processing/data\\_acquisition/mbs](https://www.gsi.de/en/work/research/experiment_electronics/data_processing/data_acquisition/mbs). Accessed: 2025-05-02.
- [59] A. Bail, J. Taieb, A. Chatillon, G. Belier, B. Laurent, and E. Pellereau, “Time of flight measurement on the SOFIA experiment,” in *2011 2nd International Conference on Advancements in Nuclear Instrumentation, Measurement Methods and their Applications*, pp. 1–4, IEEE, 2011.
- [60] K. Boretzky, I. Gašparić, M. Heil, J. Mayer, A. Heinz, C. Caesar, D. Kresan, H. Simon, H. T. Törnqvist, D. Körper, *et al.*, “NeuLAND: The high-resolution neutron time-of-flight spectrometer for R3B at FAIR,” *Nuclear Instruments and Methods in Physics Research Section A: Accelerators, Spectrometers, Detectors and Associated Equipment*, vol. 1014, p. 165701, 2021.
- [61] K. Boretzky, G. Alkazov, L. Atar, T. Aumann, and C. Beinrucker, “NeuLAND— from double-planes to the demonstrator,” *GSI Sci. Rep.*, vol. 200, p. 2015, 2014.
- [62] W. Bethge, “Wiedemann, Kernphysik,” 2007.
- [63] L. Ponnath, *Precise Measurement of Nuclear Interaction Cross Sections with R3B*. PhD thesis, Technische Universität München, 2023.
- [64] “MDPP-16 Detector Readout Systems, Mesytec.” <https://www.mesytec.com/products/nuclear-physics/MDPP-16.html>. [Online; accessed October 18, 2024].
- [65] O. Bertini, *Study of 3 Lambda H and 4 Lambda H in the reaction of 6 Li + 12 C at 2 A GeV*. PhD thesis, Dissertation, Mainz, Johannes Gutenberg-Universität Mainz, 2013.
- [66] E. Bayer and M. Traxler, “Development of a high-resolution (< 10 ps RMS) 32-channel TDC in a field-programmable-gate-arrays,” *Instruments-Methods-45, GSI Scientific Report 2009*, p. 325, 2009.
- [67] J. Serrano, M. Lipinski, T. Wlostowski, E. Gousiou, E. van der Bij, M. Cattin, and G. Daniluk, “The white rabbit project,” 2013.

- [68] International Atomic Energy Agency, “Iaea live chart of nuclides.” <https://www-nds.iaea.org/relnsd/vcharthtml/VChartHTML.html>, 2024. Accessed: 2025-05-16.
- [69] G. Van Der Steenhoven, H. Blok, E. Jans, L. Lapikás, E. Quint, and P. D. W. Huberts, “Weak transitions in the quasi-elastic reaction  $^{12}\text{C}$  ( $e, \tilde{\nu}p$ )  $^{11}\text{B}$ ,” *Nuclear Physics A*, vol. 484, no. 3-4, pp. 445–475, 1988.
- [70] K. S. Krane, *Introductory Nuclear Physics*. John Wiley & Sons, 1987.
- [71] O. Hahn and F. Strassmann, “Nachweis der Entstehung aktiver Bariumisotope aus Uran und Thorium durch Neutronenbestrahlung; Nachweis weiterer aktiver Bruchstücke bei der Uranspaltung,” *Naturwissenschaften*, vol. 27, pp. 89–95, 1939.
- [72] L. Meitner and O. R. Frisch, “Disintegration of uranium by neutrons: a new type of nuclear reaction,” *Nature*, vol. 143, no. 3615, pp. 239–240, 1939.
- [73] N. Bohr and J. Wheeler, “Phys. Rev.,” *Phys. Rev.*, vol. 56, no. 426, 1939.
- [74] T. Mayer-Kuckuk, *Kernphysik: Eine Einführung*. Springer-Verlag, 2013.
- [75] F. Bassani, G. L. Liedl, and P. Wyder, “Encyclopedia of condensed matter physics,” 2005.
- [76] H. Paşa, A. Andreev, G. Adamian, and N. Antonenko, “Possible origin of transition from symmetric to asymmetric fission,” *Physics Letters B*, vol. 760, pp. 800–806, 2016.
- [77] A. Andreev, G. Adamian, and N. Antonenko, “Mass distributions for induced fission of different Hg isotopes,” *Physical Review C-Nuclear Physics*, vol. 86, no. 4, p. 044315, 2012.
- [78] P. Möller, J. Randrup, and A. J. Sierk, “Calculated fission yields of neutron-deficient mercury isotopes,” *Physical Review C-Nuclear Physics*, vol. 85, no. 2, p. 024306, 2012.
- [79] V. A. Popescu, “Review of mass and charge distributions in low energy fission for  $^{235,238}\text{U}$  and  $^{239}\text{Pu}$ ,” 2021.
- [80] G. García-Jiménez, H. Alvarez-Pol, A. Graña-González, J. Rodríguez-Sánchez, J. Benlliure, D. Cortina-Gil, L. Atar, L. Audouin, G. Authelet, A. Besteiro, *et al.*, “Study of ( $p, 2p$ ) fission reactions in inverse kinematics using the R3B set-up,” in *EPJ Web of Conferences*, vol. 290, p. 02009, EDP Sciences, 2023.

- [81] P. Morfouace, J. Taieb, A. Chatillon, L. Audouin, G. Blanchon, R. Bernard, N. Dubray, N. Pillet, D. Regnier, H. Alvarez-Pol, *et al.*, “An asymmetric fission island driven by shell effects in light fragments,” *Nature*, pp. 1–6, 2025.
- [82] E. Sartori, “Nuclear data for radioactive waste management,” *Annals of Nuclear Energy*, vol. 62, pp. 579–589, 2013.
- [83] H. Schopper, “Excited Nuclear States: Nuclei with Z= 48-60,” *Excited Nuclear States: Nuclei with Z= 48-60*, 2013.
- [84] H. Kolanoski and N. Wermes, *Teilchendetektoren*, ch. 13.5.2. Springer, 2016.
- [85] S. Seltzer, “XCOM-Photon Cross Sections Database, NIST Standard Reference Database 8.” <http://www.nist.gov/pml/data/xcom/index.cfm>, 2010. Accessed: 2025-04-10.
- [86] O. Klein and Y. Nishina, “Über die Streuung von Strahlung durch freie Elektronen nach der neuen relativistischen Quantendynamik von Dirac,” *Zeitschrift für Physik*, vol. 52, no. 11, pp. 853–868, 1929.
- [87] G. F. Knoll, *Radiation Detection and Measurement*. John Wiley & Sons, 4th ed., 2010. See Chapter 7 (Interaction of Gamma Rays with Matter) and Chapter 12 (Gamma-Ray Spectroscopy) for discussion of single and double escape peaks.
- [88] M. Lipiński, T. Włostowski, J. Serrano, and P. Alvarez, “White rabbit: A PTP application for robust sub-nanosecond synchronization,” in *2011 IEEE International Symposium on Precision Clock Synchronization for Measurement, Control and Communication*, pp. 25–30, IEEE, 2011.
- [89] D. Bertini, “R3BRoot, simulation and analysis framework for the R3B experiment at FAIR,” in *Journal of Physics: Conference Series*, vol. 331, p. 032036, IOP Publishing, 2011.
- [90] S. Agostinelli, J. Allison, K. a. Amako, J. Apostolakis, H. Araujo, P. Arce, M. Asai, D. Axen, S. Banerjee, G. Barrand, *et al.*, “GEANT4â€“ toolkit,” *Nuclear instruments and methods in physics research section A: Accelerators, Spectrometers, Detectors and Associated Equipment*, vol. 506, no. 3, pp. 250–303, 2003.
- [91] F. Nielsen, *Hierarchical Clustering*, pp. 195–211. Cham: Springer International Publishing, 2016.

- [92] P. Virtanen, R. Gommers, T. E. Oliphant, M. Haberland, T. Reddy, D. Cournapeau, E. Burovski, P. Peterson, W. Weckesser, J. Bright, *et al.*, “SciPy 1.0: fundamental algorithms for scientific computing in Python,” *Nature methods*, vol. 17, no. 3, pp. 261–272, 2020.
- [93] F. Nielsen and F. Nielsen, “Hierarchical clustering,” *Introduction to HPC with MPI for Data Science*, pp. 195–211, 2016.
- [94] S. Imambi, K. B. Prakash, and G. Kanagachidambaresan, “Pytorch,” *Programming with TensorFlow: solution for edge computing applications*, pp. 87–104, 2021.
- [95] S. Mannor, D. Peleg, and R. Rubinstein, “The cross entropy method for classification,” in *Proceedings of the 22nd international conference on Machine learning*, pp. 561–568, 2005.
- [96] P.-T. De Boer, D. P. Kroese, S. Mannor, and R. Y. Rubinstein, “A tutorial on the cross-entropy method,” *Annals of operations research*, vol. 134, pp. 19–67, 2005.
- [97] D. Newton, R. Pasupathy, and F. Yousefian, “Recent trends in stochastic gradient descent for machine learning and Big Data,” in *2018 Winter Simulation Conference (WSC)*, pp. 366–380, IEEE, 2018.
- [98] P. W. Battaglia, J. B. Hamrick, V. Bapst, A. Sanchez-Gonzalez, V. Zambaldi, M. Malinowski, A. Tacchetti, D. Raposo, A. Santoro, R. Faulkner, *et al.*, “Relational inductive biases, deep learning, and graph networks,” *arXiv preprint arXiv:1806.01261*, 2018.
- [99] A. Vaswani, N. Shazeer, N. Parmar, J. Uszkoreit, L. Jones, A. N. Gomez, Ł. Kaiser, and I. Polosukhin, “Attention is all you need,” *Advances in neural information processing systems*, vol. 30, 2017.
- [100] X. Amatriain, A. Sankar, J. Bing, P. K. Bodugutla, T. J. Hazen, and M. Kazi, “Transformer models: an introduction and catalog,” *arXiv preprint arXiv:2302.07730*, 2023.
- [101] G. DeZoort, S. Thais, J. Duarte, V. Razavimaleki, M. Atkinson, I. Ojalvo, M. Neubauer, and P. Elmer, “Charged particle tracking via edge-classifying interaction networks,” *Computing and Software for Big Science*, vol. 5, pp. 1–13, 2021.

- [102] X. Ju, D. Murnane, P. Calafiura, N. Choma, S. Conlon, S. Farrell, Y. Xu, M. Spiropulu, J.-R. Vlimant, A. Aurisano, *et al.*, “Performance of a geometric deep learning pipeline for HL-LHC particle tracking,” *The European Physical Journal C*, vol. 81, pp. 1–14, 2021.
- [103] S. Van Stroud, P. Duckett, M. Hart, N. Pond, S. Rettie, G. Facini, and T. Scanlon, “Transformers for Charged Particle Track Reconstruction in High Energy Physics,” *arXiv preprint arXiv:2411.07149*, 2024.
- [104] K. Lau and J. Pyrlik, “Optimization of centroid-finding algorithms for cathode strip chambers,” *Nuclear Instruments and Methods in Physics Research Section A: Accelerators, Spectrometers, Detectors and Associated Equipment*, vol. 366, no. 2-3, pp. 298–309, 1995.
- [105] H. Bethe, “Zur Theorie des Durchgangs schneller Korpuskularstrahlen durch Materie,” *Annalen der Physik*, vol. 397, no. 3, pp. 325–400, 1930.